

UNIVERSITY OF GENOA



DOCTORAL THESIS

**Large-Scale Transport in
Geophysical Flows.
Developments and Applications.**

Author:

Daniele LAGOMARSINO ONETO

Supervisor:

Prof. Andrea MAZZINO

*A thesis submitted in fulfillment of the requirements
for the degree of Doctor of Philosophy*

Doctoral School in Civil, Chemical and
Environmental Engineering
Curriculum in Fluid Dynamics and Environmental Engineering

May 7, 2018

Supervisor:

Prof. Andrea Mazzino - DICCA, University of Genoa

External Reviewers:

Prof. Angelo Vulpiani - Department of Physics, University of Roma "La Sapienza"

Dott. Filippo De Lillo - Department of Physics, University of Turin

Examination Committee:

Prof. Nicoletta Tambroni - DICCA, University of Genoa

Prof. Ilaria Gnecco - DICCA, University of Genoa

Prof. Simone Camarri - DICI, University of Pisa

Prof. Carlo Camporeale - DIATI, Polytechnic of Turin

Ph.D. program in Civil, Chemical and Environmental Engineering

Curriculum in Fluid Dynamics and Environmental Engineering

Cycle XXX

Contents

1	Introduction	1
2	Fundamental results	5
2.1	Transport processes	5
2.1.1	Diffusion	6
2.1.2	Advection	8
2.2	The Lagrangian approach	8
2.3	Turbulence	11
2.4	Homogeneization	13
2.5	Anomalous diffusion	14
3	Survival strategies in fungal kingdom	15
3.1	Fungal spore dissemination	15
3.2	Describing spore dispersal	18
3.3	Numerical study	19
3.3.1	The meteorological dataset	19
3.3.2	Numerical techniques.	20
3.3.3	Statistical observables	26
3.4	Results	27
3.4.1	Role of the ABL dynamics	35
3.5	Conclusions	47
4	Eddy diffusivities in sea surface dispersion	53
4.1	The strategy	53
4.2	Advective fields	55
4.2.1	Field analysis	56
4.2.2	Filtered fields	61
4.3	Modeling transport	61
4.3.1	Numerical solution techniques	63
4.3.2	Numerical simulations	65
4.3.3	Conclusions	69
A	Papers in preparation	73

Bibliography **75**

Acknowledgments **79**

List of Figures

3.1	Geographical domain of North American Regional Reanalysis (NARR): the dataset covers the entire area of the continent in the northern hemisphere, from Mexico to Canada across the United States. Grid points on which meteorological variables (like wind velocity) are known are plotted one every five, the actual horizontal resolution is about 32 km.	20
3.2	Geographical distribution of spores release location in North America: ten different starting locations have been chosen for spores release and are showed on the map as red circles.	27
3.3	Mean flight time signal for releases started at Green Mexico during January and April of year 2014.	29
3.4	Mean flight time signal for releases started at Green Mexico during July and October of year 2014.	30
3.5	Mean flight time signal for releases started at Veggies Wi during January and April of year 2014.	31
3.6	Mean flight time signal for releases started at Veggies Wi during July and October of year 2014.	32
3.7	Mean flight time signal for releases started at Wheat Alberta during January and April of year 2014	33
3.8	Mean flight time signal for releases started at Wheat Alberta during July and October of year 2014	34
3.9	Dots represent the mean flight time averaged on all releases performed in Green Mexico at the same hour but different days of the selected period; width of the shaded band is the related standard deviation. Figure a) shows the result of the averaging procedure for January, April, July and October separately; in figure b) all months are considered together.	36

-
- 3.10 Dots represent the mean flight time averaged on all releases performed in Wheat Mexico at the same hour but different days of the selected period; width of the shaded band is the related standard deviation. Figure a) shows the result of the averaging procedure for January, April, July and October separately; in figure b) all months are considered together. 37
- 3.11 Dots represent the mean flight time averaged on all releases performed in Baja Ca at the same hour but different days of the selected period; width of the shaded band is the related standard deviation. Figure a) shows the result of the averaging procedure for January, April, July and October separately; in figure b) all months are considered together. 38
- 3.12 Dots represent the mean flight time averaged on all releases performed in Crops Okla at the same hour but different days of the selected period; width of the shaded band is the related standard deviation. Figure a) shows the result of the averaging procedure for January, April, July and October separately; in figure b) all months are considered together. 39
- 3.13 Dots represent the mean flight time averaged on all releases performed in Tobacco NC at the same hour but different days of the selected period; width of the shaded band is the related standard deviation. Figure a) shows the result of the averaging procedure for January, April, July and October separately; in figure b) all months are considered together. 40
- 3.14 Dots represent the mean flight time averaged on all releases performed in Crops Ca at the same hour but different days of the selected period; width of the shaded band is the related standard deviation. Figure a) shows the result of the averaging procedure for January, April, July and October separately; in figure b) all months are considered together. 41
- 3.15 Dots represent the mean flight time averaged on all releases performed in Forest Colorado at the same hour but different days of the selected period; width of the shaded band is the related standard deviation. Figure a) shows the result of the averaging procedure for January, April, July and October separately; in figure b) all months are considered together. 42
- 3.16 Dots represent the mean flight time averaged on all releases performed in Veggies Wi at the same hour but different days of the selected period; the width of the shaded band is the related standard deviation. Figure a) shows the result of the averaging procedure for January, April, July and October separately; in figure b) all months are considered together. 43

3.17	Dots represent the mean flight time averaged on all releases performed in Wild Canada at the same hour but different days of the selected period; width of the shaded band is the related standard deviation. Figure a) shows the result of the averaging procedure for January, April, July and October separately; in figure b) all months are considered together.	44
3.18	Dots represent the mean flight time averaged on all releases performed in Wheat Alberta at the same hour but different days of the selected period; width of the shaded band is the related standard deviation. Figure a) shows the result of the averaging procedure for January, April, July and October separately; in figure b) all months are considered together.	45
3.19	Probability density function and cumulative distribution of flight times, averaged on all releases started at 2:00 PM (unstable case) of all days in July 2014. The blue line with squares is the averaged curve. The distance between green continuous lines and the blue line represents the standard deviation from the average.	46
3.20	Probability density function and cumulative distribution of flight times, averaged on all releases started at 2:00 AM (stable case) of all days in July 2014. The blue line with squares is the averaged curve. The distance between green continuous lines and the blue line represents the standard deviation from the average.	47
3.21	Histograms of particles height during the first hour after the release. a) unstable case; b) stable case.	48
4.1	Sketch of how the strategy works: the large-scale field is produced filtering out the smallest dynamical scales in the fully resolved field. In the energy spectrum the contribution of all the modes with wave numbers higher than a chosen cutoff is removed.	54
4.2	The geographic area in which the circulation is given.	55
4.3	Both preliminary analysis and transport simulations are performed in the subdomain inside the blue square. The side of this area is about 150 km.	56
4.4	<i>Upper left:</i> histogram of the spatial averaging at fixed times of the current speed inside the domain; <i>Upper right:</i> polar histogram of the direction of the current averaged in space at fixed times; <i>Lower:</i> time series of spatially averaged kinetic energy per unit mass.	57
4.5	Bathymetry inside the domain and slope of the shelf. <i>Up:</i> the continental shelf very sharp in the geographic area of the case. The white line is a top view of the cross section shown in right panel. <i>Down:</i> Cross section of the shelf that gives the idea of its slope.	58

4.6	Energy spectrum calculated averaging over angular coordinates in the k -space. In agreement with the Kolmogorov law, it shows a clear range of ks with energies that follow a $k^{-5/3}$ law up to scales of the order of $\sim 10 km$	59
4.7	Normalized autocorrelations permit to appreciate also qualitatively that correlation times decrease with the wave number. . . .	60
4.8	Fully resolved field: snapshot of the advective velocity in the FRF at a fixed time: the color represents the current speed and arrows the direction. Notice that many small-scale structures are present in the flow.	61
4.9	Filtered fields: snapshots of the advective velocity in two LSF generated with different cutoffs. <i>Up</i> : cutoff wavenumber $k = 5 \cdot 10^{-4} m^{-1}$; <i>Down</i> : cutoff wavenumber $k = 2 \cdot 10^{-4} m^{-1}$. Notice the progressive reduction of structures when the cutoff is reduced	62
4.10	Comparison between time series of U_{rms} (blue signal) and of a characteristic turbulent velocity scale computed as $\sqrt{2TKE}$ (red signal), for a cutoff $k_L = 2 \cdot 10^{-4} m^{-1}$. This figure gives the idea of the relative importance of removed scales in the transport.	65
4.11	Snapshot of the D_{11} field calculated for $k_L = 2 \cdot 10^{-4} m^{-1}$	66
4.12	Snapshot of the D_{22} field calculated for $k_L = 2 \cdot 10^{-4} m^{-1}$	66
4.13	Snapshot of the the extra-diagonal component of the Eddy Diffusivity tensor field $D_{12} = D_{21}$,calculated for $k_L = 2 \cdot 10^{-4} m^{-1}$	67
4.14	Dispersion is measured looking at the particle displacement variances. This plot shows the evolution in time of $Var_{XX} + Var_{YY}$ for a particular release of particles. The blue line represents the transport in the FRF, the green line in the filtered field without any description of the subgrid dynamics. Red and light blue lines are related with transport simulation in which an Eddy Diffusivity closure has been applied. In is clear that, in this case, Eddy diffusivity closures make worse the description of transport.	69
4.15	Dispersion is measured looking at the particle displacement variances. This plot shows the evolution in time of $Var_{XX} + Var_{YY}$ for a particular release of particles. The blue line represents the transport in the FRF, the green line in the filtered field without any description of the subgrid dynamics. Red and light blue lines are related with transport simulation in which an Eddy Diffusivity closure has been applied.	70
4.16	Dispersion is measured looking at the particle displacement variances. This plot shows the evolution in time of $Var_{XX} + Var_{YY}$ for a particular release of particles. The blue line represents the transport in the FRF, the green line in the filtered field without any description of the subgrid dynamics. Red and light blue lines are related with transport simulation in which an Eddy Diffusivity closure has been applied.	71

4.17 Clustering of particles on small-scale structures in the FRF (lower than the cutoff wave-length $\lambda \sim 30 km$).	71
4.18 Compressibility index as function of time, it is equal to 0 in incompressible flows (averaging on space) and it is equal to 1 in the pure potential case. The blue line represents the fully resolved field while the green represents the filtered one. It is evident for all times that, in the filtering process, a great contribution to compressibility is removed.	72

List of Tables

3.1	Physical spore parameters	19
3.2	Starting locations for simulations	28
3.3	Diurnal cycle strength and sharpness: for each starting location and each selected period, the maximum mean flight time averaged on releases performed at the same hour of the day and the index \mathcal{I} that measure the goodness of the cycle are shown.	35
3.4	Pearson correlation coefficients for location Green Mexico: correlation between the mean flight time and other signals. H is a 24 hours periodic signal and other signals are time series of ABL parameters u^* , W^* , L and Z_i	49
3.5	Pearson correlation coefficients for location Wheat Mexico.	49
3.6	Pearson correlation coefficients for location Baja Ca.	50
3.7	Pearson correlation coefficients for location Crops Okla.	50
3.8	Pearson correlation coefficients for location Tobacco NC.	50
3.9	Pearson correlation coefficients for location Crops CA.	50
3.10	Pearson correlation coefficients for location Forest Colorado.	50
3.11	Pearson correlation coefficients for location Veggies WI.	51
3.12	Pearson correlation coefficients for location Wild Canada.	51
3.13	Pearson correlation coefficients for location Wheat Alberta.	51

Chapter 1

Introduction

On April 2010 a serious environmental disaster started: it was going to be the worst in United States history. After the explosion of the Deepwater Horizon, an oil platform of the British Petroleum Company, about 500000 tons of oil were discharged in the Gulf of Mexico with heavy impact on the ecosystem and an estimated economical damage of 17.5 billion dollars.

Every spring, countless numbers of fungal spores fly northward from Mexico, carried by wind in the large-scale atmospheric circulation that interests the North American region. Many of them are pathogens of the main crops cultivated in US and Canada ([1]). Understanding spore transport is crucial to inform decision making, especially to indicate to farmers what is the right time to spray their crops and protect them from devastating pathogenic invasion.

Ocean hydrodynamics affects the distribution of small fish species. For instance, in the Mediterranean Sea the reproductive strategy of the European Anchovy is strongly influenced by the surface currents that carry around eggs and larvae, as investigated in [2] for the particular case of the Sicily channel.

These seemingly unrelated phenomena are all examples of transport in geophysics, carried out either by oceanic or atmospheric currents. In a very general way, we can talk about transport whenever the spatial distribution of a substance changes in time. This definition encloses a wide range of phenomena that belong to very different fields in science and engineering.

Computational power and storage are ever more reliable and affordable. Thanks to advances in both software and hardware, numerical tools became widely available to study transport phenomena in the environment. This is particularly interesting for environmental problems, as experiments in the field are expensive and they can only provide sparse information, whereas numerical models describe the dynamics in a regular grid in space and time. Numerical models are a powerful tool for fundamental scientific inquiry, but they also offer essential assistance for land management in both ordinary and extraordinary situations. Quantitatively understanding geophysical flows, as well as the substances they carry, is challenging. Atmospheric and oceanic flows are typically turbulent, and their dynamics couples a wide range of space-time scales. The full range of

dynamically coupled scales, from the millimeters to thousands of kilometers, is inaccessible to direct numerical simulations. Turbulence is intrinsically chaotic, in that a minor deviation in the initial conditions leads to completely different evolutions. Moreover, the current state of the environment cannot be monitored with sufficient detail.

In this thesis, I will focus on phenomena that depend mainly on the large scales. In these class of problems, numerical simulations can be developed, where the small scales are not resolved but rather parameterized.

The definition of large and small scales depends on the particular application. Different strategies have been developed to model the unresolved scales, which depend on the constraints of the specific application. I will discuss and apply sub-grid models for fungal spore dispersal in the atmosphere and sea surface transport.

Survival strategies in fungal kingdom The first part of my thesis focuses on the large-scale atmospheric transport of fungal spores. Despite the fundamental role of fungi for ecosystems and human activities, this mega-diverse group of species remains largely obscure and understudied. Recently, fungi has received increasing attention, mostly due to the economic impact of fungal pathogens on agriculture. Single species like *Sclerotinia sclerotiorum* can produce billion of dollars of damage per year and similar figures are common to several different pathogenic species on the main food crops (e.g. wheat and rice). In the following, I focus on the North American region, first because this is where meteorological datasets are best resolved. Second because a wealth of information is available on crop disease, and it appears that pathogens travel from Mexico to Canada following large scale atmospheric circulation patterns.

The wheat pathogen *Puccinia graminis* causes stem rust and jeopardizes the harvest causing huge economical losses. This fungus passes the winter in the warm region of Mexico and Southern USA and during the spring it disperses northward, reaching Canada in few months. This dynamics is possible due to the geographical structure of the central USA, characterized by flat terrain, with mountains on either side West and East and affected by mainly northward and southward currents connecting Mexico with Canada. At the same time, this extended region is full of crops, suitable for fungal invasion.

Numerical models have been deployed to study spore transport and spatial dispersal of plant diseases caused by fungi. Some of these studies focus on dynamics at the scale of the canopy, others on transport within the surface layer (the lower part of the planetary boundary layer) and others on regional and global scales ([8], [6] and [7]). In this thesis I focus on spore dispersal in the open atmosphere, i.e. once the spores leave the canopy.

The motivation for studying spore dispersal stems from its importance for fungal survival. Indeed, although fungi are sessile organisms, and have no wings or legs for locomotion, they routinely translocate in space by dispersing their microscopic spores. Most species rely on air currents to transport their spores in the atmosphere. The spectacular mechanisms of spore discharge have been investi-

gated previously and suggest that fungi finely optimize discharge speed (see [3], [4] and [5]). Many species discharge spores at accelerations nearly unmatched in nature, and additionally developed adaptations to sail the spores through the boundary layer surrounding the parent fungus. Spores can then be transported away by atmospheric currents, in their search for a more suitable environment. From the physical point of view, spores are solid particles, characterized by a density, volume and shape which affect their atmospheric transport. Unlike abiotic particles, they have a limited lifespan as their viability depends substantially on temperature, moisture and especially UV exposure during flight. Their survival depends on both physical and biological aspects: to germinate the spores as to survive during the flight and reach a suitable host at the right stage of maturation for the infection. Most of these factors are out of control for a fungus, which can only manage the time for spores liberation.

The fundamental question I want to address here is related to the stochastic nature of turbulent transport: fungi optimize discharge, but the fate of their spores is dramatically affected by stochasticity in atmospheric transport. What can fungi do to positively bias the unknown fate of their spores? The original contribution of my work is to highlight that the initial condition plays a key role in determining spore trajectory. Indeed the time of spore liberation dictates the duration of a spore journey from take-off to landing. This fundamental information suggests that fungi may tune discharge to maximize survival, according to longevity of their particular kind of spore. I conducted a series of numerical simulations for atmospheric transport in North America, using realistic datasets for wind and other meteorological fields. By a statistical analysis of the results, I quantified the duration of spores flight as function of the time of liberation in the environment. I discovered that spores remain in the atmosphere for a timescale that can range from hours until days and even weeks. Because UV light damage can kill a spore in as little as few hours, it is crucial for fungi to correctly time spore ejection to avoid massive die offs. To understand the underlying causes for these widely different flight times, I analyzed the numerical results and found that the dynamical state of the atmospheric boundary layer at the liberation is the crucial parameter. By correlating the statistics of flight time with that of several weather parameters, I determined that stability is the most important driver. This can be understood because close to ground, where spores start their journey, the mean vertical motion is almost zero while turbulent fluctuations may dominate the dynamics, depending on stability of the atmosphere.

This result lays the foundations for further biological inquiry, particularly related to what are the best strategies to sense the micrometeorology and infer the state of atmospheric stability and respond appropriately.

Eddy diffusivities in sea surface transport In the second part of the thesis I study the reliability of eddy diffusivity closures in describing the sea surface dispersion of passive tracers.

As anticipated, the abundance of active dynamical degrees of freedom makes impossible to perform direct numerical simulations of the transport. Even if

our interest is in the large-scale dynamics, the effect of smaller scales cannot be ignored in general. Therefore, to study the behavior of concentration fields on large scales, the standard approach is to solve a transport equation, in which the advection is given by the large-scale velocity of the carrying flow (e.g. the output of a geophysical circulation model like ROMS, MITgcm, WRF, etc.) and the effect of smaller scales is described defining new diffusion coefficients in the diffusive term, namely the eddy diffusivities (ED) (see for example [16], [15]). Differently from standard diffusion, in which the molecular diffusivity is only a property of the involved substances, these redefined quantities depend on the specific features of the carrying flow and thus they should be represented, in general, as tensor fields rather than constants.

The procedure to define the ED is not unique and several levels of accuracy can be adopted. Typical approaches are empirical or semi-empirical, dependent on the specific application and thus conditioned to calibration procedures.

As shown in [20] and [21], a possible way to write the advection-diffusion equation for large-scales evolution is based on the multiple scale perturbative technique. A peculiar consequence of this technique is that, as the large-scale velocity field (resolved by circulation models) is involved in determining the ED field, also the unresolved scales affect the effective advective term in the evolution equation, as a slight correction in the underlying flow velocities, originated from circulation models. Following the theoretical formalism developed in [21], Boi et al. [17] developed new formulas for the ED tensor as function of the resolved velocity components and other parameters related to the unresolved turbulence.

My research in this field is aimed to investigate the reliability of ED closures, in model the sea surface dispersion for realistic applications. The underlying idea is the following: consider as an advective field the output of an oceanographic model, with a very good resolution both in time and space, and assume this field to be a satisfying representation of the real flow. Then apply a spatial filter to this field, obtaining a new advective field with worse resolution, as in the case when the information about the removed scales is not actually available. Finally compare the statistics of dispersion, computed with different descriptions of the unresolved scales, to evaluate what model is more reliable in reproducing the transport in the fully resolved field.

The comparison gives apparently counterintuitive results, suggesting that closures based on an ED approach can eventually overestimate the transport, respect to study the dispersion without any model for the unresolved dynamics. This fact turned out to be related with an effective compressibility of the surface velocity field, that can occur even if the trimensional flow has zero divergence. Even if this result has been obtained for a particular case study, this reveals the necessity to develop an ED model, that can take in to account also the effects of a compressible component in the advective field.

Chapter 2

Fundamental results

In this chapter some fundamental concepts and results related with transport processes, and used in my thesis, are recalled.

2.1 Transport processes

This section deals with the main physical mechanisms involved in transport phenomena. Starting from diffusion and then introducing advective transport, the basic equations to describe the movement of a substance in a fluid are obtained. For a more detailed and deeper presentation consider, for example, [15].

In the context of continuum mechanics, the general problem of transport can be defined introducing the balance law for the dispersed substance. Considering a fixed region with volume V , the balance of an extensive (i.e. depending on the size of the system) physical quantity Q inside this volume is simply expressed by the equality

$$\Delta Q = \Delta Q_E + \Delta Q_P \quad (2.1)$$

that is, the variation of Q in a certain time interval Δt is given by two contributions: the quantity ΔQ_E entered in the volume and the internal production ΔQ_P .

Developing the theory we assume the continuum hypothesis, i.e. that local quantities, defined as the limit of extensive quantities per unit volume when the size of the volume shrinks to zero, are defined in a slightly different sense respect to the ordinary calculus. Indeed the volume has to be

1. sufficiently small in order to consider the extensive quantity Q approximately constant inside it;
2. but large enough for the fluctuations of Q inside the volume to be neglected.

Introducing the vector \mathbf{j} as the amount of Q that cross an infinitesimal surface of area dS and normal unit vector \mathbf{n} during an infinitesimal time interval dt :

$$\delta Q = (\mathbf{j} \cdot \mathbf{n})dSdt,$$

the first contribution can be written as the total flux of \mathbf{j} across the boundary of the region

$$\Delta Q_E = -\Delta t \oint_{\partial V} \mathbf{j} \cdot \mathbf{n} dS.$$

The negative sign is a consequence of defining \mathbf{n} on the boundary as pointing outward of the region. Also the production term can be expressed as

$$\Delta Q_I = \Delta t \iiint_V \xi_Q dV$$

where the production rate of Q has been introduced. Then equation (2.1) can be written as:

$$Q(t + \Delta t) - Q(t) = -\Delta t \oint_{\partial V} \mathbf{j} \cdot \mathbf{n} dS + \Delta t \iiint_V \sigma_Q dV.$$

Now using the divergence theorem to switch the flux integral to a volume integral, dividing by Δt and taking the limit $\Delta t \rightarrow 0$ gives the form

$$\frac{dQ}{dt} = - \oint_{\partial V} \mathbf{j} \cdot \mathbf{n} dS + \iiint_V \sigma_Q dV.$$

that is the balance equation for Q in the integral form.

Moreover, writing the amount of Q inside the region as the integral of its volume concentration θ and taking the time derivative inside the volume integral (that is allowed because the region is fixed in time), leads to the further equation

$$\iiint_V \frac{\partial \theta}{\partial t} dV = - \iiint_V \boldsymbol{\partial} \cdot \mathbf{j} + \sigma_Q dV. \quad (2.2)$$

Finally, since the latter holds for any volume V , the equality holds for the integrands too:

$$\frac{\partial \theta}{\partial t} = -\boldsymbol{\partial} \cdot \mathbf{j} + \sigma_Q \quad (2.3)$$

Equation (2.3) describes the differential form for the balance of Q . This equation is not sufficient to solve the problem of transport, both θ and \mathbf{j} are unknown quantities and further constitutive laws are required to specify the form of \mathbf{j} . Such laws depending on the specific processes involved in the transport.

2.1.1 Diffusion

Diffusion is a very familiar transport phenomenon. Consider, for instance, the behavior of an ink drop released in a still liquid. As time is going on, the drop expands its spatial extension and the color decreases its intensity, finally becoming homogeneously distributed in space. Now look at small solid particles flying in a fluid, like dust in the air. With the help of the sun, their very discontinuous and random flights can be easily observed. It is an example of Brownian motion and it can be explained as the result of all the collisions between

a particle and the microscopic molecules of the surrounding fluid. At macroscopic scales, it turns in to diffusion of dust in to the whole available volume of your room. These are only two of many examples of diffusive processes in our everyday life. Moreover, not only matter can undergo diffusion, but also properties of the fluid (like salinity, temperature, momentum, energy, etc.) can be transported through this mechanism.

To write a differential equation for diffusive processes we have to specify the related form for \mathbf{j} . For diffusion of matter in a fluid, described by the evolution in time of the concentration of matter, the constitutive law is due to the work of the german physiologist Fick. From experimental observations he found out that

1. the flux of matter is a function of the gradient of concentration: $\mathbf{j} = \mathbf{f}(\nabla\theta)$;
2. diffusive processes are isotropic, i.e. they doesn't have a preferential direction;
3. diffusive processes are homogeneous, i.e. they are invariant for spatial translations;
4. \mathbf{f} is linear.

From these four features the Fick's law can be written as:

$$\mathbf{j} = -D_0\partial\theta$$

where D_0 is the molecular diffusivity, a property of the substances involved in the diffusive process. The minus sign comes from the additional experimental evidence that diffused matter flows in order to reduce the concentration gradient, from high to low concentration areas. To write the diffusion equation it is sufficient to substitute the Fick law in equation (2.3):

$$\frac{\partial\theta}{\partial t} = -\partial \cdot (-D_0\partial\theta) + \sigma_Q$$

and then, being D_0 a constant:

$$\frac{\partial\theta}{\partial t} = D_0\partial^2\theta + \sigma_Q \quad (2.4)$$

It is noteworthy that equation (2.4) has the same mathematical form of the Fourier's equation of heat.

Fundamental solutions of the diffusion equation

It is easily verified that, without sources ($\sigma_Q = 0$), the function

$$G(\mathbf{x}, t) = \frac{1}{(4\pi D_0)^{3/2}} e^{-r^2/(4D_0t)}$$

is a solution of the diffusion equation, where $r^2 = \sum_i x_i^2$. The function $G(\mathbf{x}, t)$ represents a tridimensional Gaussian centered in the origin with variances

$$\sigma_i^2 = 2D_0t$$

Then the size of the distribution increases as \sqrt{t} with velocity decreasing as $1/\sqrt{t}$. Moreover the G function approximates the Dirac's delta distribution as $t \rightarrow 0$, hence it is a solution of the homogeneous diffusion equation with initial condition $\theta(\mathbf{x}, 0) = \delta(\mathbf{x})$. It is also called the *Green's function* or the *fundamental solution* for the diffusion equation and, thanks to the superposition principle, the general solution can be written in terms of this function. Hence purely diffusive processes are quite simple to describe.

2.1.2 Advection

Typical values for D_0 are of the order of $10^{-5} \frac{m^2}{s}$, hence molecular diffusion is very common but also very slow as a transport process. Taking, for example, a source of smell and sitting 1 meter away from the source, we could wait to feel it, more than three hours from the emission. This time is significantly reduced if the smell is transported also by advection.

If the substance is immersed in a fluid in motion with a velocity field $\mathbf{v}(\mathbf{x}, t)$ and considering the substance as a passive tracer, then a further contribution arises in the density current due to advection:

$$\mathbf{j} = \mathbf{v}\theta$$

Adding this new contribution in the balance law gives the following differential form:

$$\frac{\partial \theta}{\partial t} + \boldsymbol{\partial} \cdot (\theta \mathbf{v}) = D_0 \partial^2 \theta + \sigma_Q$$

Finally, if the carrying field is also incompressible (and then with zero divergence), as can usually be assumed in geophysics, the equation becomes:

$$\frac{\partial \theta}{\partial t} + \mathbf{v} \cdot \boldsymbol{\partial} \theta = D_0 \partial^2 \theta + \sigma_Q. \quad (2.5)$$

Furthermore, if we relax the requests on the diffusive process, removing the conditions of isotropy and homogeneity, an advection-diffusion equation can be written again, but now the diffusion coefficient is not simply a constant, becoming in general a tensor field.

2.2 The Lagrangian approach

Up to now the transport problem has been introduced looking at the concentration field $\theta(\mathbf{x}, t)$, that is the Eulerian framework. Equivalently we can use the Lagrangian approach, that consists in following trajectories of transported particles.

We start to handle particle trajectories with a very simple but fundamental case, the Brownian motion of particles in a still fluid. A particle of the immersed substance undergoes a lot of collisions with the smaller molecules of the surrounding fluid (animated by thermal agitation) which transfer momentum to the particle, that turns in to a random velocity, like for dust flying in the room. Hence we can write the equation of motion for the dust particle as:

$$\dot{x}(t) = \sqrt{2D_0}\eta(t) \quad (2.6)$$

where I consider the unidimensional case for simplicity. Here $\eta(t)$ is a stochastic process whose realizations determine at each time step the velocity of the particle (for a good presentation on stochastic processes see [31]). Moreover we assume that:

1. $\langle \eta(t) \rangle = 0$, i.e. a single particle has a zero velocity on average or, alternatively, the mean velocity over an ensemble of particles is zero;
2. $\langle \eta(t)\eta(t') \rangle = \delta(t - t')$, i.e. different realization of the process, arbitrary close in time, are uncorrelated.

With these hypotheses we can formally write the solution of eq. (2.6) as

$$x(t) = x_0 + \sqrt{2D_0} \int_0^t \eta(t') dt',$$

where x_0 is the initial position of the particle. Even if we cannot integrate $\eta(t)$ that is not a function, we can evaluate statistics of the random variable x such

$$\langle x(t) \rangle = \langle x_0 \rangle + \sqrt{2D_0} \int_0^t \langle \eta(t') \rangle dt'.$$

Here we used the fact that the average operator commutes with the integral. Now, because of hypothesis 1 we find that $\langle x - x_0 \rangle = 0$. Considering now the variance

$$\langle (x - x_0 - \langle x - x_0 \rangle)^2 \rangle = \langle (x - x_0)^2 \rangle = 2D_0 \int_0^t dt' \int_0^t dt'' \langle \eta(t')\eta(t'') \rangle = 2D_0 t$$

where we used the properties of the delta distribution. In analogy with the fundamental solution of the eulerian diffusion problem we recognize that the variance grows linearly in time.

Now consider the evolution of the probability density $P(x, t)$ that the Brownian particle can be found around point x at instant t . The probability density $P(x, t + \Delta t)$ that the particle is found close to x at time $t + \Delta t$ can be evaluated by summing over all its possible positions x' at time t . Then $P(x, t + \Delta t)$ is given by the integral over x' of the probability density $P(x', t)$ that the particle was found at x' at time t , times the conditional probability $P(x, t + \Delta t | x', t)$, that starting from x' at time t , it reaches x at time $t + \Delta t$:

$$P(x, t + \Delta t) = \int dx' P(x, t + \Delta t | x', t) P(x', t). \quad (2.7)$$

We found that, in a time interval Δt , a Brownian particle undergoes a displacement $\Delta x = x - x'$ whose average vanishes and whose variance is equal to $2D_0\Delta t$. We will denote the distribution of this displacement by $\phi(\Delta x)$. If Δt is small enough, we can expand $P(x', t)$ on the right-hand side of equation (2.7) in a Taylor series in powers of Δx around the x point. Changing the integration variable to Δx , we obtain

$$P(x, t + \Delta t) = \int d(\Delta x)\phi(\Delta x) \left[P(x, t) - \Delta x \frac{\partial P}{\partial x'} \Big|_x + \frac{1}{2} \Delta x^2 \frac{\partial^2 P}{(\partial x')^2} \Big|_x + \dots \right]$$

Because Δx vanishes on average, the second term in the right hand side vanishes too and we can write:

$$P(x, t + \Delta t) = P(x, t) + D_0 \Delta t \frac{\partial^2 P}{\partial x^2} + o(\Delta t)$$

and finally, taking the limit for $\Delta t \rightarrow 0$ we found that the probability density P satisfies the diffusion equation

$$\frac{\partial P}{\partial t} = D_0 \frac{\partial^2 P}{\partial x^2},$$

with the identification of D_0 with the molecular diffusivity introduced in the Eulerian framework.

The procedure that we used to show the connection between Brownian motions and molecular diffusion can be generalized. Particularly, in the case of Lagrangian particles whose velocity is given by the sum of a random component and an advective deterministic one $\mathbf{v}(\mathbf{x}, t)$:

$$\dot{\mathbf{x}} = \mathbf{v}(\mathbf{x}(t), t) + \sqrt{2D_0}\boldsymbol{\eta}(t),$$

it can be proved (see for example [30]), that the corresponding Eulerian equation is the advection-diffusion equation (2.5):

$$\frac{\partial \theta(\mathbf{x}, t)}{\partial t} + \mathbf{v} \cdot \boldsymbol{\partial} \theta(\mathbf{x}, t) = D_0 \partial^2 \theta(\mathbf{x}, t).$$

Also dealing with a generalized diffusive process it can be proved that the Eulerian equation:

$$\frac{\partial \theta(\mathbf{x}, t)}{\partial t} + \boldsymbol{\partial} \cdot (\mathbf{v}(\mathbf{x}, t)\theta(\mathbf{x}, t)) = \partial_i \partial_j D_{ij}(\mathbf{x}, t)\theta(\mathbf{x}, t).$$

is equivalent to

$$\dot{\mathbf{x}} = \mathbf{v}(\mathbf{x}(t), t) + \sqrt{2D_{ij}}\boldsymbol{\eta}(t),$$

where the square root of a matrix is not ambiguous as D_{ij} is assumed to be positive definite.

This fact is very important as the theoretical support for Lagrangian simulations performed in my thesis work.

2.3 Turbulence

Either using a Lagrangian or an Eulerian approach, there is a physical problem in studying the transport of matter: we have to tackle the dynamical complexity of turbulence. This phenomenon can be very relevant, especially dealing with geophysical flows. It is a well known experimental fact that, in a given system, laminar flows are stable only up to certain critical values of the typical velocity. These values change for different systems and depend from the geometry and the physical properties of the fluid.

Over these critical velocities instabilities arise, becoming chaotic with significant fluctuations. Chaotic motions are always present at the molecular scales, also when the macroscopic flow is stationary. Hence perturbations of the flow are always present but these perturbations are suppressed or limited if the flow is neutral or stable. Otherwise perturbations grow up becoming comparable with the base flow.

Turbulence is due to nonlinear advective terms in the Navier-Stokes equations. The relative importance of such nonlinear terms respect to the viscous term can be measured by a dimensionless parameter, the Reynolds number

$$Re = \frac{U^2/L}{\nu U/L^2} = \frac{UL}{\nu} \quad (2.8)$$

where U , L and ν are the typical velocity of the fluid, the characteristic length scale and the kinematic viscosity. Critical values of the Reynolds number for transitions from laminar to turbulent regimes, can vary very much, with cases in which the flow can persist in a laminar state up to $Re > 100.000$.

In geophysics Reynolds numbers are very high, consider for example an important geophysical phenomenon like the Gulf stream. It has a typical velocity of $1 \frac{m}{s}$, a width of about $100 km$. Assuming $\nu \sim 10^{-6} m^2 s^{-1}$, the Reynolds number reaches values of

$$Re = \frac{UL}{\nu} = \frac{1 \times 10^5}{10^{-6}} = 10^{11}$$

then the flow is typically turbulent, as usual in ocean and atmosphere.

As a strongly nonlinear process, turbulence is chaotic and hence a deterministic description of turbulent systems is impossible. The standard approach consists in considering the involved physical quantities as random variables. The idea, due to Reynolds, is to consider an ensemble of many identical systems and to decompose all the dynamical variables in the sum of two terms, the ensemble average $\langle \xi \rangle$ and the fluctuation ξ' :

$$\xi = \langle \xi \rangle + \xi'$$

Introducing such decomposition in the fundamental equations allows to write the evolution equations for the averaged quantities (a detailed description of the procedure can be found in [12]). I report here the result of the substitution for the fundamental equations (the average components of the velocity field are indicated as $\langle u_i \rangle = U_i$:

- the continuity equation:

$$\frac{\partial U_i}{\partial x_i} = 0;$$

- the Navier-Stokes equation (RANS: Reynolds averaged Navier-Stokes equations):

$$\frac{dU_i}{dt} = -\frac{1}{\rho} \frac{\partial P}{\partial x_i} + \frac{\partial}{\partial x_j} \left[\nu \frac{\partial U_i}{\partial x_j} - \langle u'_i u'_j \rangle \right] + g_i \quad (2.9)$$

Notice that the mean values evolution equations are not completely decoupled from fluctuations because there is a nonlinear interaction between the two components. The effect of this interaction on the mean flow equations is represented by the correlations $\langle u'_i u'_j \rangle$. This correlations can be included in a redefinition of the stress tensor $\langle \tau_{ij} \rangle$ for the mean flow:

$$\langle \tau_{ij} \rangle = -P \delta_{ij} + \mu \left(\frac{\partial U_i}{\partial x_j} + \frac{\partial U_j}{\partial x_i} \right) - \rho \langle u'_i u'_j \rangle$$

Then in addition to the mean stress there is a new tensor, the *Reynolds' stress tensor* that can be written in matrix form as

$$R = -\rho \begin{pmatrix} \langle u'u' \rangle & \langle u'v' \rangle & \langle u'w' \rangle \\ \langle v'u' \rangle & \langle v'v' \rangle & \langle v'w' \rangle \\ \langle w'u' \rangle & \langle w'v' \rangle & \langle w'w' \rangle \end{pmatrix}.$$

Notice that, to close the mathematical problem, we need to express this stress tensor in terms of the mean flow, this is called the *closure problem* and the way to describe this interaction is not unique.

- the advection-diffusion equation for passive scalar transport:

$$\frac{\partial \langle \theta \rangle}{\partial t} + \langle \mathbf{u} \rangle \cdot \boldsymbol{\partial} \langle \theta \rangle = -\boldsymbol{\partial} \cdot \langle \theta' \mathbf{u}' \rangle + \boldsymbol{\partial} \cdot (\kappa_\theta \boldsymbol{\partial} \langle \theta \rangle),$$

where $\langle \theta' \mathbf{u}' \rangle$ represents the turbulent transport, often empirically described by the *K-theory*, according to which

$$\langle \theta' \mathbf{u}' \rangle = -K \boldsymbol{\partial} \langle \theta \rangle,$$

where K can be in general a tensor (*Turbulent diffusion tensor*) and its elements have to be deduced from experimental data or given by models.

This Reynolds averaging procedure is very important because, most of the numerical models that produce advective fields for transport models uses this approach to compute the dynamics.

2.4 Homogeneization

We saw as the presence of turbulence involves too many degrees of freedom to be completely described and as, in the context of RANS, the Reynolds stress tensor enters in the dynamics of the mean flow with the related problem of closure. The choice to close the problem assuming the turbulent fluxes as diffusive (K-theory) is only a possible assumption. Anyway, starting from the advection-diffusion equation

$$\partial_t \theta(\mathbf{x}, t) + \mathbf{v}(\mathbf{x}, t) \cdot \boldsymbol{\partial} \theta(\mathbf{x}, t) = \partial^2 D_0 \theta(\mathbf{x}, t). \quad (2.10)$$

and using the homogeneization technique of multi-scale perturbation theory, It is possible to obtain again an advection-diffusion equation for the pre-asymptotic behavior of the large-scale component of the concentration field. The following theory has been developed in [20] and [21]. Biferale and alt. found that, for a passive tracer in a periodic advective velocity field, the asymptotic behavior of the large-scale scalar concentration, in the reference frame of the mean flow, is diffusive. Indeed they started from equation (2.10) and, expressing the concentration field as a perturbative multi-scale series, they obtained the following asymptotic equation for the large-scale field $\langle \theta_0 \rangle$:

$$\partial_T \langle \theta_0 \rangle = D_{ij}^E \nabla_i \nabla_j \langle \theta_0 \rangle$$

where D_{ij}^E is a positive-definite tensor that is named *Eddy Diffusivity tensor*. With the same technique, Mazzino and alt. obtained the preasymptotic equation. They separated the advective field in the sum of a large scale \mathbf{U} and a small scale \mathbf{u} component:

$$\mathbf{v} = \mathbf{U} + \mathbf{u}.$$

The idea is to identify \mathbf{U} with the part of the advective field that are known in realistic applications and \mathbf{u} with the subgrid unresolved scales. Here the term *preasymptotic* indicates to the evolution of the scalar field on the same scales of \mathbf{U} . Then the resulting equation is

$$\partial_t \Theta(\mathbf{x}, t) + \mathbf{U}(\mathbf{x}, t) \cdot \boldsymbol{\partial} \Theta(\mathbf{x}, t) = \partial_i [D_{ij}(\mathbf{x}, t) \partial_j \Theta(\mathbf{x}, t)].$$

where now $\Theta(\mathbf{x}, t)$ is the large scale concentration field. The tensor D_{ij} is neither simmetryc nor positive-definite, hence the equation can be written in terms of its symmetric part:

$$\partial_t \Theta(\mathbf{x}, t) + \partial \cdot [\mathbf{U}^E(\mathbf{x}, t) \Theta(\mathbf{x}, t)] = \partial_i \partial_j [D_{ij}^E(\mathbf{x}, t) \Theta(\mathbf{x}, t)] \quad (2.11)$$

where

$$U_i^E(\mathbf{x}, t) \equiv [U_i(\mathbf{x}, t) + \partial_j D_{ij}(\mathbf{x}, t)], \quad D_{ij}^E(\mathbf{x}, t) \equiv \frac{D_{ij}(\mathbf{x}, t) + D_{ji}(\mathbf{x}, t)}{2}.$$

The main result of the preasymptotic theory is to obtain, directly from the fundamental laws, an equation for the large-scale concentration that still has the form of an advection-diffusion equation. This fact is very relevant for my work, particularly for chapter 4 in which I study the transport on the sea surface using the Lagrangian counterpart of the Eulerian equation 2.11.

2.5 Anomalous diffusion

In previous sections we saw that, typically, the role of the smaller scales in the advective field is to diffuse tracer particles, with effective diffusion coefficients that take the name of eddy diffusivities. A footprint of this kind of dynamics is that the variances of particles' displacements evolve linearly for large times:

$$\langle (x(t) - x(0))^2 \rangle \rightarrow 2D^E t,$$

that is analogous to the case of Brownian motions, but here the molecular diffusivity D_0 has been replaced with the eddy diffusivity D^E . All the effects due to the unresolved scales in the advective velocity field are summarized in the eddy diffusion coefficient.

In some cases, nontrivial small-scale dynamics can lead to a different behavior and anomalous diffusion is observed. This phenomenon occurs when variances of the displacement show a different time evolution, i.e.,

$$\langle (x(t) - x(0))^2 \rangle \sim t^{2\nu},$$

with $\nu \neq \frac{1}{2}$. Particularly the case when $\nu < \frac{1}{2}$ corresponds to subdiffusion, that occurs only in compressible fields and is basically due to trapping effects, while, when the field is incompressible and the molecular diffusivity is nonzero, either superdiffusion $\nu > \frac{1}{2}$ or standard diffusion takes place. This kind of phenomena has been largely studied in different systems and with several techniques, see for example [13] and [14].

Chapter 3

Survival strategies in fungal kingdom

Dispersal processes are very important because of their influence on survival of many biological organisms. A multitude of species of plants and fungi use airborne pollen and spores to move and reproduce. Serious virulent pathologies, like the Foot and Mouth disease of cloven-hoofed animals, spread through abiotic aerosols. Biological tracers like larvae are transported by oceanic currents and are significantly affected by turbulence.

In this chapter I discuss biological issues related with the large-scale dispersal of fungal spores in the atmosphere and I present the results of numerical simulations aimed at understanding the duration of a spore flight in the atmosphere.

3.1 Fungal spore dissemination

Despite its abundance and economical impact the fungal kingdom is still largely unexplored, only few percent of the estimated 1 to 8 million of fungal species have been described. Fungi play key roles in nature, from decomposers, symbionts, parasites and pathogens and are simultaneously among the worst threats and the most fundamental components of many ecosystems. As a fundamental feature fungi are heterotroph organisms; differently from plants they are not capable of photosynthesis and hence need to feed on dead matter or live in symbiosis with hosts to obtain the nutrients that are necessary for their survival. In geographical areas subjected to a temperate climate suitable hosts are only available in short periods along the year depending on suitable environmental conditions, especially temperature. Similarly, within the tropical zone the presence of resources is limited in time, in this case the driving factor is the alternation of very dry with very wet and rainy phases. Best conditions for fungal hosts growth are found in subtropical or prosperous tropical areas. Here fungi can count on resources all year around, yet suitable patches of resources are discontinuously distributed in space. After a fungus established on a host it starts to increase its biomass developing the *mycelium*, its vegetative apparatus, that is made up of many filamentous structures called *hyphae*. Even in best cases the resources supply is finite in time and fungi have no legs or any locomotive apparatus to

translocate to new favorable habitats. To face this challenge fungi developed different mechanisms. Some species evolved specific structures called *sclerotia*: a conglomerate of compact mass of hardened fungal mycelium containing food reserves. In this form fungi can survive severe winters until favorable growth conditions return. In some cases mycelia can stay dormant inside plant seeds.

The most prominent mechanism for survival is spreading of fungal spores. Differently from sclerotia and seeds, spores are very small and light hence large numbers can be stored in few space and carried around by wind, making dissemination very effective. Production, storage, liberation and single spore features are very peculiar of individual species. Fungi can perform either sexual or asexual reproduction and consequently genetic pool of the offspring may be homogeneous or diverse. Some species choose the tissues of infected hosts as storing place, others let spores rest externally, others develop new structures called fruit bodies whose shape is very different from species to species. Typical spore size is of the order of magnitude of one to ten microns and then countless numbers can be produced and packed in a little space: as examples the ordinary corn smut fungus produces almost a billion spores in a cubic centimeter of infected tissue and there are about 70000 million spores of *Puccinia graminis* at one time on a heavily rusted bush of barberry of few meters. Moreover a fungus can produce many generations of spores employing just one week more or less between consecutive ones. Prolificacy is crucial for the survival but longevity of spores is fundamental too, due to the aforesaid time and space discontinuity of resources fungal spores has to survive after land in a dormant state before germination in order to wait hosts at a proper stage to establish on and in many cases they are able to survive unfavourable seasons under certain conditions. Also the viability during flight is important since spores are exposed to severe temperatures, moisture and most importantly UV-ray. Another aspect of fungal dispersal is the spectacular mechanisms for spore liberation: when stored externally these corpuscle are typically detached by movement or passively released and they abandon the fungus by settling. However, the majority of fungi, about 75% of described species, produces spores inside fruit bodies made of thousands of microscopics sacs, called *asci*, that act like cannons powered by osmotic pressure [4], [5]. Although these fungal cannons are optimal and realize accelerations of order 10^5g , nearly unmatched in nature, the launch speed may not be enough to get the spores through the boudary layer of still air around the fruit body. The fungi developed a myriad adaptations to solve this problem. For example, thousand of species synchronise ejections of their spores to mobilize the air right next to the fruit body and create a jet of air that travels much further than isolated spores. As consequence of this refined optimization these fungi increase the probability for a spore to exit the stagnant boundary layer around the fruit body and to be carried away by wind. Depending on the particular case, the dissemination by wind can interest a very wide range of spatial scales, from local, to regional, to intercontinental. It is a well established fact that airborne spores can reach very great heights and distances from the source: the observations, made on balloon traps and airplanes, reveal the presence of fungal spores at altitudes of more

than 4000 meters over infected crops or above the Caribbean Sea, about 1000 km from the nearest possible source. In addition, to be effective, spores traveling high in the atmosphere have to come to the ground and they accomplish this either through vertical downdrafts, possibly caused by storms and rain, or by sedimentation. Sedimentation velocities typically range from 0.5 mm/s to 20 mm/s in dry air conditions but could be increased by factors of about 2 or 3 in wet conditions and rough estimations of deposition distances from the source easily give values about thousand of kilometers. On the contrary other situations show dissemination on the shorter scales of the forest, the orchard or the single crop.

Analyzing this wide range of possibilities mycologists started to classify dissemination processes according to their extent then introducing the concepts of *Long distance dissemination* (LDD) and *Short distance dissemination* (SDD). Different species have developed essentially different strategies: some species spread their spores on local scales and other species spread their spores to regional and even continental scales, whence spores fly for weeks before landing. Clearly the latter spores must be well adapted for atmospheric transport and particularly resistant to meteorological agents. An important challenge for spore dispersal is that fungi often need specific hosts at the right condition that are sparsely distributed in space. Consider, for example, pathogens of certain specific crops in regions with high diversification of agricultural activities.

Ultimately the relative success or failure of a survival strategy is determined by several factors: the amount of spores produced; the release mechanism; the resistance either during flight or after landing; the abundance, the extent and timeliness of dissemination; and the state of a possible host in order to germinate. From the point of view of the fungus, the fate of its spores is uncertain. Crucially, in this highly stochastic scenario, fungi can only control the initial condition, i.e. the time for spore release. A number of physical and evolutionary questions arise: What is the role of the initial condition for the trajectory of the spores in the atmosphere? What is the best timing to release spores? Can fungi release spores to maximize their probability of survival? As shown by my research the answer to this questions can vary essentially among species and different survival strategies have to be developed.

Different strategies are needed because of the different biological constraints. Some species evolved particularly resistant spores, e.g. by developing pigments that protect the spores from UV light exposure. Spores of the wheat pathogen *Puccinia graminis* can remain viable in the atmosphere for weeks. On the other hand, some species have more fragile spores, that die after few hours of exposure to UV light. Spores need to sediment before they die: flight time must be strictly smaller than survival times. In the following I elucidate what are the best strategies to ensure that this constraint is satisfied.

3.2 Describing spore dispersal

Fungal spores have no legs or fins for locomotion and are carried around passively by wind. Hence in describing their motion they can be considered as particles subject to external forces. The starting point to study the dispersal of fungal spores is the equation of motion for a single spore. Newton's second law reads:

$$M\mathbf{g} - \rho_{Air}V\mathbf{g} + \eta(\mathbf{V}_{Wind} - \mathbf{u}) = M\mathbf{a} \quad (3.1)$$

where M , V , \mathbf{u} and \mathbf{a} are mass, volume, velocity and acceleration of a spore. On the left hand side gravity, Archimede's force and the effect of the moving fluid surrounding the spore are taken into account. The last term works to make spores travel at the same speed of the surrounding air \mathbf{V}_{Wind} in the neighbourhood of spore position $\mathbf{x}(t)$; the dimensional parameter η sets the strength of this term and can be determined in the particular case in which the spore falls down in still air [23]. The equation of motion can be written in term of the Stokes time $\tau_S := \frac{M}{\eta}$,

$$\beta\mathbf{g} + \frac{(\mathbf{V}_{Wind} - \mathbf{u})}{\tau_S} = \mathbf{a} \quad (3.2)$$

where $\beta := 1 - \frac{\rho_{Air}}{\rho_S}$ is a dimensionless parameter and ρ_S is spore density. The Stokes time represents the characteristic response time over which a spore reacts to accelerations of the surrounding fluid. Air density in normal conditions is about 1.225 kg/m^3 and spore densities have been measured for many kinds of spores belonging to different species [24]. In some cases it is very close to water density because of the high water content of some species, from 50% to 75%. For other species this water content is smaller, from 6% to 25% but anyway, taking $\beta \sim 1$ is found to be a good approximation for all species.

Looking at the non-dimensional form of the previous equation and being U and T respectively the characteristic velocity and time (typically the Kolmogorov time scale of a turbulent atmosphere), it can be found that, if

$$\tau_S \ll T; \quad \beta g \gg \frac{U}{T},$$

then the acceleration in equations 3.1 and 3.2 can be neglected and finally fungal spores can be treated as passive tracers with an additional gravitational settling velocity $V_G := g\beta\tau_S$:

$$\frac{d\mathbf{x}(t)}{dt} = \mathbf{V}_{Wind}[\mathbf{x}(t), t] + \mathbf{V}_G, \quad (3.3)$$

Table 3.1 gives an overview of the involved parameters for some fungal species: As mentioned before, the Stokes time and therefore the gravitational settling velocity can be determined considering the case of a spore falling down in still air. For spherical particles for example it gives:

$$\tau_S = \frac{2}{9} \frac{\rho_S r^2}{\mu}$$

where $\mu = 1.81 \cdot 10^{-5} \text{ Pa} \cdot \text{s}$ is the dynamical viscosity of air and r is the radius of the spore.

Table 3.1 – Physical spore parameters

Species	size [μm]	density [$\frac{g}{cc}$]	Stokes time [s]
<i>puccinia graminis</i>	28.3 (length)	0.47	$1.78 \cdot 10^{-3}$
	17.5 (width)		
<i>sclerotinia sclerotiorum</i>	12 (length)	0.44	$1.95 \cdot 10^{-4}$
	6 (width)		

3.3 Numerical study

In order to understand the influence of the spores release time on the survival strategies of fungi, I conducted a numerical study of atmospheric dispersal using real meteorological datasets. For this purpose the dispersal has been studied following a Lagrangian approach, i.e. following the trajectories of each spore according to eq. 3.3. Note that I am focusing here on the large scales and the effect of the unresolved dynamics has to be properly modeled.

Spores are microscopic objects but their trajectory spans large scales, reaching hundreds of kilometers. The entire range of coupled space-time scales cannot be fully resolved: meteorological data are available on a 12 km grid, and subgrid models account for additional fluctuations with an eddy viscosity model and phenomenological expressions for the eddy viscosity.

3.3.1 The meteorological dataset

Numerical models for dispersal processes need advective fields as input. Typically this information comes from other numerical models, run to solve the Navier-Stokes equation under appropriate conditions, together with the continuity equation, the equation of state for air and other additional equations that account for peculiar processes of the atmosphere such as cloud microphysics, etc. In my research about fungal spores dispersal I used a wide dataset, the North American Regional Reanalysis (NARR)[28], produced by the National Centers for Environmental Prediction (NCEP) of the National Oceanic and Atmospheric Administration (NOAA)[29], a US government department, and publicly available. The dataset is a reanalysis, the result of a procedure of matching between regularly gridded fields, produced by atmospheric models, and sparse observations assimilated from meteorological stations, balloons, airplanes, satellites, etc. This multiple contribution makes the reanalysis our best knowledge of the state of the atmosphere at a certain time. The NARR is a regional reanalysis of North America, from Mexico to Canada, containing temperatures, winds, moisture, soil data, and dozens of other parameters. The main data that are assimilated, in order to initialize the model to real-world conditions, are temperatures, winds, and moisture from radiosondes as well as pressure data from surface observations. Also included in this dataset are dropsondes, pibals, aircraft temperatures and winds, satellite radiance (a measure of heat) from polar (orbiting Earth) satellites, and cloud drift winds from geostationary (fixed at one location viewing

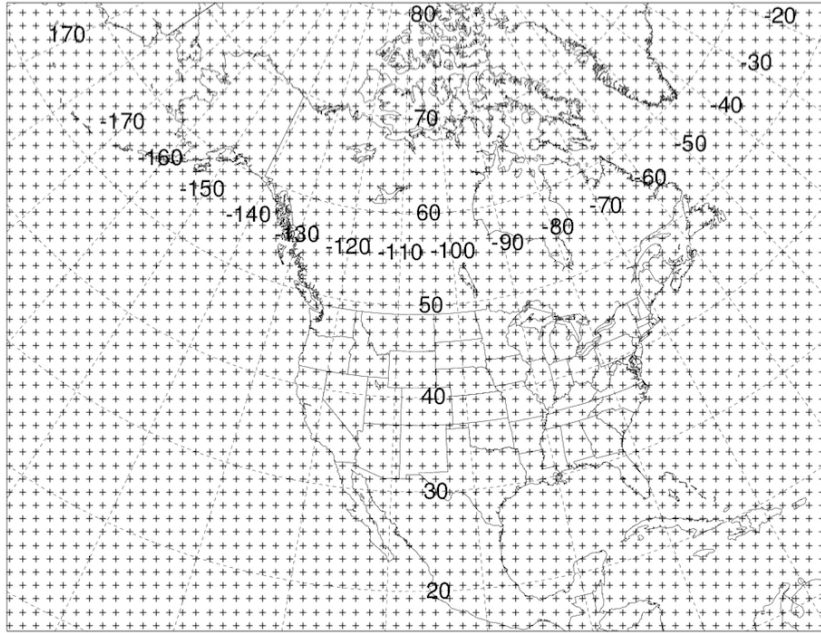


Figure 3.1 – Geographical domain of North American Regional Reanalysis (NARR): the dataset covers the entire area of the continent in the northern hemisphere, from Mexico to Canada across the United States. Grid points on which meteorological variables (like wind velocity) are known are plotted one every five, the actual horizontal resolution is about 32 km.

Earth) satellites. An important contribution is given by the assimilation of precipitation data coming from a very dense network of various sources. The NARR grid is a Lambert conformal grid with 309 x 237 horizontal point and 24 levels on vertical pressure-sigma coordinates system. The horizontal resolution is about 32 km. The described time period start from 1979 to today and the state of the atmosphere is available with a sampling time of 3 hours.

3.3.2 Numerical techniques.

To perform simulations I used the Hybrid Single Particle Lagrangian Integrated Trajectories (HySPLIT) model. It is a FORTRAN code, developed at the Air Resource Laboratory (ARL) of NOAA and largely adopted in the scientific community to study dispersal phenomena in the atmosphere. In addition to the computation of atmospheric transport, this code has the possibility to describe different kind of deposition processes, chemical reactions, particle resuspension and radioactive decays. In the following I present only the main numerical features of the code related with simulations performed in this thesis, for a complete overview on HySPLIT and the related technical bibliography, refer to the HySPLIT technical guide, available from the web [25].

HySPLIT is conceived with a Lagrangian approach, it solves the equation of motion for each particle of the dispersed substance according to the wind speed and the gravitational settling as pointed out in section 3.2. Moreover, since from

NARR the wind field is given with a 32 km resolution, all the information about the unresolved scales has to be modeled. Hence the contribution of wind velocity to the trajectory of each particles is splitted in advection by resolved wind speed and effective diffusion by subgrid turbulence given by a proper model.

Stability computation

A preliminary and fundamental step in computing particle's evolution is the evaluation and quantification of atmospheric boundary layer (ABL) stability at each particle location. This step is very important in order to choose the proper modelization for turbulent velocities that substantially affect the dispersion process. Here I recall only notions that are strictly related with this thesis, several specific texts exist for a deeper description about the subject, like [26] and [27].

If stability could be measured through several quantities HySPLIT uses the computation of the *Monin-Obukhov length* L , that is a dimensional parameter related with the stability of the surface layer, the lower part of the ABL. It is positive or negative when the ABL state is respectively stable or unstable. The expression for L is

$$L = -\frac{(u^*)^3}{kg \frac{\langle w'\theta' \rangle}{\theta}}.$$

The parameter $u^* = [\langle u'w' \rangle^2 + \langle v'w' \rangle^2]^{\frac{1}{4}} = |\frac{\tau_s}{\rho}|^{\frac{1}{2}}$, called the *friction velocity*, is related with the turbulent stress at the surface τ_s and the air density ρ , and the covariances $\langle u'w' \rangle$ and $\langle v'w' \rangle$ are the kinematic momentum fluxes at the surface. In the denominator g is the gravity acceleration, $k = 0.4$ is the von Karman constant, θ is the potential temperature and $\langle w'\theta' \rangle$ is proportional to the turbulent heat flux at the surface. From a physical point of view L measures the relative contributions to turbulent kinetic energy given by buoyant production and shear production, representing the height at which these two contributions are equal. During unstable conditions another velocity scale can be introduced, the convective velocity $W^* = [\frac{gZ_i}{\theta} \langle w'\theta' \rangle]^{\frac{1}{3}}$, where Z_i is the boundary layer depth, that is another important parameter involved in the computation of turbulent motions. HySPLIT assumes Z_i to be the height at which the potential temperature exceeds the ground value by 2 °K (starting from the top and going down). A minimum depth of 250m, is assumed (probably overestimating night time ABL thickness). If the turbulent kinetic energy (TKE) field is available from the meteorological dataset the mixed layer depth can also be computed from the TKE profile instead of the temperature profile. In this case the mixed layer depth is assumed to be the height above the ground at which the TKE drops by more than half of its previous value.

Stability can be studied through different procedures, depending on the information carried by the meteorological data used. If surface heat and momentum fluxes are not available, as in the case of NARR dataset, the stability is estimated from wind and temperature profiles according to the following steps:

- preliminary evaluation of the bulk Richardson number

$$R'_b = \frac{g\Delta\theta\Delta Z}{\theta_{12}[(\Delta u)^2 + (\Delta v)^2]}$$

where Δ indicates the gradient between levels 1-2 of the internal grid and θ_{12} is the related layer-average potential temperature;

- possible correction for very coarse vertical spacing data files (if the values at Z_2 comes from linear interpolation from external meteorological data level at a height Z_d is much greater than Z_2):

$$R_b = R'_b \left(\frac{Z_2}{Z_d} \right)^2 ;$$

- from R_b , estimation of the ratio $\frac{z}{L}$, evaluated at the top of the surface layer, by using empirical interpolation formulas:

$$\frac{z}{L} = R_b \left(\frac{s^2}{t} - 0.50 \right), \quad R_b \leq 0$$

$$\frac{z}{L} = \frac{-t + 2s\beta R_b(t^2 - 4st\beta R_b + 4s^2\beta R_b)^{\frac{1}{2}}}{2\beta(1 - \beta R_b)}, \quad 0 \leq R_b < 0.08$$

$$\frac{z}{L} = (0.005s + 41.2)R_b^2 + (1.18s - 1.5v - 1.37)R_b, \quad R_b \geq 0.08$$

being

$$s = \ln \frac{z}{Z_o} + 1.0$$

$$t = \ln \frac{z}{Z_h} + 1.0$$

$$v = \ln \frac{Z_o}{Z_h}$$

where Z_h is the roughness length for heat and Z_o is the roughness length for momentum, taken such that $\frac{Z_o}{Z_h} = 10$, and $\beta = 5$ is a parameter;

- computation of friction velocity and temperature:

$$u^* = \frac{kZ_2\Delta u}{\phi_m\Delta Z}$$

$$T^* = \frac{kZ_2\Delta\theta}{\phi_h\Delta Z}$$

where ϕ_h and ϕ_m are the normalized profiles for heat and momentum defined as follows in both the stable case $0 \leq \frac{z}{L} \leq 15$

$$\phi_m = 1 + \frac{z}{L} \left[a + be^{-d\frac{z}{L}} \left(1 - d\frac{z}{L} + c \right) \right]$$

$$\phi_h = Pr_n \left\{ 1 + \frac{z}{L} \left[a\sqrt{1 + ab\frac{z}{L}} + be^{-d\frac{z}{L}} \left(1 - d\frac{z}{L} + c \right) \right] \right\}$$

or the unstable case, $-2 \leq \frac{z}{L} \leq 0$

$$\phi_m = \sqrt[3]{\frac{1 + 0.625 \left(\frac{z}{L}\right)^2}{1 - 7.5 \frac{z}{L}}}$$

$$\phi_h = 0.64 \sqrt[3]{\frac{3 - 2.5 \frac{z}{L}}{1 - 10 \frac{z}{L} + 50 \left(\frac{z}{L}\right)^2}}$$

In the stable case $Pr_n = 0.923$ is the turbulent Prandtl number during neutral conditions, $a = 1$, $b = 2/3$, $c = 5$, $d = 0.35$.

Equations

Subgrid turbulent velocities come from a stochastic model, and the equation of motion for a single particle takes the form of a stochastic ordinary differential equation. The discrete form of such equations is:

$$\begin{aligned} X(t + \Delta t) &= X_{Adv}(t + \Delta t) + U'(t + \Delta t)\Delta t G_X \\ Y(t + \Delta t) &= Y_{Adv}(t + \Delta t) + V'(t + \Delta t)\Delta t G_Y \\ Z(t + \Delta t) &= Z_{Adv}(t + \Delta t) + W'(t + \Delta t)\Delta t (Z_{top})^{-1} + V_G \Delta t \end{aligned}$$

where $\mathbf{P}(X, Y, Z)$ is particle position, the pedices *Adv* indicates new positions computed by advection of the resolved wind speed, U', V', W' are the turbulent velocity components and $G_X, G_Y, (Z_{top})^{-1}$ are scaling factors related to the adopted coordinates. As horizontal coordinates the same system of the meteorological dataset is kept, but fields are interpolated on an internal sigma terrain following vertical system, i.e. whose coordinate lines follow the orography of the terrain.

Advection

Given the position $\mathbf{P}(t)$ of a particle at some time t the model first computes the advective contribution to the new position $\mathbf{P}'(t + \Delta t)$ at time $t + \Delta t$. It uses a two step technique with a first guess position:

$$\mathbf{P}'(t + \Delta t) = \mathbf{P}(t) + \mathbf{V}(\mathbf{P}, t)\Delta t,$$

where $\mathbf{V}(\mathbf{P}, t)$ is the resolved wind velocity at time t interpolated at the particle position and then giving a final position:

$$\mathbf{P}(t + \Delta t) = \mathbf{P}(t) + \frac{1}{2} [\mathbf{V}(\mathbf{P}, t) + \mathbf{V}(\mathbf{P}', t + \Delta t)] \Delta t.$$

Trajectories are terminated if they exit the upper boundary, whereas their integration formally continues after a particle hits the ground.

Dispersion

The second step in computing tracer particle motion consists in adding a further displacement due to turbulent velocities given by stochastic processes. For each component such process is described by the following equations

$$U'(t + \Delta t) = R(\Delta t)U'(t) + U''\sqrt{1 - R(\Delta t)^2}$$

$$V'(t + \Delta t) = R(\Delta t)V'(t) + V''\sqrt{1 - R(\Delta t)^2}$$

$$\begin{aligned} \left(\frac{W'}{\sigma_W}\right)(t + \Delta t) &= R(\Delta t)\left(\frac{W'}{\sigma_W}\right)(t) + \left(\frac{W''}{\sigma_W}\right)(t)\sqrt{1 - R(\Delta t)^2} + \\ &+ T_{LW}(1 - R(\Delta t))\frac{\partial\sigma_3(t)}{\partial z} \end{aligned}$$

with

$$\sigma_W(t + \Delta t) = \sigma_W(t) + W'(t)\Delta t\frac{\partial\sigma_3(t)}{\partial z}$$

and where the autocorrelation function R is

$$R(\Delta t) = e^{-\frac{\Delta t}{T_{L_i}}}$$

with $T_{L_i} = T_{LW}$, T_{LU} or T_{LV} Lagrangian time scales, assumed as constant in the model and equal to $T_{LW} = 100s$ and $T_{LU} = T_{LV} = 10800s$. The random velocities U'' , V'' , W'' are computed as

$$U'' = \sigma_1\lambda_1, \quad V'' = \sigma_2\lambda_2, \quad W'' = \sigma_3\lambda_3,$$

where the σ_i^2 are the turbulent velocity variances and λ_i are realizations of gaussian random processes with mean 0 and unitary standard deviation.

Determination of $U'' V'' W''$: the model has different possibilities for computes σ_i values too. Turbulent velocity variances are computed directly either from stability functions, friction velocity u^* , convective velocity scale W^* and boundary layer depth Z_i . Semiempirical formulas for the eddy diffusivity vary from stable to unstable conditions and also for different locations in the ABL. A first possibility is given by the following expressions for the stable or neutral cases:

- for the surface layer:

$$\begin{aligned} \sigma_3^2 &= 3.0(u^*)^2, \\ \sigma_1^2 &= 4.0(u^*)^2, \\ \sigma_2^2 &= 4.5(u^*)^2, \end{aligned}$$

- for the rest of boundary layer:

$$\begin{aligned}\sigma_3^2 &= 3.0(u^*)^2 \left(1 - \frac{z}{Z_i}\right)^{\frac{3}{2}}, \\ \sigma_1^2 &= 4.0(u^*)^2 \left(1 - \frac{z}{Z_i}\right)^{\frac{3}{2}}, \\ \sigma_2^2 &= 4.5(u^*)^2 \left(1 - \frac{z}{Z_i}\right)^{\frac{3}{2}};\end{aligned}$$

while unstable conditions are modeled as follow:

- for surface layer:

$$\begin{aligned}\sigma_3^2 &= 1.74(u^*)^2 \left(1 - 3\frac{z}{L}\right)^{\frac{2}{3}}, \\ \sigma_1^2 &= \sigma_2^2 = 0.36W^*,\end{aligned}$$

- and in the rest of the ABL:

$$\begin{aligned}\sigma_3^2 &= 3.0(W^*)^2 \left(\frac{z}{Z_i}\right)^{\frac{2}{3}} \left(1 - \frac{z}{Z_i}\right)^{\frac{2}{3}} \left(1 + 0.5R^{\frac{2}{3}}\right), \\ \sigma_1^2 &= \sigma_2^2 = 0.36W^*,\end{aligned}$$

where $R = 0.2$ is the ratio between the heat flux at the inversion point to the flux at the surface.

In order to determine turbulent motions for the dispersed particles inside the ABL, an alternative choice is to evaluate the diffusion coefficients and convert them into turbulent velocities. Particularly the vertical diffusion coefficient K_3 is given by the following expressions:

$$K_3 = kw_h z \left(1 - \frac{z}{Z_i}\right)^2,$$

where

- $w_h = u^* \phi_h^{-1}$ within the surface layer ($\frac{z}{Z_i} \leq 0.1$);
- $w_h = w_m Pr^{-1}$ in the rest of the ABL ($0.1 < \frac{z}{Z_i} < 1$).

The Prandtl number, with ϕ_h and ϕ_m evaluated at $\frac{z}{Z_i} = 0.1$, is given by $Pr = \frac{\phi_h}{\phi_m} + 7.2k\left(\frac{z}{Z_i}\right)\left(\frac{W^*}{w_m}\right)$, where $w_m = [(u^*)^3 + 0.6(W^*)^3]^{\frac{1}{3}}$ and $W^* = 0$ for neutral and stable conditions. Therefore the turbulent velocity variance can be computed by the formula:

$$\sigma_3 = \sqrt{\frac{K_3}{T_{LW}}}.$$

Analogous semiempirical descriptions are used also for the open atmosphere, above the ABL. Note that, in this part of the atmosphere the contribution of the unresolved turbulence is subdominant due to the strong large scale circulation.

Deposition

Deposition of spores to the ground is simply computed assuming that the particle deposition flux $j(\mathbf{x}, t)$ is proportional to particle concentration at ground level θ :

$$j(\mathbf{x}, t) = V_d \theta(\mathbf{x}, t)|_{z=0}$$

where the parameter V_d has the dimension of a velocity and has been taken equal to the gravitational settling velocity. This identification is the simplest choice, more sophisticated description is possible, taking into account the specific effect of the type of canopy, e.g. forests, crops, lakes, cities or other possible soil uses. Assuming that deposition occurs in a layer of thickness ΔZ_d above the ground level and taking particle concentration as constant within this layer, the time employed by the mass present in ΔZ_d to be completely deposited is equal to $\frac{\Delta Z_d}{V_d}$ and hence the fraction of mass deposited in a time step Δt is given by the ratio $\frac{V_d \Delta t}{\Delta Z_d}$. This mass removal is reproduced in the simulations with the following probabilistic technique:

- throughout each time step the probability for a spore to be deposited is identified with the ratio

$$P = \frac{V_d \Delta t}{\Delta Z_d}$$

- therefore at the end of a step a random number λ in the interval between 0 and 1 is extracted for each particle below ΔZ_d which will be deposited if $\lambda < P$.

3.3.3 Statistical observables

Simulations give considerable information about the dispersal process. The natural output of the adopted model are particle trajectories by which eulerian concentrations can be rebuilt on suitable grids simply collecting particles whose positions stay inside each defined cell of the grid. In this work I focus on the statistics of the flight time, i.e. the time between spore take off and landing. The former can be useful for studying the spatial extent of fungal dissemination, the latter are the subject of the present work that deals with the implications of spores release time on the effectiveness of the dissemination. Additional observables like the deposition distance, are important to understand the reach of fungal dispersal. Here I focus on flight time to understand the constraints on survival imposed by the physics of dispersal in the atmosphere. Spores sediment after a timescale that can vary considerably from one trajectory to another, even when their initial condition is identical. Hence each release is associated with a probability distribution of flight times from which a probability density function (PDF) and a cumulative probability function (CPDF) can be computed. Consequently several statistical quantities can be considered, for example the moments of the PDF. In this work I consider the *mean flight time*:

$$\tau = \frac{1}{N} \sum_{i=1}^N \tau_i$$

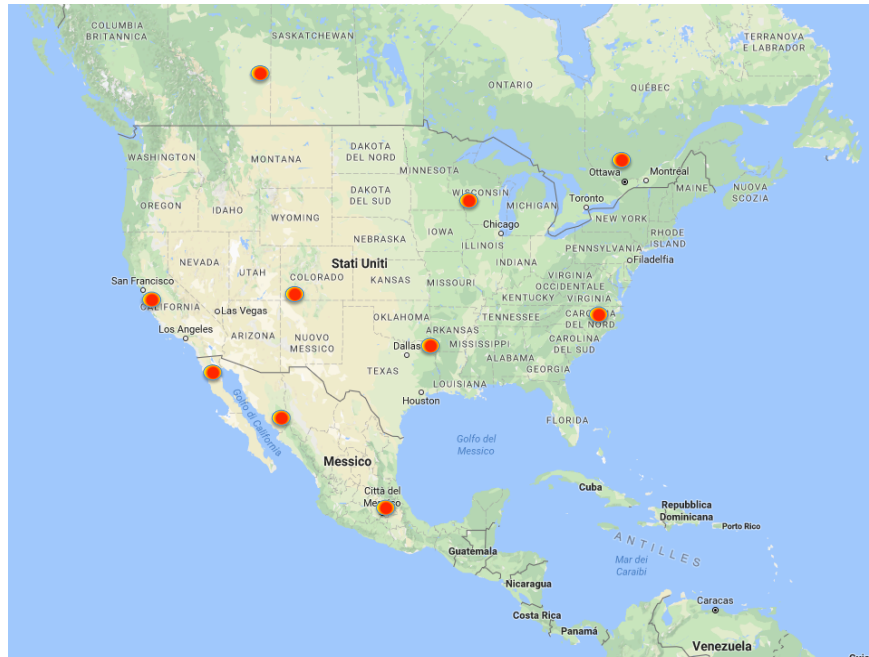


Figure 3.2 – Geographical distribution of spores release location in North America: ten different starting locations have been chosen for spores release and are showed on the map as red circles.

Alternatively it can be used as statistical observable the time after which a given fraction of the spores has sedimented.

3.4 Results

Preliminary simulations revealed substantially different scenarios. Flight times are much longer for spores released at certain hours of the day rather than others. Then I set out to understand the role of the initial condition on the statistics of flight time. I chose 10 different starting locations distributed across the whole North American continent (figure 3.2), and with widely different uses of the soil. All these locations are biologically relevant for several kinds of fungal species and because of the presence of different agricultural activities (table 3.2). For each location the dispersal has been computed releasing spores every 3 hours during the months of January, April, July and October of year 2014 (as representative of the four seasons), for a total amount of 9680 simulations. In the following I will refer to a *release* as a dispersal process starting at a fixed time from a specific location.

As suggested by preliminary results, most releases showed a common feature: the presence of a diurnal cycle in the mean flight time signal i.e. the presence of oscillations with a period of 24 hours in the behavior of this statistics. Plots of these signals for three selected locations, situated at very different latitudes, are shown in figures from 3.3 to 3.8. Signal for Green Mexico, that belongs to

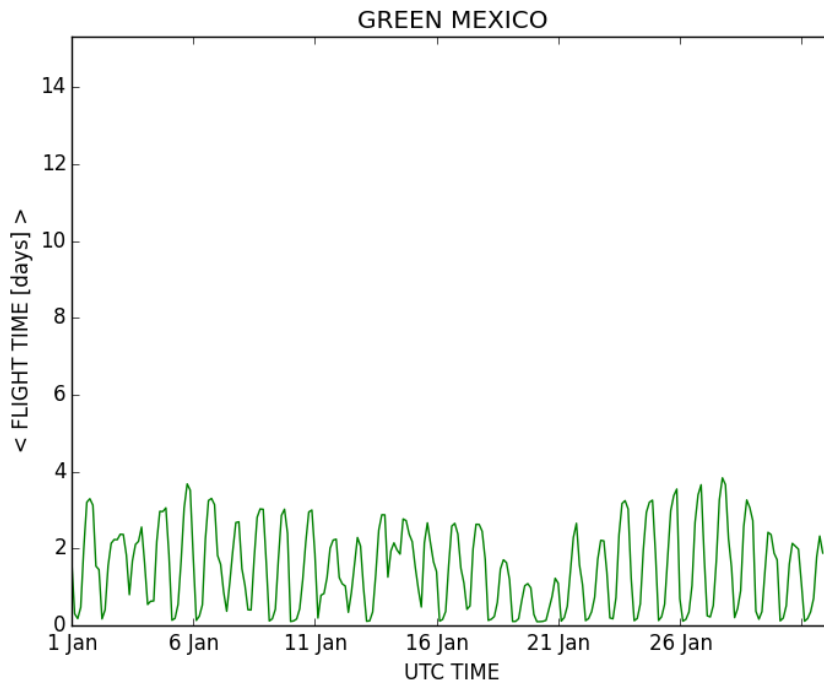
Table 3.2 – Starting locations for simulations

Location	latitude	longitude	description	label
Int. maize and wheat improvement center (Mexico)	19.6	−99.2	green revolution	GREEN MEXICO
Yaqui and Mayo valleys (Mexico)	27.7	−109.0	major wheat production area in Mexico	WHEAT MEXICO
Baja (Mexico)	31.4	−115.7	coastal, California peninsula	BAJA CA
Oklahoma	33.5	−94.6	crops in great plains of US	CROPS OKLA
Wilson County, North Carolina	35.9	−78.1	tobacco production	TOBACCO NC
Watsonville, California	36.9	−121.5	major agricultural area	CROPS CA
San Juan national forest	37.5	−107.9	forest on Rockies	FOREST COLORADO
Wisconsin	44.1	−90.9	vegetables growing area	VEGGIES WI
La Verendyre (Canada)	46.8	−76.1	reserve aunique	WILD CANADA
Alberta (Canada)	52.2	−111.1	forests and wheat	WHEAT ALBERTA

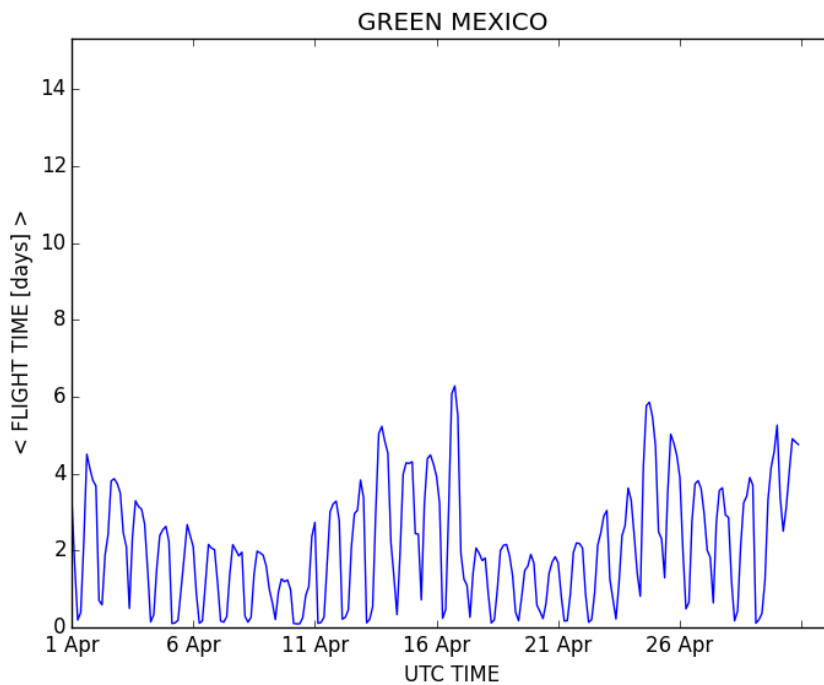
the tropical area, shows a very regular cycle in all seasons with very strong extreme events during summer; at Veggies Wi, a location in continental US, the diurnal cycle is less defined and the seasonal effect seems to be more important; a further scenario comes up at higher latitudes in Wheat Alberta where during winter the cycle is almost completely absent. To sustain this qualitative considerations I performed a more quantitative analysis of the results, based on different indicators. Two aspects are relevant and pointed out by simulations:

1. strength of the cycle (measured by the amplitude of the oscillations);
2. reproducibility of the cycle (quantified by how the period of oscillations is to 24 h).

As previously pointed out, these features significantly depend on seasons and locations of spores discharge. To give a quantitative measure of cycle's characteristics the deposition data have been analyzed computing ensemble averages and standard deviations of mean flight times related to discharges performed at the same hour of the day. The results are shown in figures 3.9 to 3.18, in which

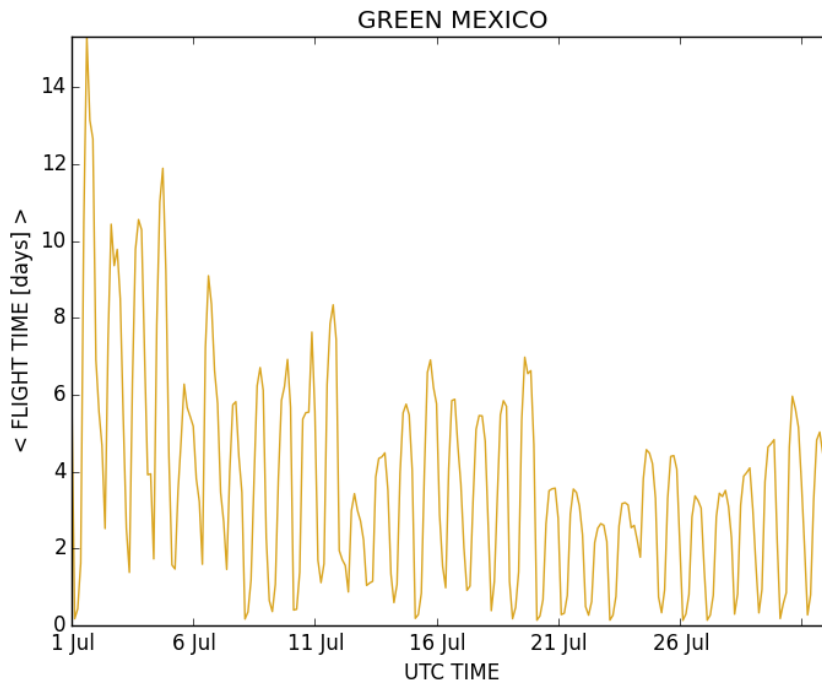


(a) Location: Green Mexico; Month: January.

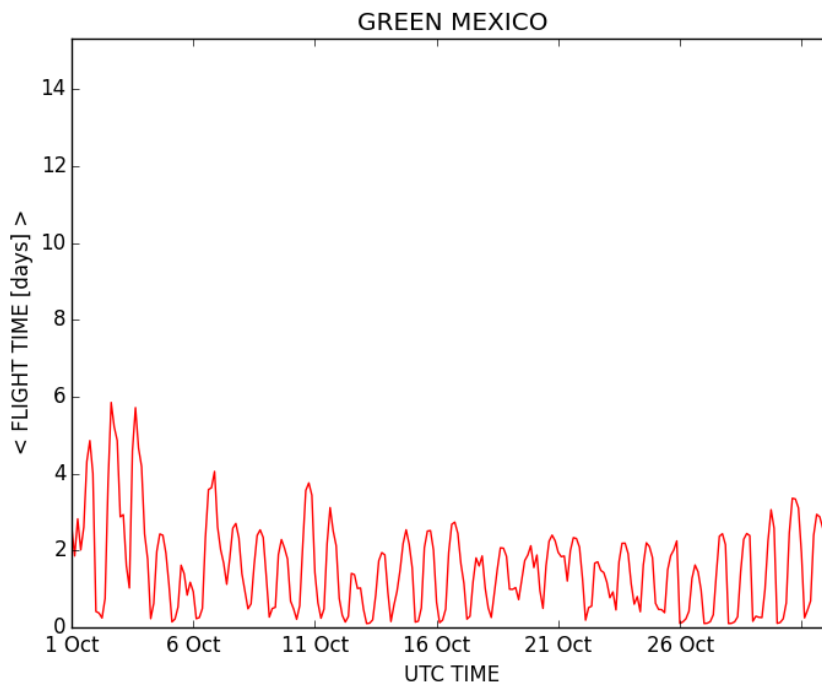


(b) Location: Green Mexico; Month: April.

Figure 3.3 – Mean flight time signal for releases started at Green Mexico during January and April of year 2014.

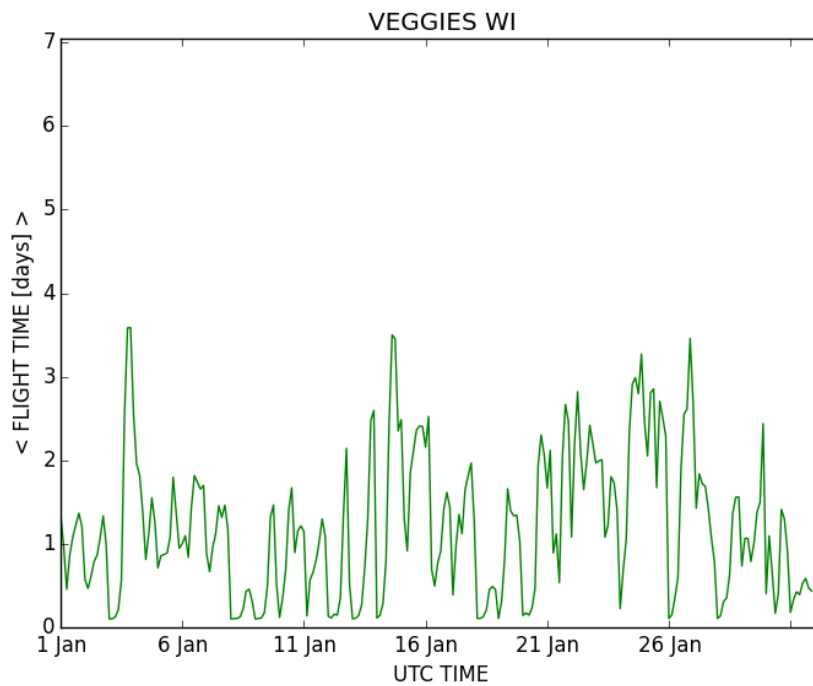


(a) Location: Green Mexico; Month: July.

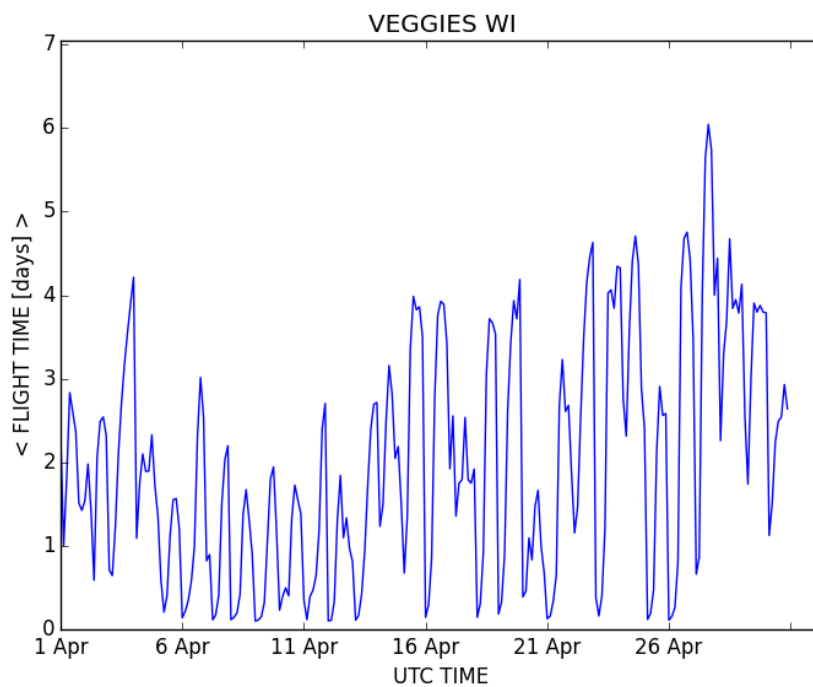


(b) Location: Green Mexico; Month: October.

Figure 3.4 – Mean flight time signal for releases started at Green Mexico during July and October of year 2014.

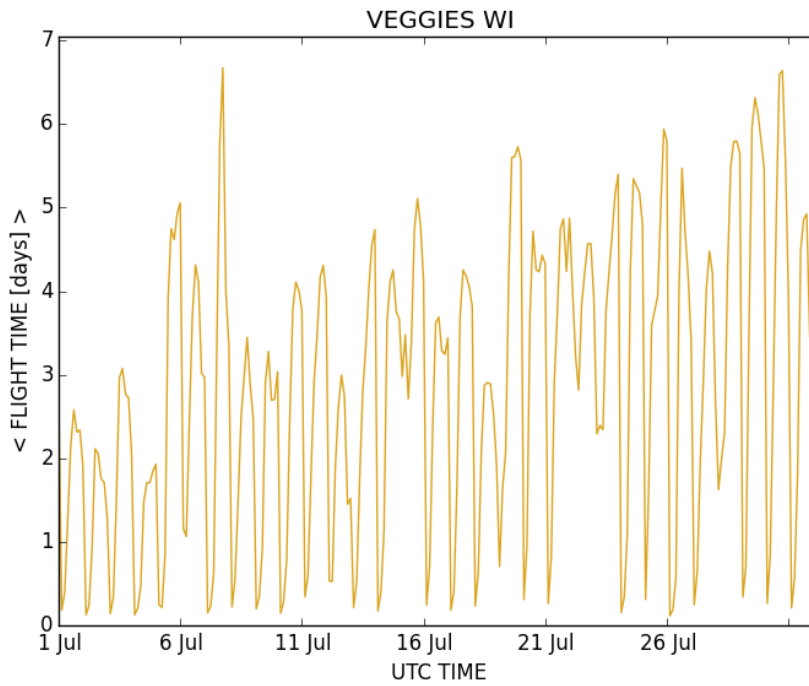


(a) Location: Veggies WI; Month: January.

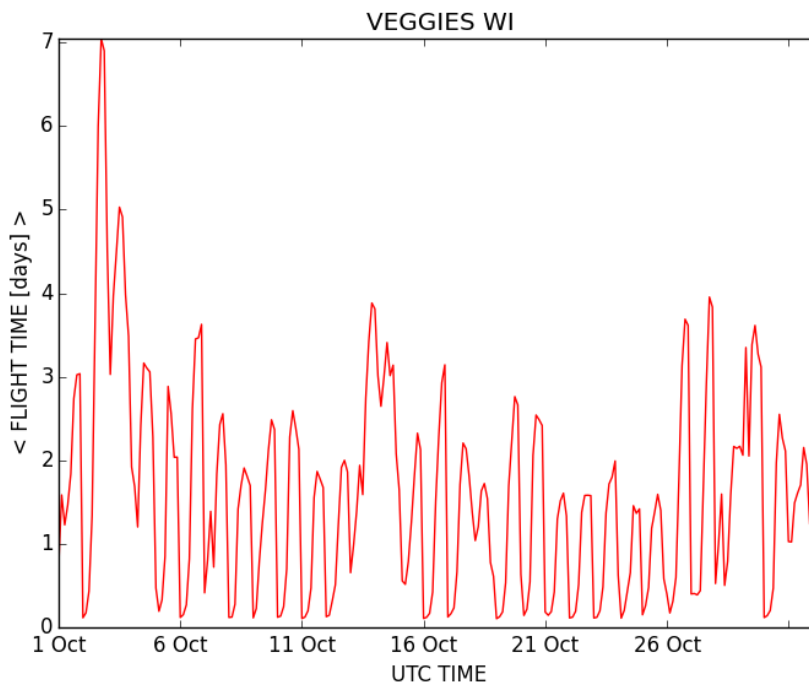


(b) Location: Veggies WI; Month: April.

Figure 3.5 – Mean flight time signal for releases started at Veggies WI during January and April of year 2014.

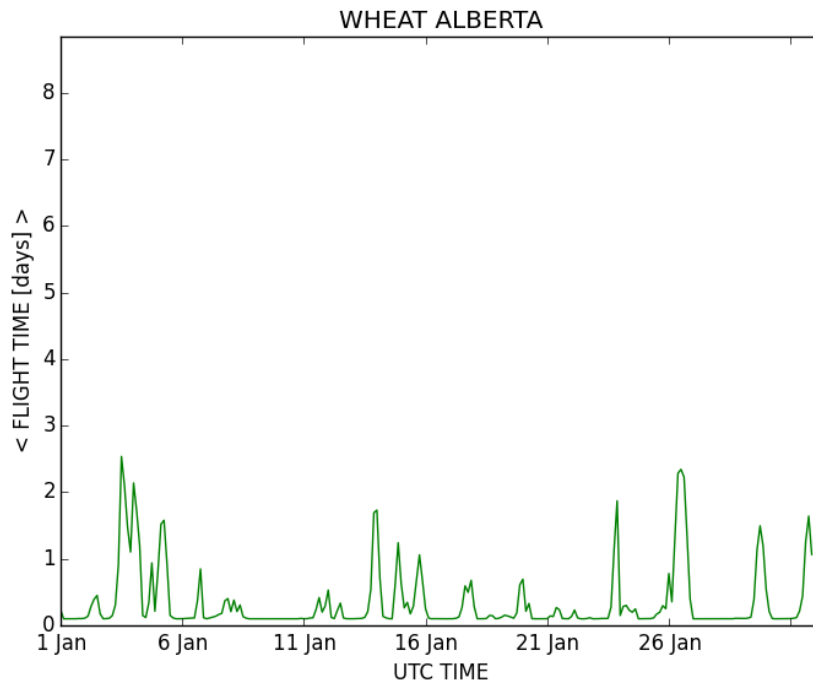


(a) Location: Veggies WI; Month: July.

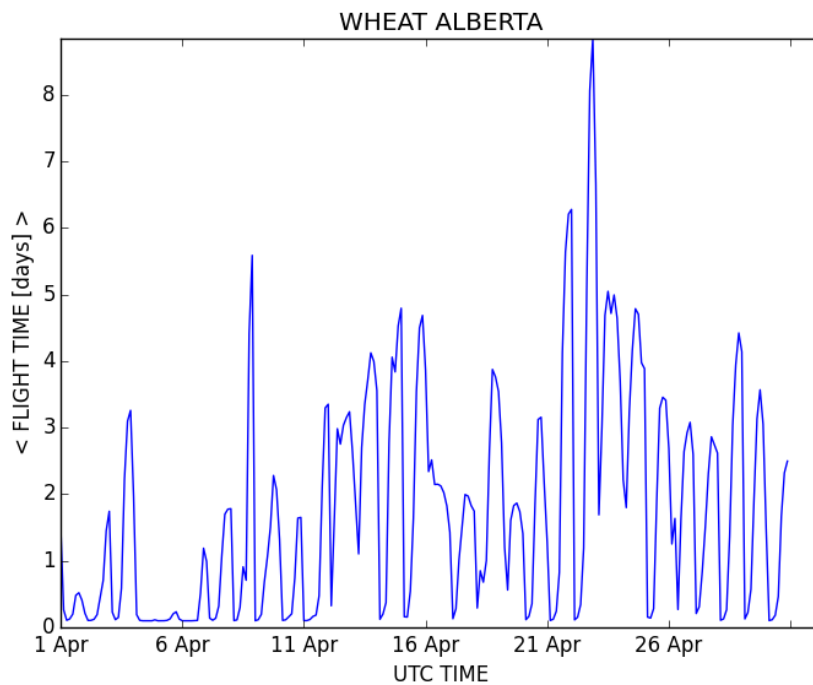


(b) Location: Veggies WI; Month: October.

Figure 3.6 – Mean flight time signal for releases started at Veggies Wi during July and October of year 2014.

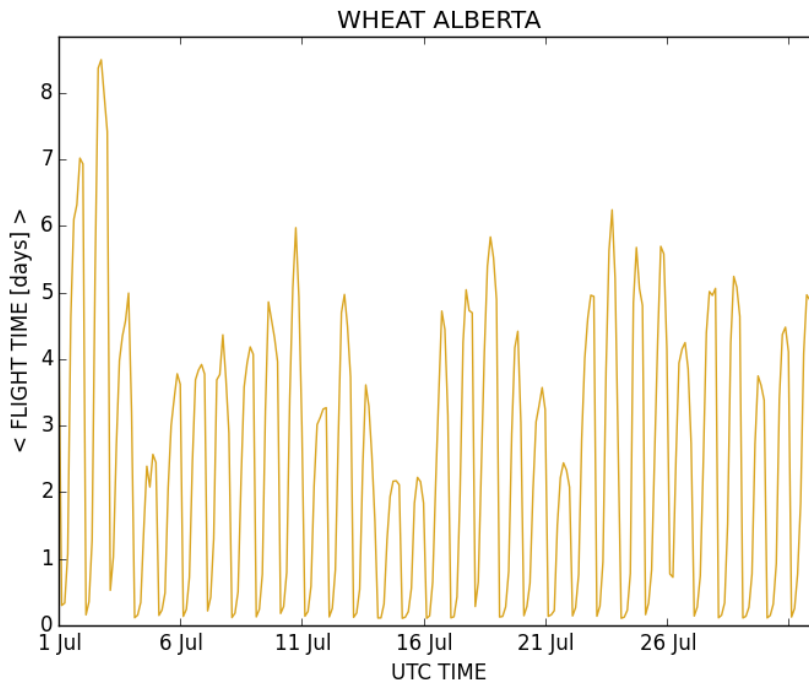


(a) Location: Wheat Alberta; Month: January.

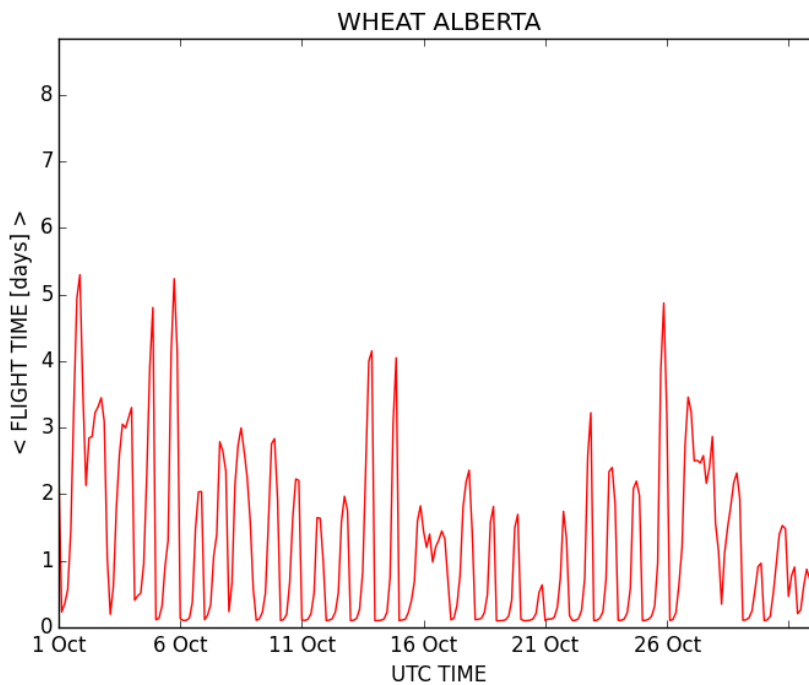


(b) Location: Wheat Alberta; Month: April.

Figure 3.7 – Mean flight time signal for releases started at Wheat Alberta during January and April of year 2014



(a) Location: Wheat Alberta; Month: July.



(b) Location: Wheat Alberta; Month: October.

Figure 3.8 – Mean flight time signal for releases started at Wheat Alberta during July and October of year 2014

the typical day for the chosen location and period is depicted: the maximum of the averaged mean flight time quantifies the strength of the cycle and the standard deviation is related to the actual 24 hours periodicity of the signal. As a measure of this latter property the following ratio can be introduced:

$$\mathcal{I} = \frac{2\bar{\sigma}}{\max\langle\tau\rangle}$$

where τ are mean flight times and angular brackets denotes average on simulations started at the same hour. The computed values of the ratio are reported

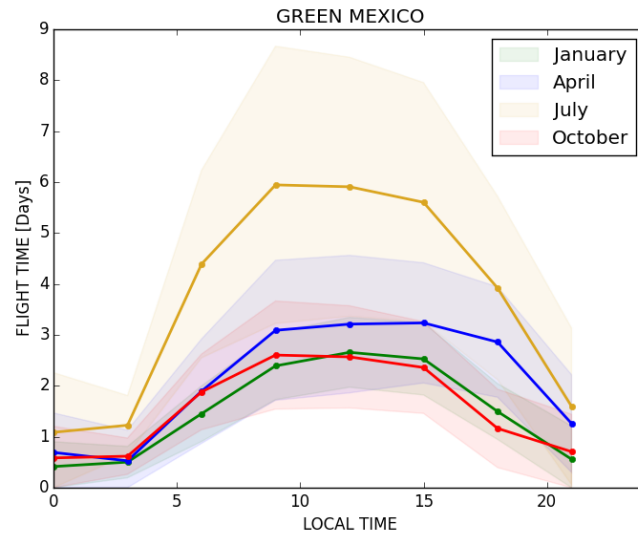
Table 3.3 – *Diurnal cycle strength and sharpness: for each starting location and each selected period, the maximum mean flight time averaged on releases performed at the same hour of the day and the index \mathcal{I} that measure the goodness of the cycle are shown.*

Location time [days]	January $\max\langle\tau\rangle, \mathcal{I}$	April $\max\langle\tau\rangle, \mathcal{I}$	July $\max\langle\tau\rangle, \mathcal{I}$	October $\max\langle\tau\rangle, \mathcal{I}$	Year $\max\langle\tau\rangle, \mathcal{I}$
Green Mexico	2.24, 0.51	2.71, 0.77	4.86, 0.75	2.02, 0.77	2.89, 1.03
Wheat Mexico	1.45, 0.46	3.19, 0.59	5.21, 0.58	3.07, 0.39	3.18, 0.99
Baha CA	1.52, 0.63	3.12, 0.82	4.33, 0.68	2.73, 0.55	2.85, 1.15
Crops Okla	1.43, 0.88	2.57, 0.69	3.74, 0.43	2.45, 0.65	2.46, 0.87
Tobacco NC	1.03, 1.27	2.13, 0.97	3.24, 0.56	2.38, 0.86	2.14, 1.04
Crops CA	1.12, 0.62	2.65, 0.67	4.85, 0.39	3.11, 0.50	2.93, 0.79
Forest CO	0.64, 2.56	1.97, 1.36	3.80, 0.89	1.99, 1.00	2.03, 1.59
Veggies WI	0.96, 1.58	2.09, 1.09	3.65, 0.58	1.95, 1.01	2.16, 1.14
Wild Canada	0.69, 2.14	1.79, 0.95	2.63, 0.85	1.74, 0.90	1.66, 1.18
Wheat Alberta	0.20, 4.76	2.53, 1.05	4.30, 0.43	2.11, 0.87	2.24, 1.18

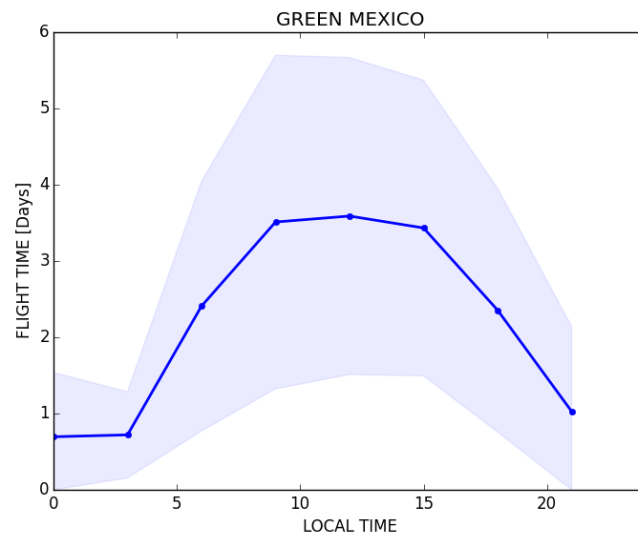
in table 3.3, together with maximum values of average mean flight time; values close to or greater than 1 indicate that the diurnal signal is buried in the standard deviation band and hence the cycle is not well defined. Looking at the values of \mathcal{I} we notice that for tropical and subtropical locations the cycle is clearly present independently from seasons while in other places it is almost always present during summer than other periods of the year. Moreover the trend is that highest flight times result from lowest latitudes (with the exception of Wheat Alberta). This is very important because tropical and subtropical areas are regions where many fungal species find favourable conditions to survive during winter (overwintering region), waiting for spring and summer to expand their presence spreading northward.

3.4.1 Role of the ABL dynamics

Having observed and quantified the presence of a diurnal cycle in the statistics of spores deposition, the natural questions to answer are on the reasons at the origin of the cycle dynamics and on the dynamical driving mechanism. By analyzing probability density functions (PDF) and associated cumulative distributions



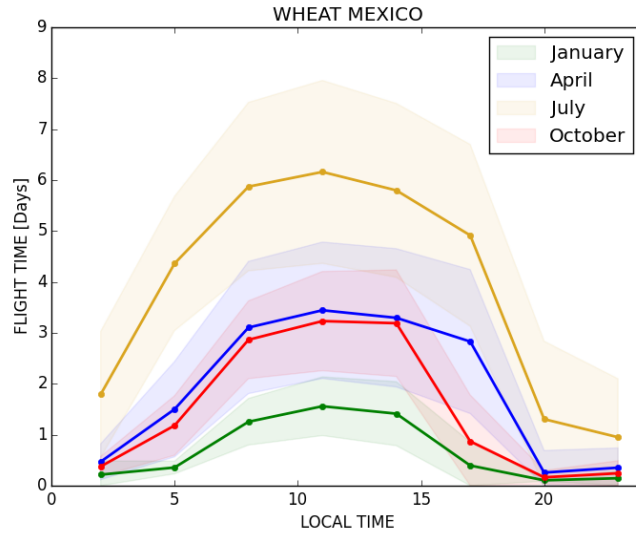
(a)



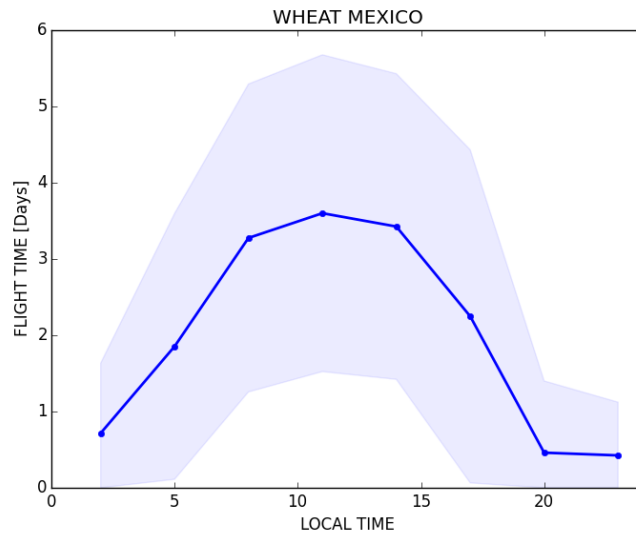
(b)

Figure 3.9 – Dots represent the mean flight time averaged on all releases performed in Green Mexico at the same hour but different days of the selected period; width of the shaded band is the related standard deviation. Figure a) shows the result of the averaging procedure for January, April, July and October separately; in figure b) all months are considered together.

(CPDF) of flight times for spores released at the same hour, two qualitatively and substantially different dynamics appear. In way of example, in figures 3.19 and 3.20, the distributions of flight times, averaged on all releases at same hour, are shown for the location Baja CA and discharge at 2:00 AM (3.20) and 2:00 PM (fig 3.19). Because the PDFs are strictly related to the deposition flux of spores to the ground, the comparison of figures 3.19a and 3.20a indicates that:



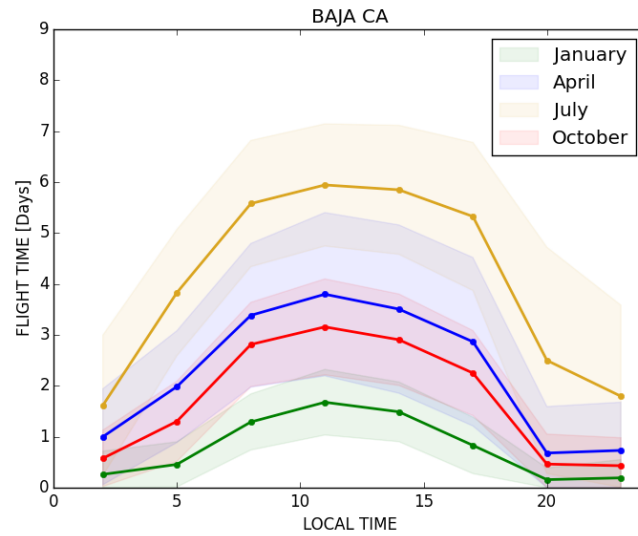
(a)



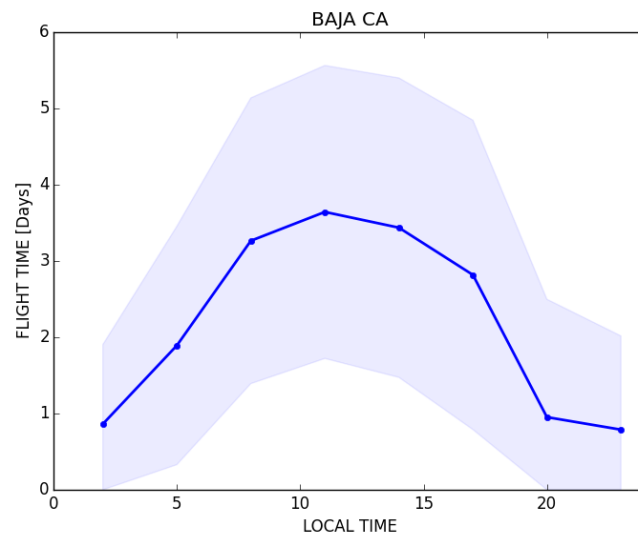
(b)

Figure 3.10 – Dots represent the mean flight time averaged on all releases performed in Wheat Mexico at the same hour but different days of the selected period; width of the shaded band is the related standard deviation. Figure a) shows the result of the averaging procedure for January, April, July and October separately; in figure b) all months are considered together.

- in the first case (release at 2:00 PM) the flux to ground is lower than in the second case (release at 2:00 AM);
- for releases at 2:00 PM deposition is strongly reduced after the early stage of the dispersal process. In the other cases the flux to ground decays more slowly;



(a)

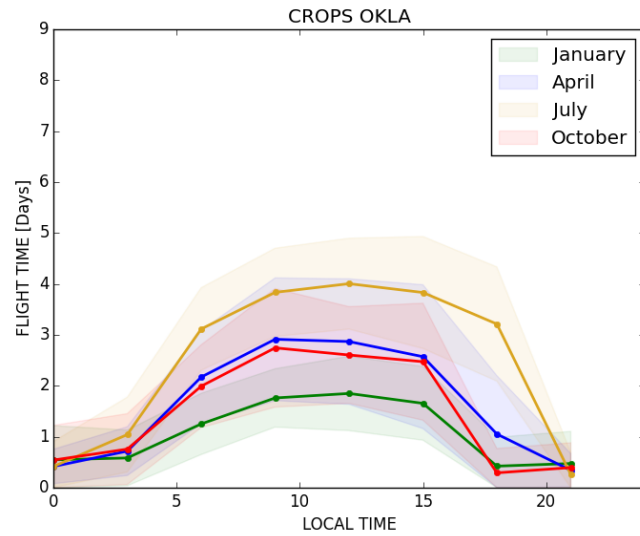


(b)

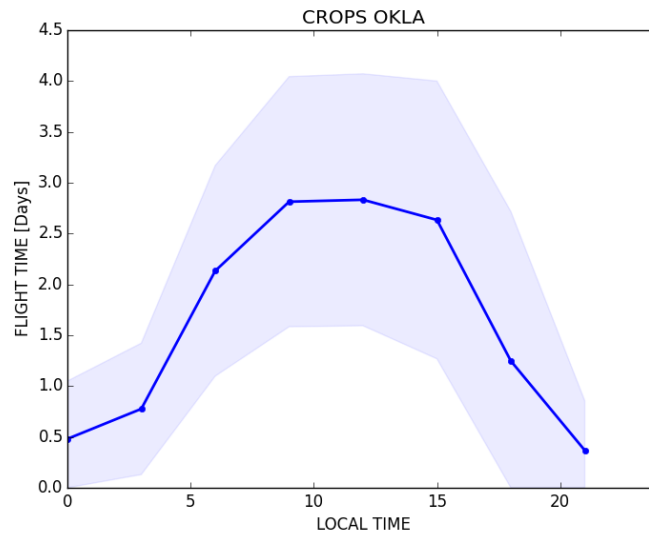
Figure 3.11 – Dots represent the mean flight time averaged on all releases performed in Baja Ca at the same hour but different days of the selected period; width of the shaded band is the related standard deviation. Figure a) shows the result of the averaging procedure for January, April, July and October separately; in figure b) all months are considered together.

- as a consequence of the previous points particles, fly much longer in the first case and the deposition process continues for days and shows peaks with a characteristic distances of about 1 day, reflecting the diurnal cycle.

A key point is that the early stage of the dispersal process is crucial in determining the mean flight time of spores because significantly different fractions



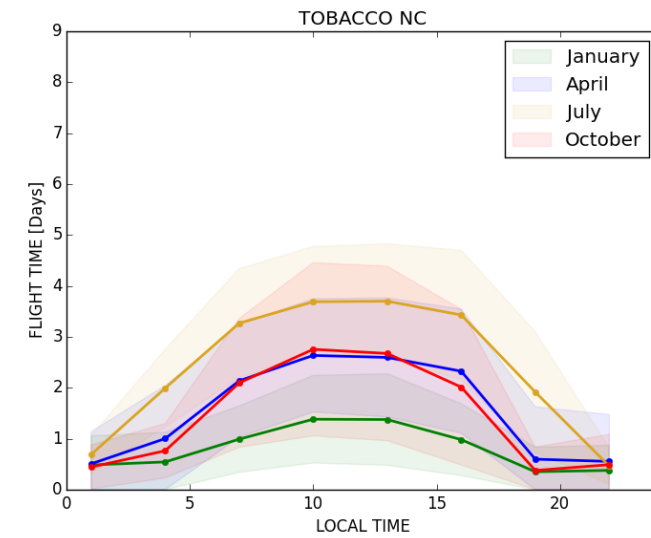
(a)



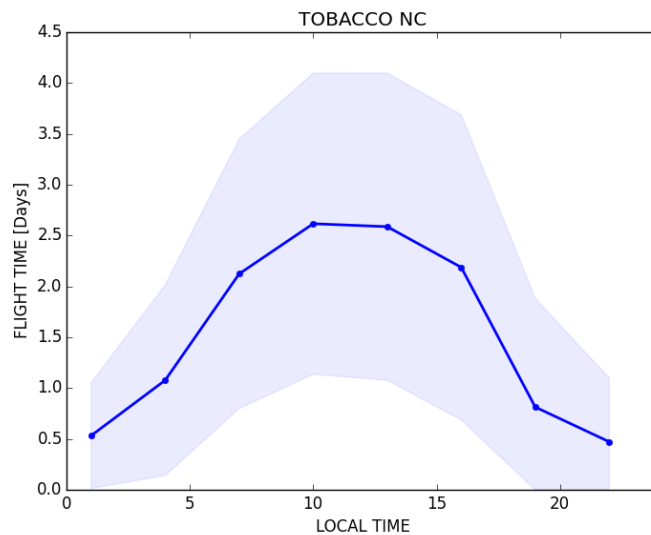
(b)

Figure 3.12 – Dots represent the mean flight time averaged on all releases performed in Crops Okla at the same hour but different days of the selected period; width of the shaded band is the related standard deviation. Figure a) shows the result of the averaging procedure for January, April, July and October separately; in figure b) all months are considered together.

of the spores puff are deposited to the ground starting at different hours. For examples releasing at 2:00 AM involve an average time of half a day to deposit the 70% of the spores while at 2:00 PM requires an average time of about 2 weeks, with all the possible implication on survival strategies of different species producing spores with significantly different survival skills. Understanding why this difference of order of magnitude appears needs to analyze what happens at



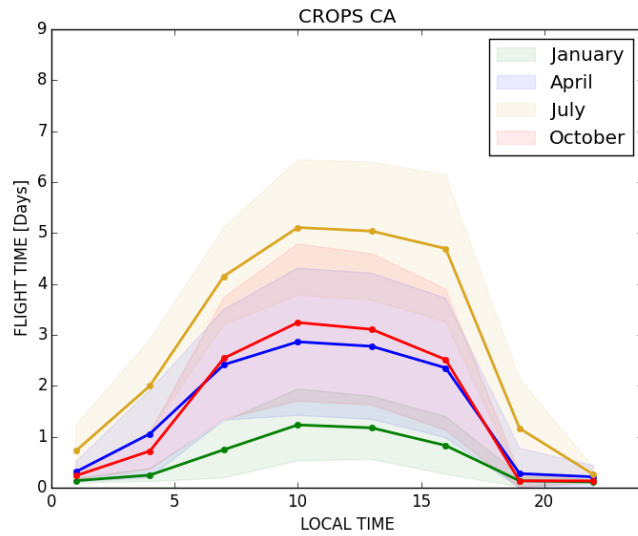
(a)



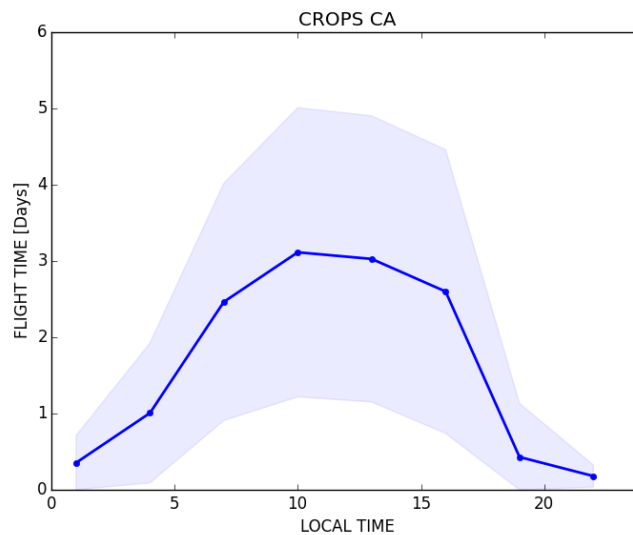
(b)

Figure 3.13 – Dots represent the mean flight time averaged on all releases performed in Tobacco NC at the same hour but different days of the selected period; width of the shaded band is the related standard deviation. Figure a) shows the result of the averaging procedure for January, April, July and October separately; in figure b) all months are considered together.

spore puffs after the release. The initial condition is the same for all releases, with all spores concentrated at the same height above and close to the ground. Looking at the vertical dispersion two clearly different behaviors occur. As one can see in figure 3.21, in some cases after few minutes the puff expands itself for hundreds of meters in the vertical; in other cases it stays vertically bounded with all spores close to the ground for hours. The first dynamics is typical of



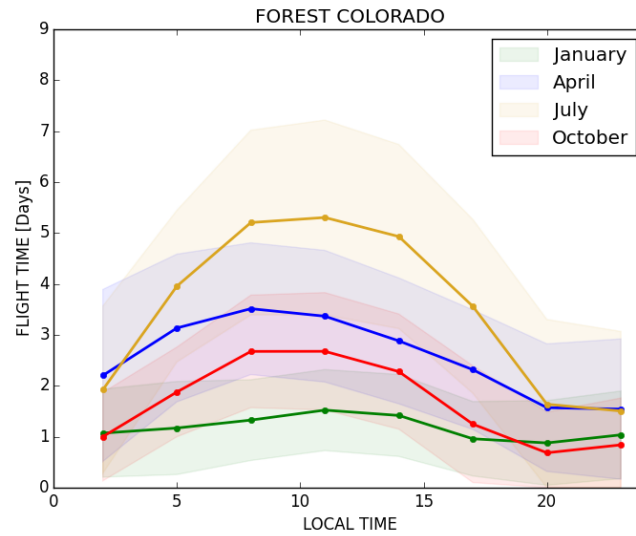
(a)



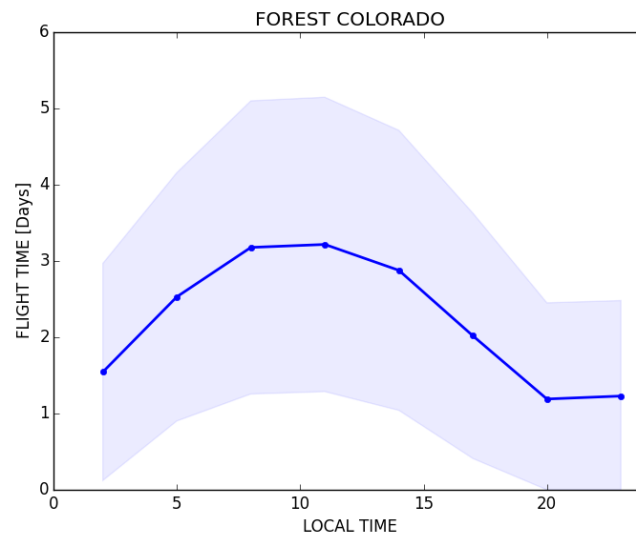
(b)

Figure 3.14 – Dots represent the mean flight time averaged on all releases performed in Crops Ca at the same hour but different days of the selected period; width of the shaded band is the related standard deviation. Figure a) shows the result of the averaging procedure for January, April, July and October separately; in figure b) all months are considered together.

sunlight hours while the second of night time releases. The previous analysis on diurnal cycle and a systematic look at PDFs and cumulative distributions reveal that also maxima in time of flight correspond to discharge of spores during sunny hours and minima corresponds to night time releases. This fact gives the key to read the cycle, that is: flight times strongly depend on the dynamical state of the ABL, particularly the stability. Discharging during sunny hours, when



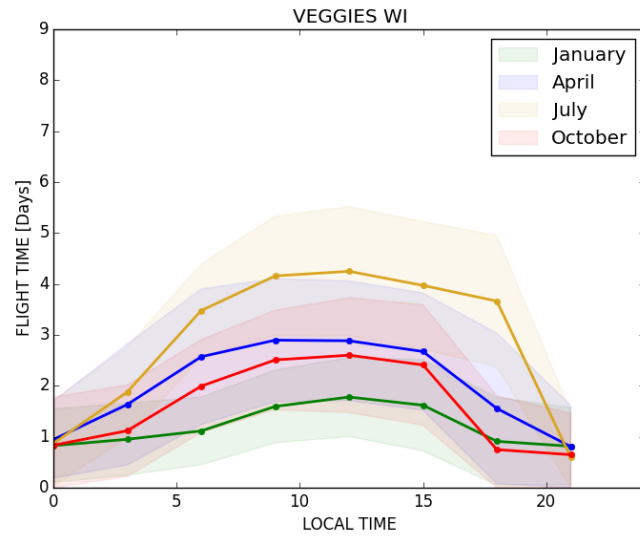
(a)



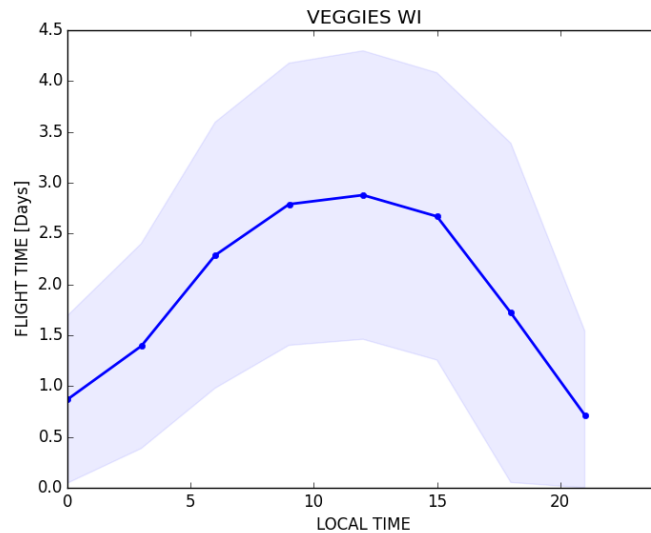
(b)

Figure 3.15 – Dots represent the mean flight time averaged on all releases performed in Forest Colorado at the same hour but different days of the selected period; width of the shaded band is the related standard deviation. Figure a) shows the result of the averaging procedure for January, April, July and October separately; in figure b) all months are considered together.

the ABL is unstable with strong vertical convective turbulence and when the thickness of the boundary layer easily reach the order of kilometers, allows the puff to extend from a few meters to hundreds in few minutes. This fact strongly reduces deposition and allows the spores to reach the large scale circulation (and consequently traveling horizontally for hundreds of kilometers). When sun is not heating the soil, the state of the ABL is typically stable and its thickness is lower



(a)

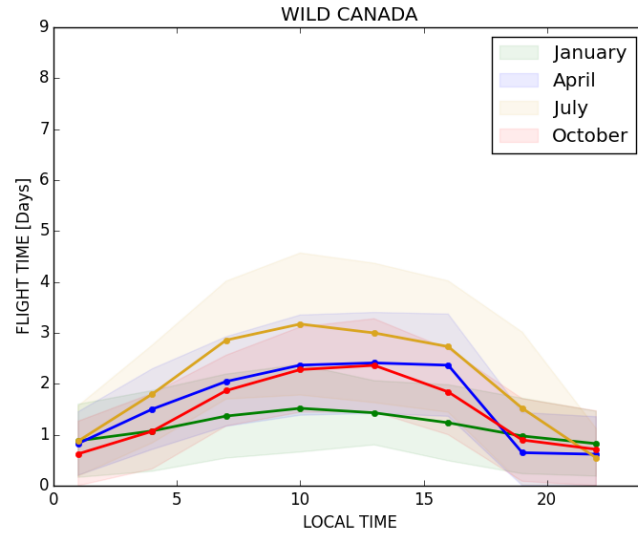


(b)

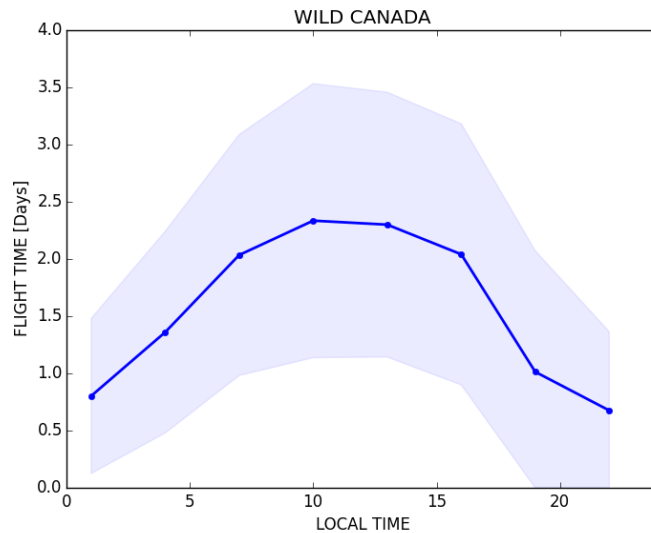
Figure 3.16 – Dots represent the mean flight time averaged on all releases performed in Veggies Wi at the same hour but different days of the selected period; the width of the shaded band is the related standard deviation. Figure a) shows the result of the averaging procedure for January, April, July and October separately; in figure b) all months are considered together.

than for unstable cases. Moreover the vertical diffusion is strongly suppressed keeping the puff concentrated close to ground for hours consequently supporting deposition of spores to the ground.

To reinforce such considerations I made a further analyses dealing with ABL parameters (whose information is again extrapolated from the NARR dataset). Such analysis is based on correlations between the mean flight time signal, a



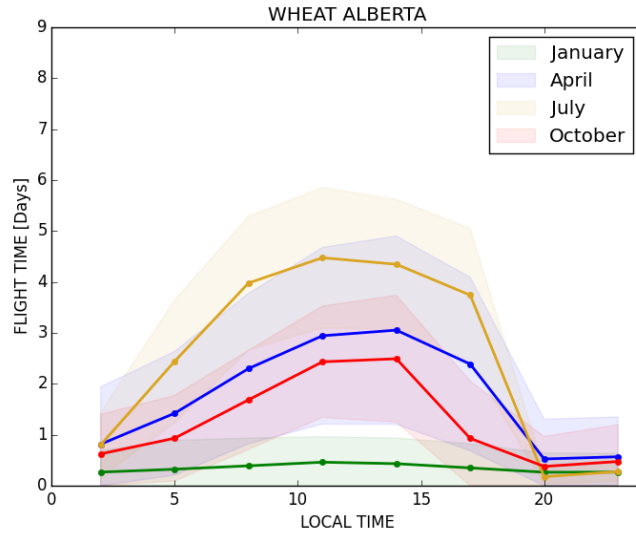
(a)



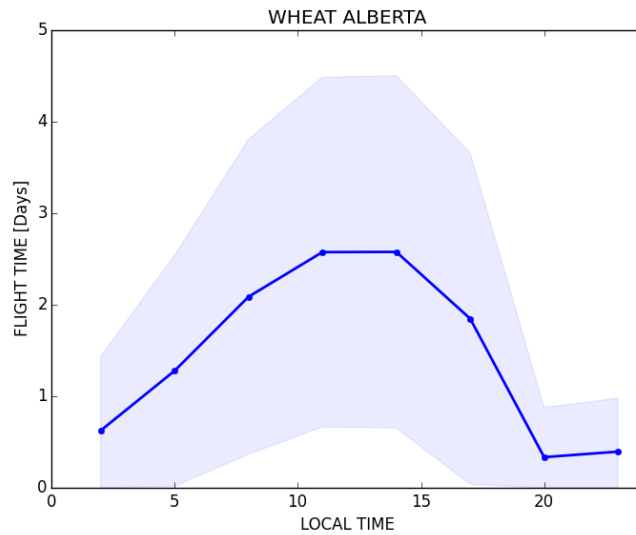
(b)

Figure 3.17 – Dots represent the mean flight time averaged on all releases performed in Wild Canada at the same hour but different days of the selected period; width of the shaded band is the related standard deviation. Figure a) shows the result of the averaging procedure for January, April, July and October separately; in figure b) all months are considered together.

24 hours periodic behaviour and the time series of four chosen ABL parameters, measured at the release location. The involved quantities are the friction velocity u^* , the convective velocity W^* , the Monin-Obhukov length L and the boundary layer thickness Z_i . Each parameter plays a different role in determining the dynamical state of the ABL and then, potentially, the feature of the spores



(a)



(b)

Figure 3.18 – Dots represent the mean flight time averaged on all releases performed in Wheat Alberta at the same hour but different days of the selected period; width of the shaded band is the related standard deviation. Figure a) shows the result of the averaging procedure for January, April, July and October separately; in figure b) all months are considered together.

dispersal. As measure of the correlation the Pearson coefficient

$$\rho_{X,Y} = \frac{\sum_{i=1}^n [(x_i - \bar{x})(y_i - \bar{y})]}{\sqrt{\sum_{i=1}^n (x_i - \bar{x})^2} \sqrt{\sum_{i=1}^n (y_i - \bar{y})^2}}$$

has been adopted. Here X is a variable, x_i is the value of X at time i and the overbar indicates the mean of X on its whole time signal. In the analysis X is

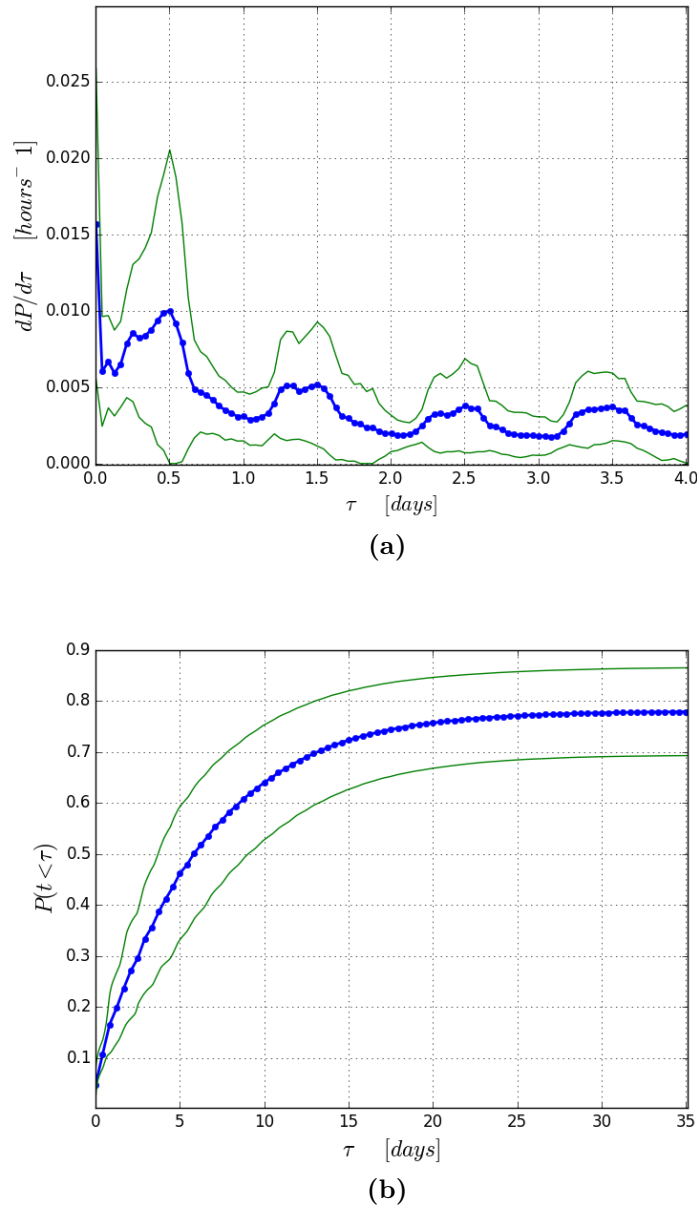
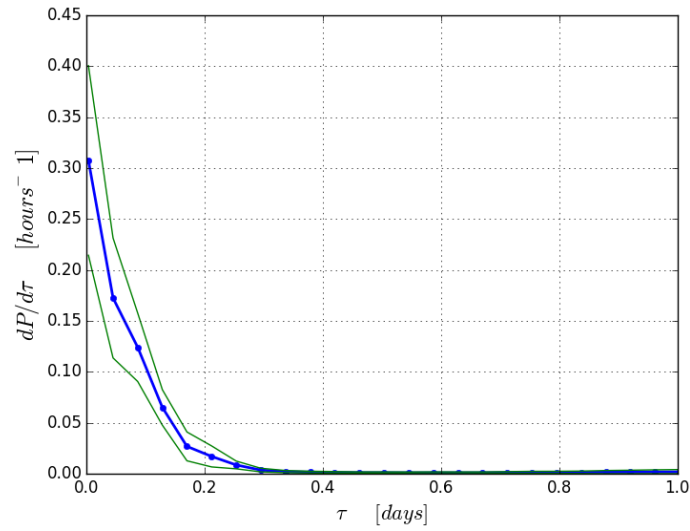
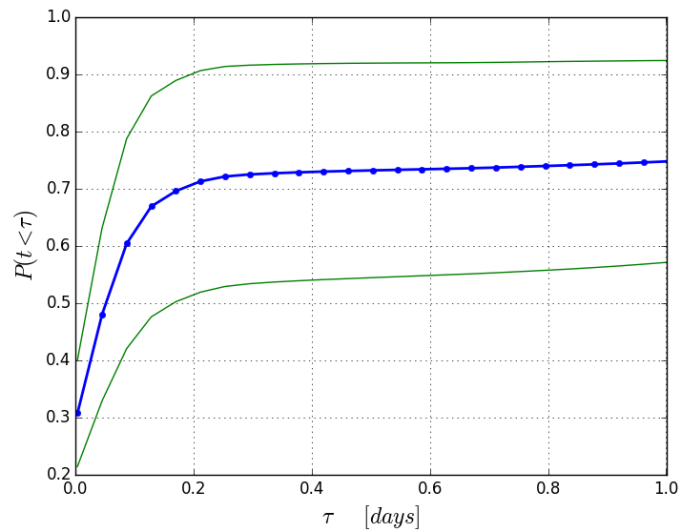


Figure 3.19 – Probability density function and cumulative distribution of flight times, averaged on all releases started at 2:00 PM (unstable case) of all days in July 2014. The blue line with squares is the averaged curve. The distance between green continuous lines and the blue line represents the standard deviation from the average.

τ and Y changes among u^* , W^* , L , Z_i and a 24 hours periodic signal H . This procedure shows that mean flight times correlate better with stability rather than hours of release, giving higher values for the correlation coefficient (see table 3.4). This fact clearly emerges where the diurnal cycle is particularly corrupted, while the ABL stability parameters persists to provide good correlation with the mean flight time signal. As an example one can look at Wild Canada in January (3.12).



(a)

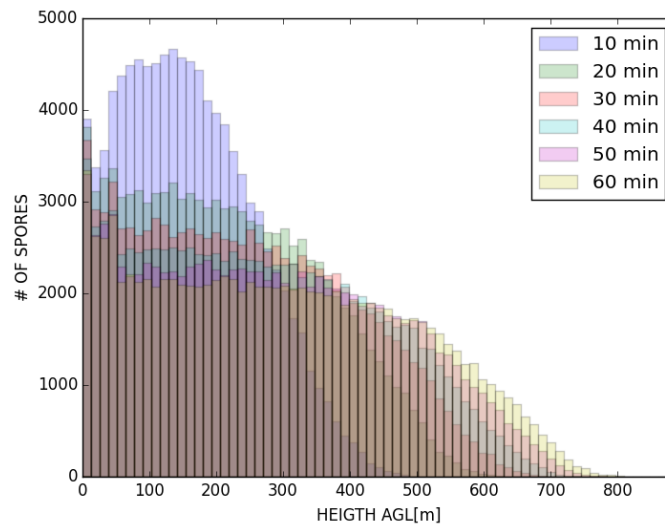


(b)

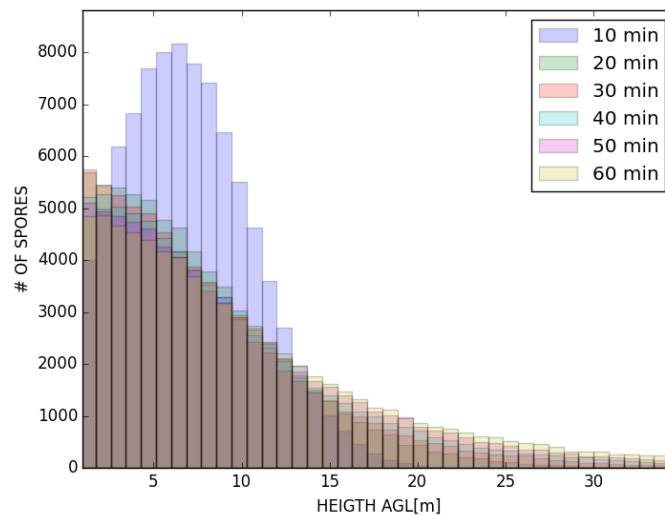
Figure 3.20 – Probability density function and cumulative distribution of flight times, averaged on all releases started at 2:00 AM (stable case) of all days in July 2014. The blue line with squares is the averaged curve. The distance between green continuous lines and the blue line represents the standard deviation from the average.

3.5 Conclusions

The motion of a spore after leaving its parent mycelium is very complex and spores escaped from the same fungus at the same time can land hundreds of kilometers far each other. Where and when spores will land and what environmental conditions will encounter, during and at the end of their atmospheric



(a)



(b)

Figure 3.21 – Histograms of particles height during the first hour after the release. a) unstable case; b) stable case.

travel, is unknown for fungi. Facing this high level of unpredictability brings the species of fungal kingdom to develop survival strategies based on huge proliferation to balance the spore wasting related with the uncertainty of the reproduction mechanism. Moreover biological studies show that some species has evolved their strategies in order to maximize the range of dissemination differently from others. Then the characteristic life of a spore during flight can vary from hours to weeks considering one species or another and why this differentiation started is an interesting evolutionary issue.

Table 3.4 – Pearson correlation coefficients for location Green Mexico: correlation between the mean flight time and other signals. H is a 24 hours periodic signal and other signals are time series of ABL parameters u^* , W^* , L and Z_i .

Green Mexico	$\rho_{\bar{\tau},H}$	$\rho_{\bar{\tau},U^*}$	$\rho_{\bar{\tau},W^*}$	$\rho_{\bar{\tau},L}$	$\rho_{\bar{\tau},Z_i}$
January	0.47	0.62	0.67	-0.80	0.40
April	0.31	0.55	0.68	-0.63	0.48
July	0.36	0.57	0.58	-0.61	0.16
October	0.41	0.52	0.62	-0.64	0.29
Year	0.31	0.48	0.50	-0.55	0.24

Table 3.5 – Pearson correlation coefficients for location Wheat Mexico.

Wheat Mexico	$\rho_{\bar{\tau},H}$	$\rho_{\bar{\tau},U^*}$	$\rho_{\bar{\tau},W^*}$	$\rho_{\bar{\tau},L}$	$\rho_{\bar{\tau},Z_i}$
January	0.53	0.66	0.67	-0.61	0.46
April	0.37	0.61	0.66	-0.60	0.47
July	0.36	0.65	0.65	-0.61	0.39
October	0.59	0.60	0.65	-0.70	0.52
Year	0.33	0.57	0.56	-0.59	0.40

However my research puts in light that flight times are driven mainly by stability of the ABL at time of release and that this feature often generates a well defined diurnal cycle whose amplitude can made the hour of the day to release spores a crucial choice to set up an effective survival strategy. As a first consequence, if a fungal species belongs to the class of LDDers, it has to discharge spores during unstable phases of the ABL, typically in sunny hours. Otherwise, if a fungus does not want to go far and its spores cannot resist too long to UV ray exposure, the best choice is to release spores on stable periods (typically night time) or it can use other mechanisms to reach the ground (the wet deposition is a relevant example). Indeed there is among mycologists the common believe that some species release before rainy periods. The work presented in this thesis doesn't deal with wet deposition, hence investigating the effect on flight times due to rain is a first interesting way to go deeper in the comprehension of the problem. On smaller scales new questions arise in light of this work: do fungi properly tune their releases according to a diurnal cycle, for instance following their internal circadian cycle? Or they developed biological devices that are able to measure quantities possibly related with stability, like soil temperature? Are they able to predict the incoming of a rainy period? Future numerical analyses together with focused and enlightened observations will put in light other interesting features of this very interdisciplinary research field.

Table 3.6 – Pearson correlation coefficients for location Baja Ca.

Baja Ca	$\rho_{\bar{\tau},H}$	$\rho_{\bar{\tau},U^*}$	$\rho_{\bar{\tau},W^*}$	$\rho_{\bar{\tau},L}$	$\rho_{\bar{\tau},Z_i}$
January	0.42	0.53	0.67	-0.51	0.50
April	0.33	0.44	0.60	-0.53	0.46
July	0.32	0.55	0.69	-0.49	0.51
October	0.41	0.62	0.63	-0.49	0.53
Year	0.27	0.42	0.60	-0.51	0.52

Table 3.7 – Pearson correlation coefficients for location Crops Okla.

Crops Okla	$\rho_{\bar{\tau},H}$	$\rho_{\bar{\tau},U^*}$	$\rho_{\bar{\tau},W^*}$	$\rho_{\bar{\tau},L}$	$\rho_{\bar{\tau},Z_i}$
January	0.43	0.51	0.53	-0.63	0.39
April	0.42	0.45	0.55	-0.46	0.33
July	0.39	0.58	0.68	-0.75	0.59
October	0.50	0.54	0.62	-0.63	0.44
Year	0.39	0.51	0.63	-0.59	0.49

Table 3.8 – Pearson correlation coefficients for location Tobacco NC.

Tobacco NC	$\rho_{\bar{\tau},H}$	$\rho_{\bar{\tau},U^*}$	$\rho_{\bar{\tau},W^*}$	$\rho_{\bar{\tau},L}$	$\rho_{\bar{\tau},Z_i}$
January	0.26	0.54	0.60	-0.54	0.39
April	0.39	0.58	0.56	-0.61	0.38
July	0.43	0.47	0.56	-0.54	0.44
October	0.34	0.41	0.53	-0.48	0.37
Year	0.33	0.52	0.58	-0.54	0.44

Table 3.9 – Pearson correlation coefficients for location Crops CA.

Crops CA	$\rho_{\bar{\tau},H}$	$\rho_{\bar{\tau},U^*}$	$\rho_{\bar{\tau},W^*}$	$\rho_{\bar{\tau},L}$	$\rho_{\bar{\tau},Z_i}$
January	0.33	0.42	0.53	-0.53	0.58
April	0.34	0.52	0.57	-0.62	0.49
July	0.36	0.51	0.63	-0.70	0.61
October	0.37	0.56	0.61	-0.63	0.51
Year	0.29	0.38	0.52	-0.57	0.54

Table 3.10 – Pearson correlation coefficients for location Forest Colorado.

Forest Colorado	$\rho_{\bar{\tau},H}$	$\rho_{\bar{\tau},U^*}$	$\rho_{\bar{\tau},W^*}$	$\rho_{\bar{\tau},L}$	$\rho_{\bar{\tau},Z_i}$
January	0.15	0.49	0.31	-0.33	0.45
April	0.21	0.35	0.34	-0.39	0.26
July	0.34	0.59	0.54	-0.59	0.10
October	0.34	0.60	0.51	-0.59	0.39
Year	0.23	0.10	0.32	-0.32	0.33

Table 3.11 – Pearson correlation coefficients for location Veggies WI.

Veggies WI	$\rho_{\bar{\tau},H}$	$\rho_{\bar{\tau},U^*}$	$\rho_{\bar{\tau},W^*}$	$\rho_{\bar{\tau},L}$	$\rho_{\bar{\tau},Z_i}$
January	0.28	0.45	0.35	-0.57	0.49
April	0.32	0.55	0.53	-0.57	0.18
July	0.33	0.49	0.66	-0.66	0.57
October	0.40	0.43	0.47	-0.55	0.15
Year	0.30	0.52	0.63	-0.59	0.45

Table 3.12 – Pearson correlation coefficients for location Wild Canada.

Wild Canada	$\rho_{\bar{\tau},H}$	$\rho_{\bar{\tau},U^*}$	$\rho_{\bar{\tau},W^*}$	$\rho_{\bar{\tau},L}$	$\rho_{\bar{\tau},Z_i}$
January	0.14	0.51	0.51	-0.40	0.35
April	0.43	0.46	0.50	-0.55	0.32
July	0.34	0.47	0.53	-0.54	0.23
October	0.32	0.46	0.53	-0.55	0.42
Year	0.30	0.42	0.51	-0.49	0.30

Table 3.13 – Pearson correlation coefficients for location Wheat Alberta.

Wheat Alberta	$\rho_{\bar{\tau},H}$	$\rho_{\bar{\tau},U^*}$	$\rho_{\bar{\tau},W^*}$	$\rho_{\bar{\tau},L}$	$\rho_{\bar{\tau},Z_i}$
January	0.10	0.49	0.45	-0.42	0.34
April	0.29	0.36	0.53	-0.57	0.47
July	0.39	0.49	0.64	-0.77	0.48
October	0.42	0.53	0.62	-0.58	0.33
Year	0.27	0.48	0.64	-0.63	0.47

Chapter 4

Eddy diffusivities in sea surface dispersion

As pointed out in chapter 2 the specific choice of an eddy diffusivity closure is not unique and strongly depends on the particular application. In this chapter the passive tracer problem on the sea surface is studied. Several closures are compared giving in some cases apparently counterintuitive results thus rising the necessity to develop new models for such cases.

4.1 The strategy

To compare the efficiency of different eddy diffusivity closures I developed the following strategy. Given an advective field $\mathbf{v}(\mathbf{x}, t)$ with a certain resolution (henceforth the fully resolved field FRF), a realistic situation, in which only the dynamics up to certain scales is known, can be mimed removing the small-scale contribution. This can be done, for instance, by a low-pass filter in the wave-number space (figure 4.1).

Such a filter simply consists in turning off from the spatial Fourier transform of the FRF all the modes related to wave numbers higher than a chosen cutoff and then coming back to the ordinary space. The procedure gives a field with a coarser resolution with respect to the FRF and we will refer to it as the large-scale field LSF.

Once the LSF is produced, transport can be numerically studied either in the FRF, or in the LSF, or in the LSF adopting different Eddy Diffusivity schemes too. Finally the reliability of a closure is measured in terms of the discrepancy between the behaviour of dispersal statistics in the FRF and in the LSF adopting the chosen scheme. Moreover the reliability of every closure will be studied moving the cutoff position in the wave number space.

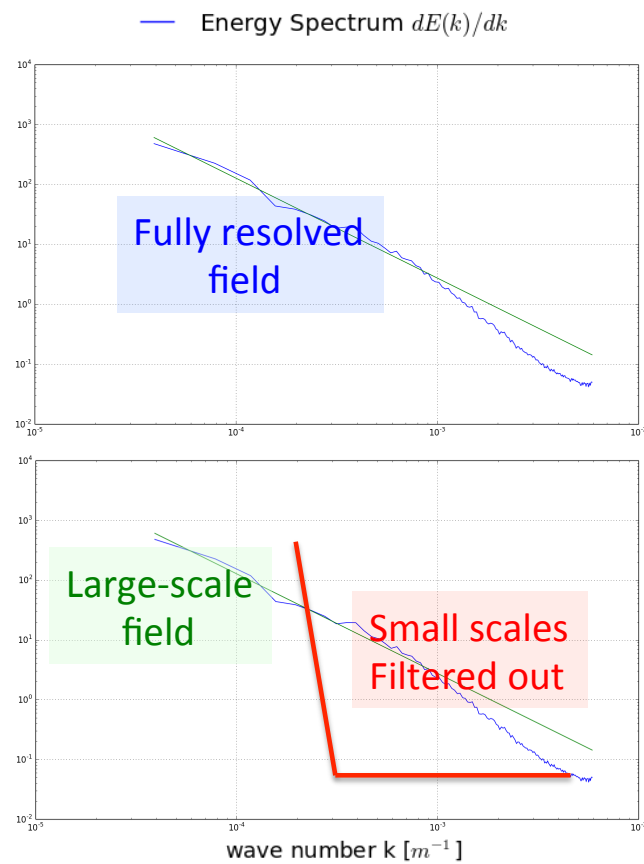


Figure 4.1 – Sketch of how the strategy works: the large-scale field is produced filtering out the smallest dynamical scales in the fully resolved field. In the energy spectrum the contribution of all the modes with wave numbers higher than a chosen cutoff is removed.

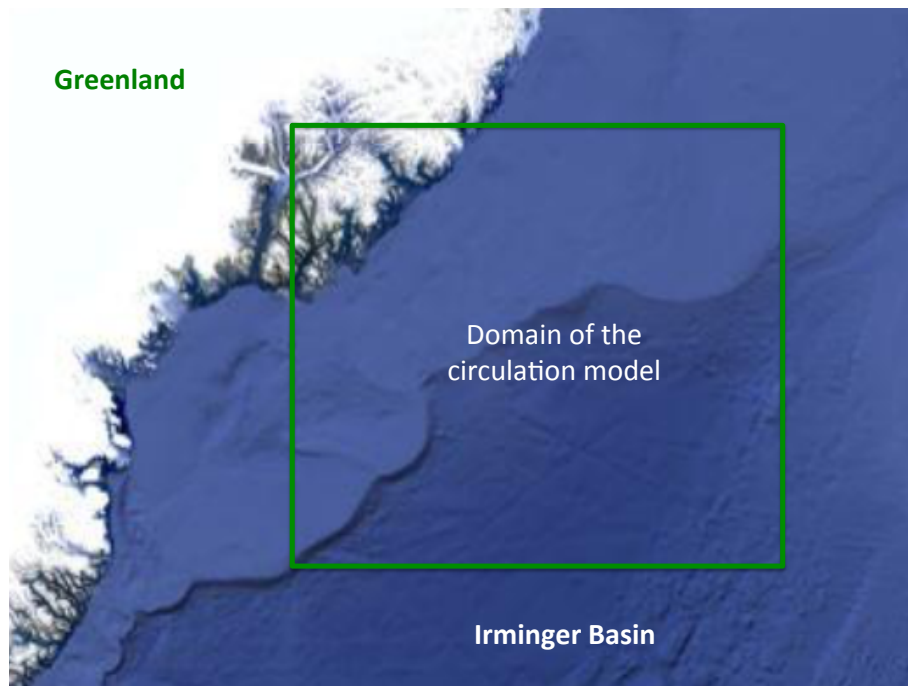


Figure 4.2 – *The geographic area in which the circulation is given.*

4.2 Advective fields

Advective fields are required in order to realize the strategy. I focused my attention on a case study in the Arctic region: the Southeast Greenland shelf, adjacent to the Irminger Basin 4.2. As studied in details in recent works ([9]), this case is dynamically important because of dense water cascades falling down the shelf. This phenomenon is dominated by a complex interplay between different components of the local current system. Hence vertical motions are relevant and the dynamics cannot be treated in terms of a shallow water approximation.

The surface component, on which we are focusing the attention, is made up of light waters of both Atlantic and Arctic origins, which flow next to each other and form the strong Irminger Current/East Greenland Current front.

The dataset contains the information about zonal and meridional components of the current. Fields are given on a Arakawa-C staggered grid that covers the geographical area corresponding to latitudes from 63.690N to 66.574N and longitudes from 37.036W to 29.076W, with a nominal spatial resolution of about 500 meters. The dataset was produced with a setup of the MIT general circulation model (MITgcm, [10]) and validated with field observations. For more details about the setup of the circulation model refer to ([9]). The computational time step is 6 s and fields are available with a sampling time of 3 hours for the simulated period starting the 1th June 2003 and ending the 1th September 2003. A further time series, sampled every 10 minutes, is available only for 3 days in the simulated period. The computational domain, and hence the produced field, is three-dimensional. Because we are interested on the sea-surface transport, only the surface flow is retained.

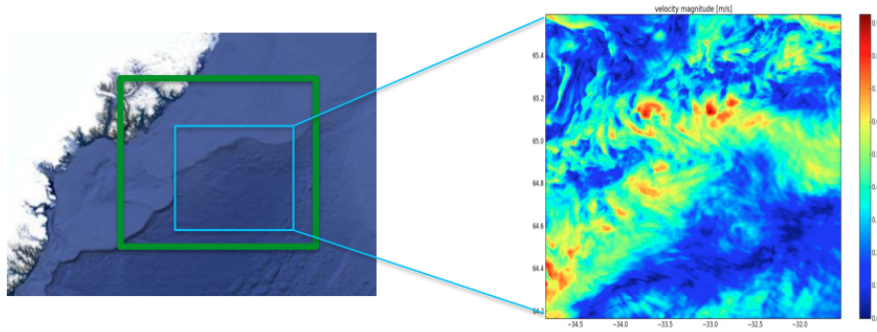


Figure 4.3 – Both preliminary analysis and transport simulations are performed in the subdomain inside the blue square. The side of this area is about 150 km.

Both the preliminary analysis of the advective fields and the transport simulations are performed on a squared subdomain, with side of 150 km (figure 4.3). In the following the results of a preliminary analysis are shown.

4.2.1 Field analysis

The geographical area is affected by strong currents, also at the surface level (see the top-left histogram in figure 4.4). Moreover, the direction of the stream is well defined (westward), for the whole simulated period, as can be seen in the top-right histogram of figure 4.4, where the time signal of the specific kinetic energy (kinetic energy per unit mass) is shown too. All the quantities represented in figure 4.4 are averaged over the grid points and varying in time. The bottom topography of the basin is characterized by a well-defined shelf. The cross section of the bathymetry showed in the left panel of figure 4.5 gives the idea of the shelf slope: the sea depth changes from 300 m to 2500 m in about 100 km of horizontal displacement, with the aforementioned implications on the dynamics.

Fourier analysis

The main goal of this work is to investigate what happens when the transport is studied with a partial knowledge of the carrying flow, i.e. when the resolution is limited to certain spatial scales. What happens to the dispersion if the effect of the unknown scales is totally neglected? How can one restore for applications the lack of information via an effective model? All these questions are relevant and proper quantities had to be defined to deal with them. For this aim the mathematical tool of Fourier decomposition has been used in the analysis, decomposing the velocity field in spatial Fourier modes that are oscillating in space with different wave vectors \mathbf{k} . In this framework, each spatial length scale λ in the advective field is associated to all Fourier modes characterized by the same magnitude $k = \frac{2\pi}{\lambda}$ of the wave vectors.

The strategy needs to know the behaviour of the advective field at each involved length scale. Hence, at each time step, the spatial Fourier transform of

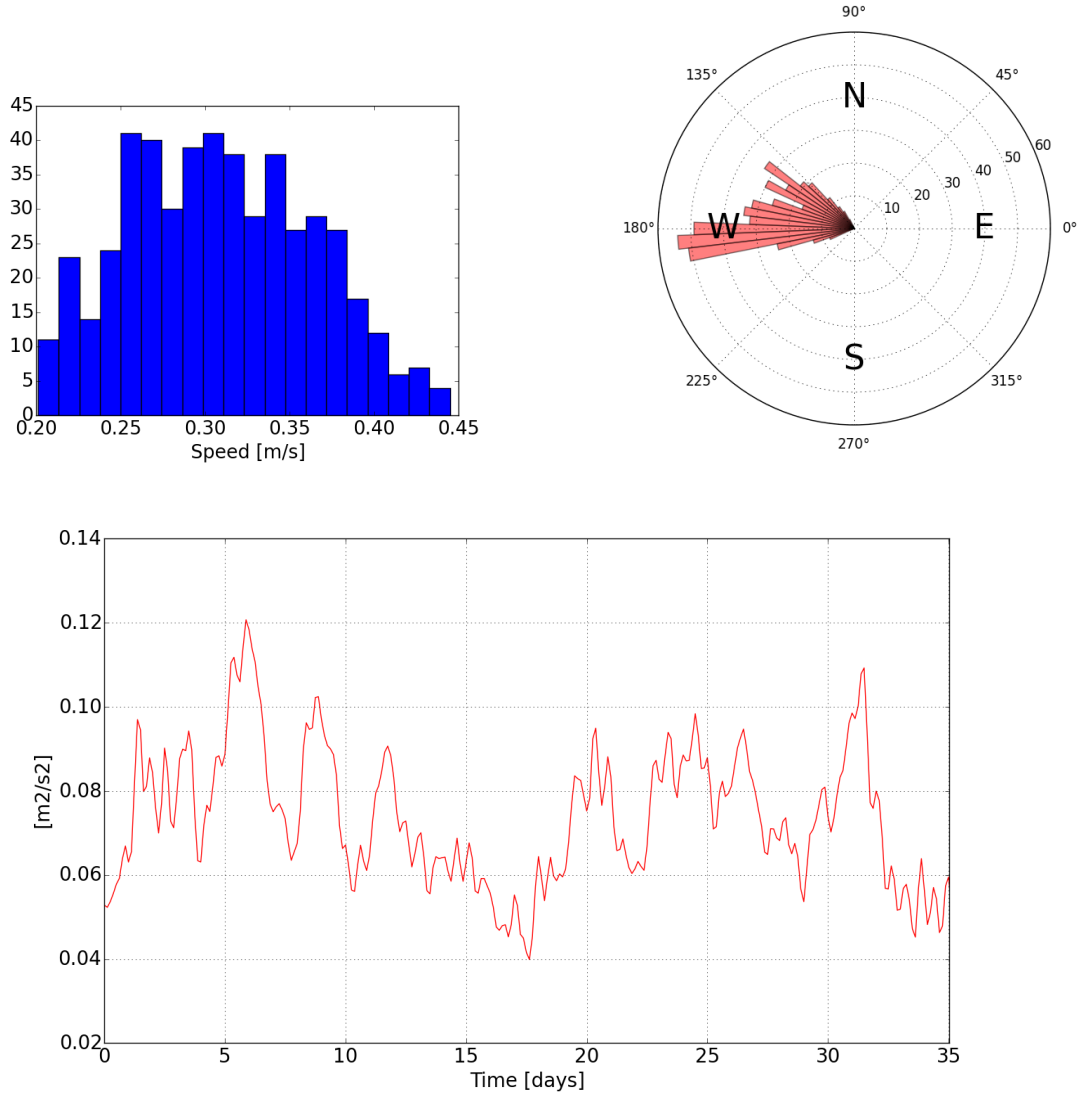


Figure 4.4 – *Upper left: histogram of the spatial averaging at fixed times of the current speed inside the domain; Upper right: polar histogram of the direction of the current averaged in space at fixed times; Lower: time series of spatially averaged kinetic energy per unit mass.*

the velocity field has been computed adopting the following conventions on the direct and inverse transform:

$$\hat{f}(\mathbf{k}) = \int e^{-i\mathbf{k}\cdot\mathbf{x}} f(\mathbf{x}) d^n \mathbf{x},$$

$$f(\mathbf{x}) = \frac{1}{(2\pi)^n} \int e^{+i\mathbf{k}\cdot\mathbf{x}} \hat{f}(\mathbf{k}) d^n \mathbf{k},$$

thus giving the following form for Parseval's identity in the case of $n = 2$:

$$\int f^2(\mathbf{x}) d^2 \mathbf{x} = \frac{1}{(2\pi)^2} \int |\hat{f}(\mathbf{k})|^2 d^2 \mathbf{k}.$$

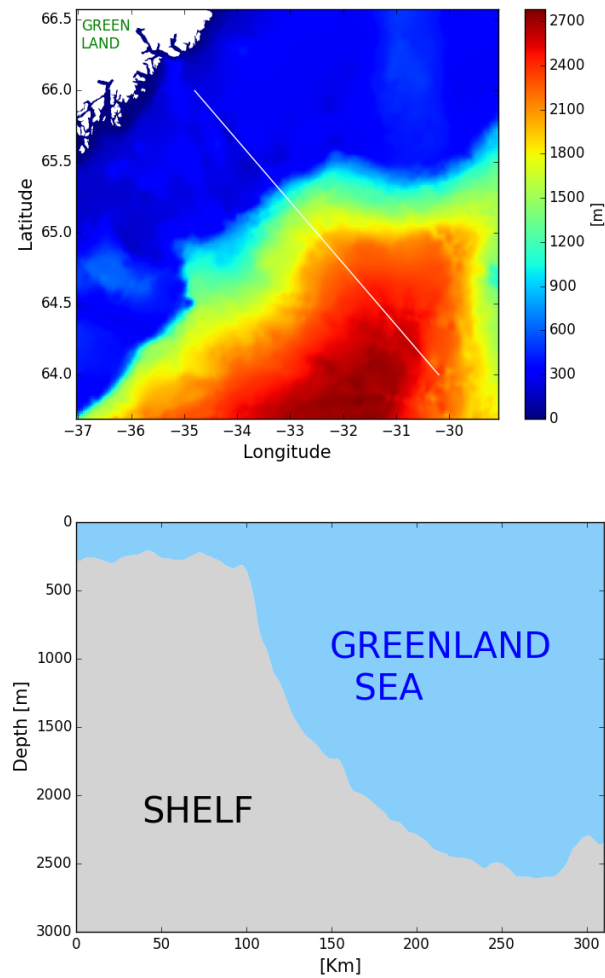


Figure 4.5 – Bathymetry inside the domain and slope of the shelf. *Up*: the continental shelf very sharp in the geographic area of the case. The white line is a top view of the cross section shown in right panel. *Down*: Cross section of the shelf that gives the idea of its slope.

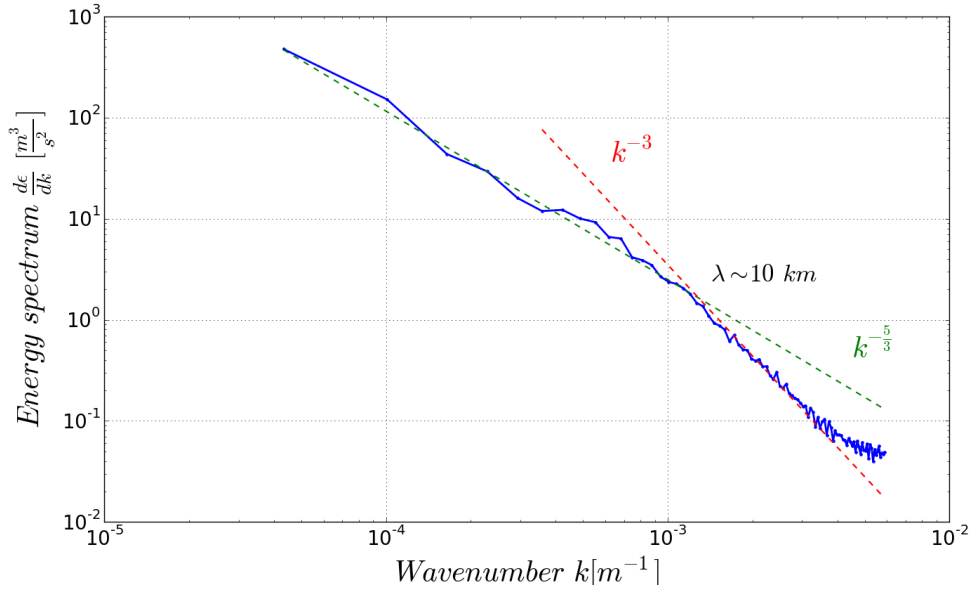


Figure 4.6 – Energy spectrum calculated averaging over angular coordinates in the k -space. In agreement with the Kolmogorov law, it shows a clear range of k s with energies that follow a $k^{-5/3}$ law up to scales of the order of ~ 10 km

The first important information obtained is how the kinetic energy is distributed on spatial scales. Therefore, starting from the averaged kinetic energy per unit mass

$$\epsilon = \frac{E_{Kin}}{M} = \frac{1}{2} \frac{\int |\mathbf{u}(\mathbf{x}, t)|^2 d\mathbf{x}}{\int d\mathbf{x}} = \frac{1}{2} \langle |\mathbf{u}(\mathbf{x}, t)|^2 \rangle_V,$$

(where V is the volume of a grid cell) and using the Parseval's identity, the isotropic energy spectrum (IES) can be defined as:

$$S(k) = \frac{d\epsilon}{dk} = \frac{k}{4\pi V} (|\hat{u}(k)|^2 + |\hat{v}(k)|^2).$$

This quantity is related to the energy density carried by all modes associated to a specific length scale λ .

With this convention I computed the IES of the velocity field for each sampled time of the advective field. An example is showed in figure 4.6. Here the IES shows the presence of an inertial range in the wavenumber space that involves wavenumbers up to $k = 10^4 \text{ m}^{-1}$. This range follows the Kolmogorov law, being the spectrum proportional to $k^{-5/3}$. For higher values of k (smaller spatial scales) the spectrum follows a different power law and the associated energies decrease faster. Further important quantities to be evaluated are the correlation times associated with different spatial scales. Indeed the turbulent nature of the flow allows to model the time signal of each Fourier mode as a random process with a characteristic correlation time $\tau(\mathbf{k})$. For each mode, such characteristic time can be computed from the correlation functions

$$C_x(t, t', \mathbf{k}) = \langle \hat{u}(t, \mathbf{k}) \hat{u}^*(t', \mathbf{k}) \rangle, \quad C_y(t, t', \mathbf{k}) = \langle \hat{v}(t, \mathbf{k}) \hat{v}^*(t', \mathbf{k}) \rangle,$$

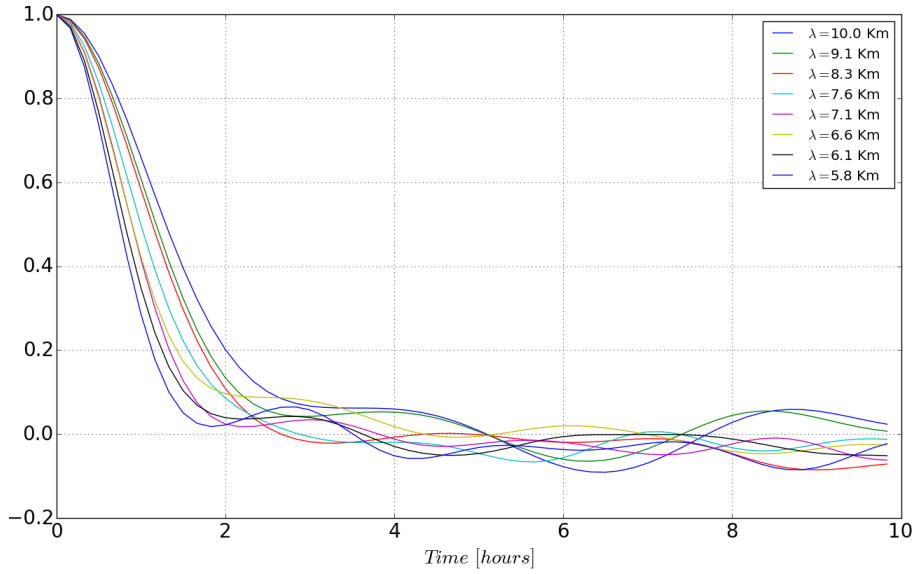


Figure 4.7 – Normalized autocorrelations permit to appreciate also qualitatively that correlation times decrease with the wave number.

where the angular brackets denote the average over an ensemble of different realizations and the $*$ indicates the complex conjugate. Assuming the process to be statistically stationary at the considered scale, the ensemble average is replaced by the average on time and the correlation becomes simply a function of the time lag $T = t' - t$:

$$C_x(T, \mathbf{k}) = \langle \hat{u}(t, \mathbf{k}) \hat{u}^*(t + T, \mathbf{k}) \rangle, \quad C_y(T, \mathbf{k}) = \langle \hat{v}(t, \mathbf{k}) \hat{v}^*(t + T, \mathbf{k}) \rangle.$$

Moreover, being the amplitude of a Fourier mode a complex signal, the correlation function is complex too and the correlation time can be evaluated from its real part as the time for this function to approach zero, i.e. after this time the signal is uncorrelated with itself. Once the correlation function had been computed, a further averaging procedure has been applied in order to obtain the correlation associated to a particular length scale: all functions belonging to modes with the same magnitude of the wave vector has been averaged together. This procedure corresponds to averaging over all angles in the wave vector space, keeping fixed magnitude of k (henceforth k -shell averaging). The resulting correlations, normalized with the variances of the signals, are shown in figure 4.7 for some length scales. As can be seen, the characteristic times decrease together with the length scale, that is, smaller scales are less correlated in time. Then correlation times can be computed, alternatively, as the integral in time of the normalized functions. Both the procedures has been implemented and lead to very similar results.

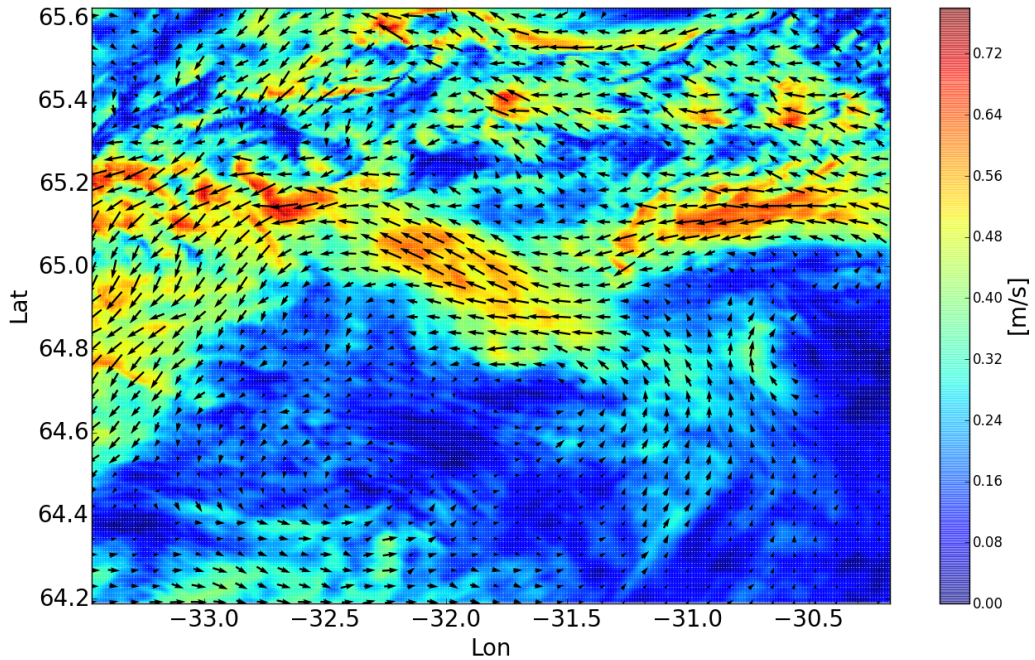


Figure 4.8 – Fully resolved field: snapshot of the advective velocity in the FRF at a fixed time: the color represents the current speed and arrows the direction. Notice that many small-scale structures are present in the flow.

4.2.2 Filtered fields

A crucial step to carry out the strategy is the production of the filtered LSF, to mimik the inevitable lack in the knowledge of the advective field. Several different datasets have been created for the LSF changing the position of the cutoff in the wavenumber space for the filtering procedure. Figures 4.8 and 4.9 show snapshots of the FRF and two LSFs generated with different cutoffs and corresponding to length scale of $\sim 12 \text{ km}$ and $\sim 30 \text{ km}$. It is evident that many dynamical structures are removed in the filtering process.

4.3 Modeling transport

The transport process is described adopting a Lagrangian approach and considering the dispersed particles as passive tracers. Therefore, for each simulation, an ensemble of particles is released in the advecting flow, computing the statistics of certain relevant quantities.

When the unresolved dynamics is completely neglected, the motion of each particle is deterministic and described by a first order ODE. On the other hand, when an Eddy Diffusivity D^E scheme is adopted, the small-scales effect is described via a stochastic process, making the equation of motion a stochastic differential

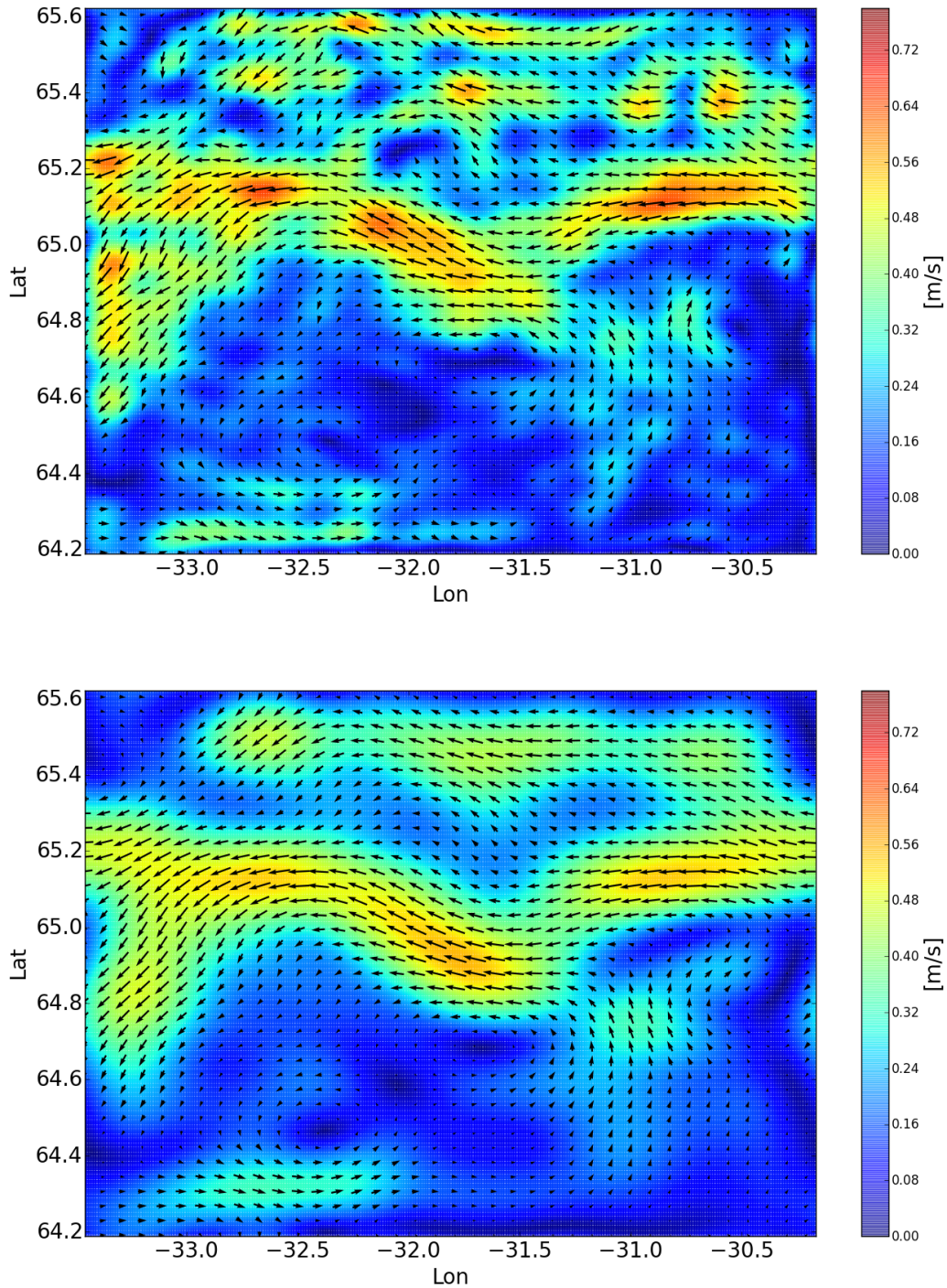


Figure 4.9 – Filtered fields: snapshots of the advective velocity in two LSF generated with different cutoffs. Up: cutoff wavenumber $k = 5 \cdot 10^{-4} \text{ m}^{-1}$; Down: cutoff wavenumber $k = 2 \cdot 10^{-4} \text{ m}^{-1}$. Notice the progressive reduction of structures when the cutoff is reduced

equation:

$$\frac{d\mathbf{x}(t)}{dt} = \mathbf{V}_{Ad}[\mathbf{x}(t), t] + \boldsymbol{\sigma}[\mathbf{x}(t), t]\boldsymbol{\eta}, \quad (4.1)$$

where $\mathbf{V}_{Ad}[\mathbf{x}(t), t]$ is the value of the advective field interpolated at the particle position at time t , $\boldsymbol{\sigma}$ is the unique positive-definite solution of the matrix equation $D_{ij}^E(\mathbf{x}, t) = \frac{1}{2}(\sigma_{ip}(\mathbf{x}, t)\sigma_{jp}(\mathbf{x}, t))$, and $\boldsymbol{\eta}$ is a delta-correlated random vector, extracted at each time step for each particle, according to a Gaussian distribution with mean value equal to zero and unit variance. In this framework the most general case, in which \mathbf{D}^E is a tensor field, is considered.

4.3.1 Numerical solution techniques

All simulations have been performed with a Lagrangian numerical model, whose source code has been written by the author using the C++ programming language. Modeling or not the effect of the unresolved dynamics requires different numerical techniques. If small-scale effects are neglected, simulations are done solving first order ODEs. In this case, an explicit Runge-Kutta method of order four has been implemented to compute the temporal evolution. Advective velocities at time t in the particle position are estimated by linear interpolation either in space and time.

The use of an Eddy Diffusivity model involves the introduction of a random component to particle velocities, in addition to the advective contribution. The aim of this component is to mimik turbulent diffusion, spreading particles in the same position, according to the value of the Eddy Diffusivity tensor field at such position. Therefore, every time step, for every particle, a bidimensional vector of random numbers is extracted from Gaussian distributions whose standard deviation is modulated according to the local values of $D_{ij}^E(\mathbf{x}, t)$ components.

The discretization of equation (4.1), that has been implemented in the code, is

$$X_i(t + \Delta t) - X_i(t) = \Delta t \left[V_{Adv,i}(\mathbf{X}, t) + \frac{1}{\sqrt{\Delta t}} \sigma_{ij}(\mathbf{X}, t) \eta_j \right]$$

with the above mentioned relationship between tensors $\boldsymbol{\sigma}$ and \mathbf{D}^E . Also in this case Advective and Eddy Diffusivity fields are linearly interpolated either in space and time.

As boundary condition particle trajectories are stopped once they reach the boundaries of the computational domain. The time step has been set to 10 min , ensuring that the particle displacement during one step doesn't exceed the grid size, i.e. satisfying the condition:

$$\frac{\Delta t \max\{V_{Adv}\}}{\Delta x} < 1$$

where Δx is the spatial resolution of the advective field.

Eddy Diffusivities

Two models to describe the subgrid scales motion have been used. In the first case a constant scalar value for the Eddy Diffusivity is used, depending on the grid size of the advective velocity field:

$$D^E = 2.055 \cdot 10^{-4} \Delta x^{1.15}$$

This formula is named the Okubo's expression for the turbulent diffusivity and it is largely used for oceanographic applications [18]. The value of Δx has been identified with the characteristic length λ , associated with the cutoff wave number $k_L = \frac{2\pi}{\lambda}$ chosen in filtering the FRF.

The second model consists in explicit expressions for the components of the Eddy diffusivity tensor as a function of the advective velocity components and other parameters related to the unresolved scales. The tensor form of such expressions, obtained by Boi et al. in [17] is:

$$D_{\beta\gamma} = \frac{u_{rms}^2}{\alpha^2} \frac{\left[\frac{\alpha^2}{u_{rms}^2} |\mathbf{U}|^2 U_\beta U_\gamma + (|\mathbf{U}|^2 \delta_{\beta\gamma} - 2U_\beta U_\gamma) \left(\sqrt{\frac{\alpha^2}{u_{rms}^2 |\mathbf{U}|^2 + 1} - 1} \right) \right]}{\sqrt{\frac{\alpha^2}{u_{rms}^2} |\mathbf{U}|^2 + 1} |\mathbf{U}|^4} \sum_{i=1}^N \frac{B_i}{2} \tau_i \quad (4.2)$$

where \mathbf{U} is large-scale velocity vector in the the considered position. The constant u_{rms} is the the root mean square velocity of the FRF and it is simply related to the whole kinetic energy by:

$$u_{rms} = \sqrt{2E_{kin}} = \sqrt{2(E_{LSF} + TKE)}$$

E_{LSF} being the kinetic energy of the large scale field, and TKE is the turbulent kinetic energy of the unresolved scales. This quantities have been evaluated during the filtering process. Figure 4.10 shows the time series of u_{rms} and $\sqrt{2TKE}$ in the case of LSF produced with a cutoff wavenumber $k_L = 2 \cdot 10^{-4} m^{-1}$.

The index i runs among the unresolved wavenumbers k_i and τ_i is the associated correlation time that has been computed from the analysis of the correlation function described in section 4.2.1.

The other constants $\{B_i\}$, involved in the summation, are related to the energy spectrum:

$$E(k_i) \delta k_i = \frac{1}{4} B_i \quad E_{kin} = \frac{1}{4} \sum_{i=1}^N B_i$$

where $E(k_i) \delta k_i$ is the energy of all modes inside a thin shell, of radius k_i and thickness δk_i , in the wave-vector space. Moreover, if the unresolved field obeys the Kolmogorov 1941 theory, $E(k_i) = C \epsilon^{2/3} k_i^{-5/3}$, where C is the Kolmogorov constant and ϵ denotes the energy dissipation rate. Consequently one has that

$$B_i = 4C \epsilon^{2/3} k_i^{-5/3} \delta k_i$$

and, by definition of turbulent kinetic energy $TKE \equiv \int_{k_L}^{\infty} E(k) dk$, it turns that

$$C \epsilon^{2/3} = \frac{2}{3} TKE k_L^{2/3}.$$

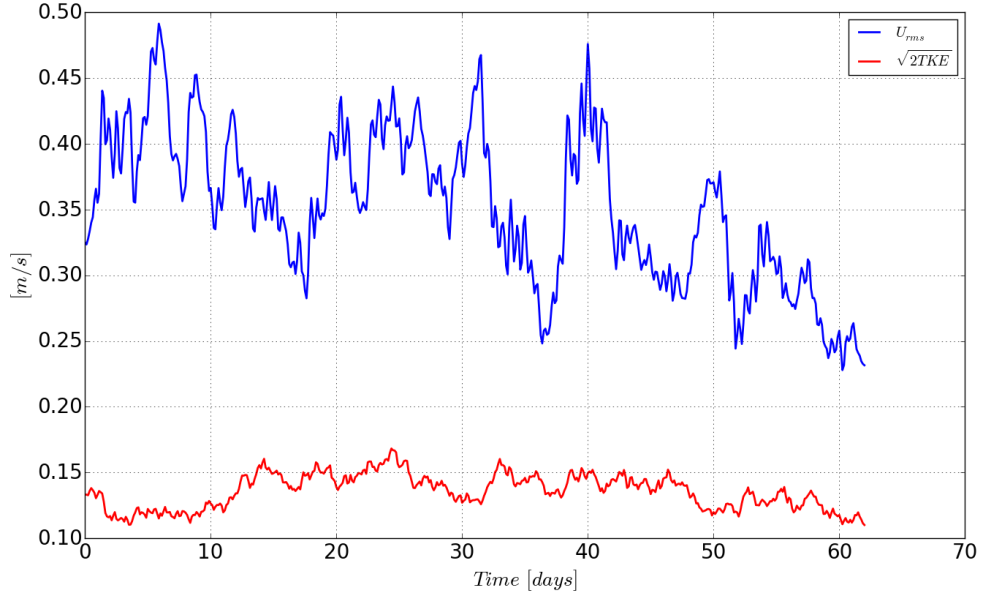


Figure 4.10 – Comparison between time series of U_{rms} (blue signal) and of a characteristic turbulent velocity scale computed as $\sqrt{2TKE}$ (red signal), for a cutoff $k_L = 2 \cdot 10^{-4} m^{-1}$. This figure gives the idea of the relative importance of removed scales in the transport.

This relationship is very useful in realistic applications because the TKE is easily accessible in many CFD models (both RANS and LES).

Finally the dimensionless constant α is a free tuning parameter, typically of order 1. In the present work α has been evaluated by a best fit, assuming the following functional relationship between τ and k :

$$\tau_i = \frac{\alpha}{U_{rms} k_i}$$

that is supported by numerical evidence reported by Kaneda et al. [32]. Then the obtained value is $\alpha \sim 1.2$.

With the knowledge of all involved parameters and given a LSF, it is then possible to produce the relative field for each of the three independent components of the Eddy Diffusivity tensor. Figures 4.11, 4.12 and 4.13 show the result of this computation at a fixed time, for a cutoff $k_L = 2 \cdot 10^{-4} m^{-1}$.

4.3.2 Numerical simulations

Keeping in mind the purpose of evaluating the goodness of different models for the unresolved turbulence, every run has been repeated, starting from the same initial condition and releasing particles in the FRF, in the LSF and also in the LSF using an Eddy Diffusivity model. The LSF chosen for the comparison has been produced with a cutoff wavenumber $k_L = 2 \cdot 10^{-4} m^{-1}$, corresponding to a length scale of about 30 km. On one hand this choice gives correlations times,

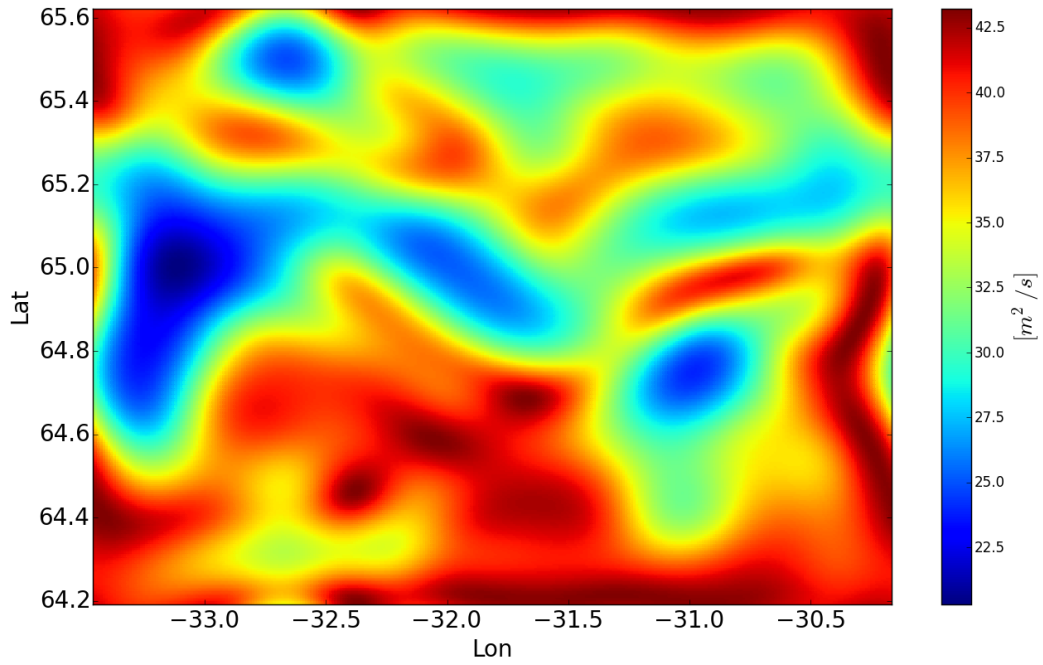


Figure 4.11 – Snapshot of the D_{11} field calculated for $k_L = 2 \cdot 10^{-4} m^{-1}$.

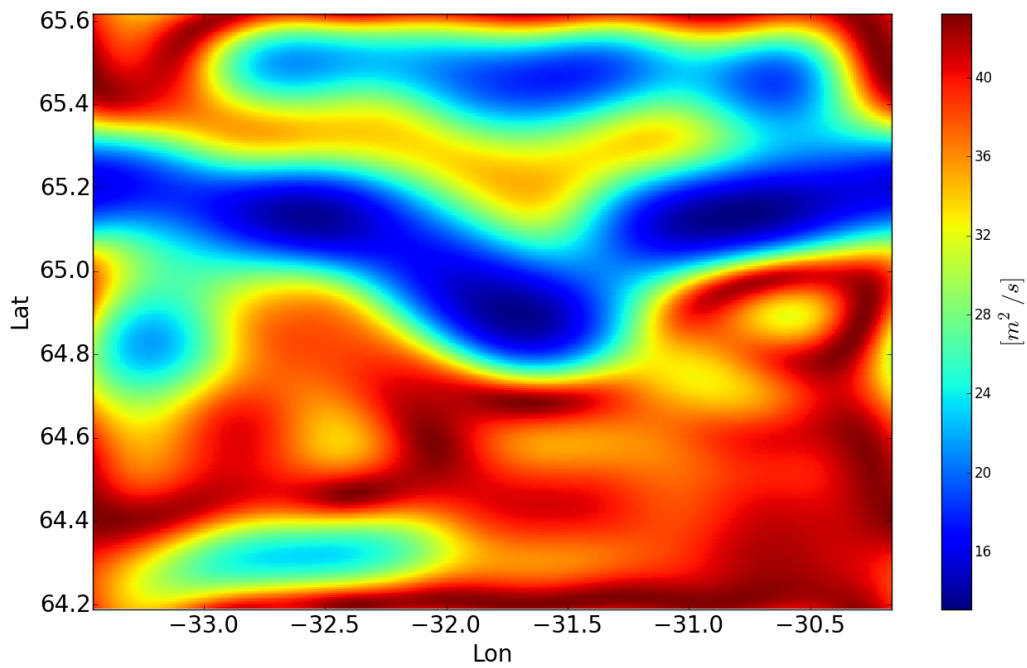


Figure 4.12 – Snapshot of the D_{22} field calculated for $k_L = 2 \cdot 10^{-4} m^{-1}$.

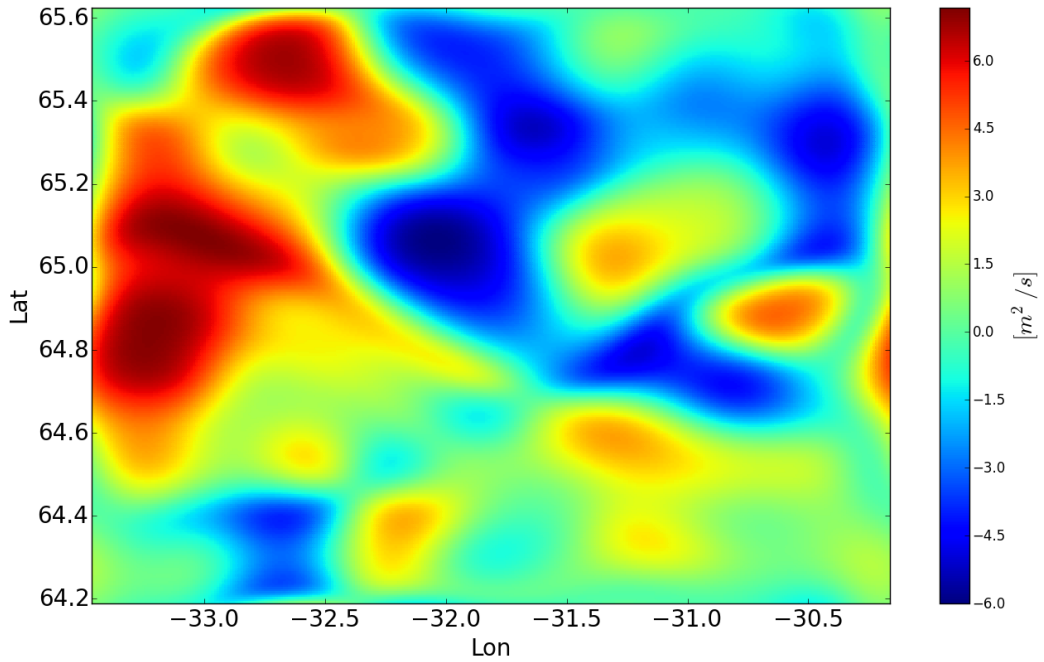


Figure 4.13 – Snapshot of the the extra-diagonal component of the Eddy Diffusivity tensor field $D_{12} = D_{21}$, calculated for $k_L = 2 \cdot 10^{-4} \text{ m}^{-1}$.

in the unresolved field, that are not too long with respect to the chosen time step. On the other hand the filter is quite strong, giving to the dispersion an appreciable role in the dynamics.

For the computation, the particle positions and advective fields are mapped on an internal Cartesian grid, with the x -axis along the east direction, the y -axis northward and the origin is placed on the left-down corner of the computational domain.

Since the direction of the mean current is always westward, in order to maximize the domain crossing time, the starting distribution of particles positions has been chosen near the east boundary. Particles are released uniformly on a square, centered about 110 km east of the west boundary and at the mean latitude. The side of the square is chosen to be like the characteristic cutoff wavelength.

The number of released particles for each run has been set to 250000, ensuring the convergence of observed statistics. A new group of simulation with the same initial condition started every 9 hours and particle positions has been saved every hour.

Statistics of the dispersion

In order to measure the dispersion the components of the displacement from the initial position:

$$M_X = \langle x - x_0 \rangle, \quad M_Y = \langle y - y_0 \rangle$$

has been computed (brackets denote the average over the ensemble of all the released particles). The statistics of this observables gives a quantification of the dispersion process. The variances of the displacement are measures of the turbulent diffusion coefficient from a Lagrangian point of view. Indeed their asymptotic behaviour gives the diffusion tensor components:

$$Var_{ij} = \langle (x_i - x_{0i} - M_i)(x_j - x_{0j} - M_j) \rangle \rightarrow 2D_{ij}t.$$

Hence these quantities can be used to compare the reliability of different methods in numerical description of the large-scale transport.

Results

A close look at the resulting behavior of the statistical observable reveals unexpected results. By construction the LSF consists in turning off some dynamical Fourier modes. Consequently the energy amount of the LSF is always less than the corresponding FRF. Hence the energy amount available for turbulent diffusion, typically associated with smaller scales, is significantly reduced in the LSC and then, without any Eddy Diffusivity model, the displacement variances are expected to increase more slowly in the LSF than in the FRF.

Surprisingly, in most cases, this fact is not true. Figures 4.14, 4.15 and 4.16 are related to three different initial conditions and, in all cases, the LSF is more diffusive than FRF. Moreover, the introduction of an Eddy Diffusivity scheme deteriorates the agreement with the FRF.

Why does this, at first look, counterintuitive fact happen? A look at the spatial distribution of particles gives an hint. Comparing two snapshots of particle positions, after the same time from the release but within the FRF and the LSF, shows a clear clustering effect in the first case. As can be seen in figure 4.17 particles are repelled from certain region and attracted on structures that show characteristic length scales lower than the cutoff length. This is a clear effect of compressibility. Of course, this does not mean that water is compressible, but simply that in a 2D cut of a 3D field mass is not conserved. It is generally believed that this effect is negligible in the ocean. We actually found that such an effect has important consequences on surface transport. Hence, even if the tridimensional velocity fields are actually incompressible, as imposed by the equations of the circulation model, the surface transport is given by a bidimensional restriction of such fields. If vertical motions are significant, as in the present domain, this produce an effective compressibility in the advective field. To support this idea, a further step in the analysis has been done using a compressibility index introduced in [11]:

$$\mathcal{I} = \frac{\langle (\nabla_i v^i)^2 \rangle}{\langle (\nabla_i v^j)^2 \rangle}$$

where angular brackets indicates the average over all grid points. This index is zero in the perfectly incompressible case. The result of the analysis is plotted in figure 4.18, revealing that in all cases the FRF is more compressible than the

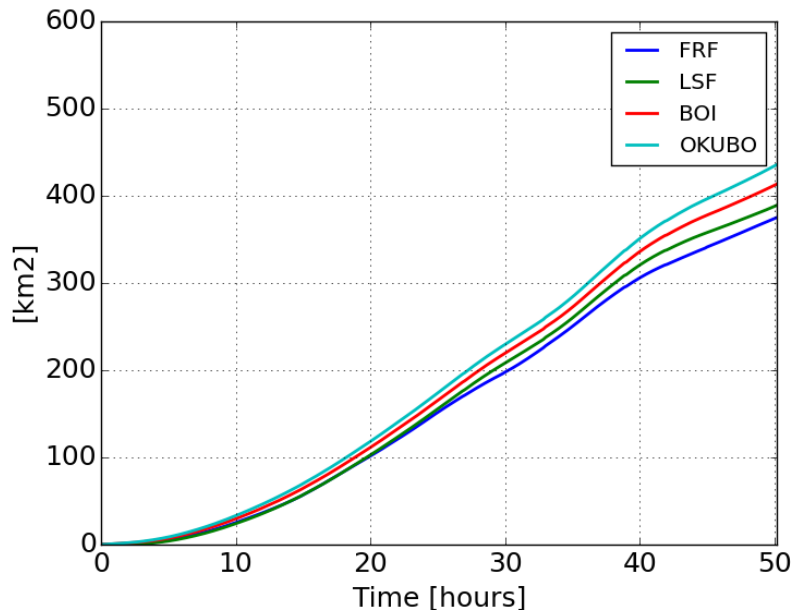


Figure 4.14 – Dispersion is measured looking at the particle displacement variances. This plot shows the evolution in time of $Var_{XX} + Var_{YY}$ for a particular release of particles. The blue line represents the transport in the FRF, the green line in the filtered field without any description of the subgrid dynamics. Red and light blue lines are related with transport simulation in which an Eddy Diffusivity closure has been applied. It is clear that, in this case, Eddy diffusivity closures make worse the description of transport.

LSF. Hence, in this case, the most important contribution to a non-zero divergence comes from filtered scales, consequently producing clustering of particles on attractive structures.

4.3.3 Conclusions

Eddy diffusivities for incompressible flows are largely used in numerical models for passive tracer transport [22]. In many cases they give good results in describing the transport. The hypothesis of incompressible flows is also a good assumption in general for geophysical flows. Anyway dealing with floating tracers on the sea surface requires to consider as advective velocity only the horizontal component of the whole field at the surface. Often this is a good approximation because the vertical component is actually much less important than the others. However, in some cases, the vertical dynamics becomes important and has significant effect also in the horizontal transport.

My work shows how the presence of compressible component on unresolved scales of the advective field, can significantly affect the dispersion of substances in the sea surface. Even if the tridimensional velocity field has no divergence, this compressible component rises anyway when the vertical dynamics in the studied region is relevant, as in the case of the Greenland Sea. In shallow basins, this

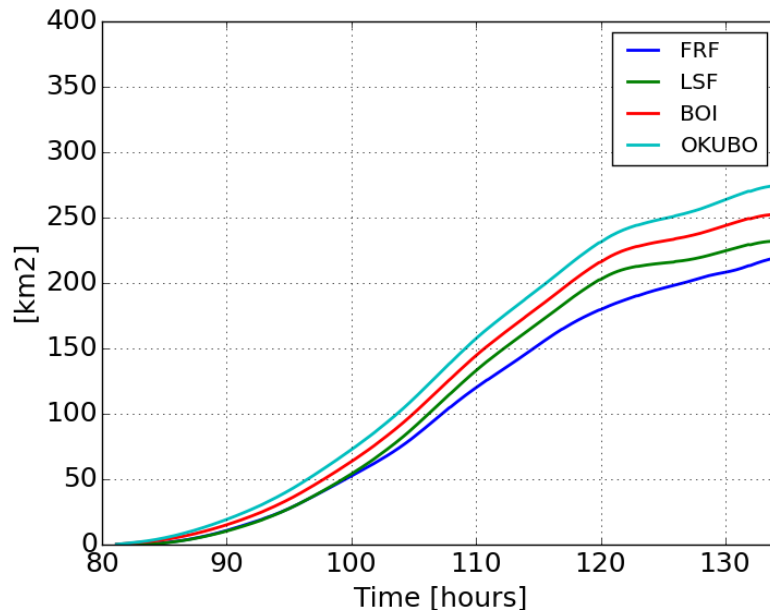


Figure 4.15 – Dispersion is measured looking at the particle displacement variances. This plot shows the evolution in time of $Var_{XX} + Var_{YY}$ for a particular release of particles. The blue line represents the transport in the FRF, the green line in the filtered field without any description of the subgrid dynamics. Red and light blue lines are related with transport simulation in which an Eddy Diffusivity closure has been applied.

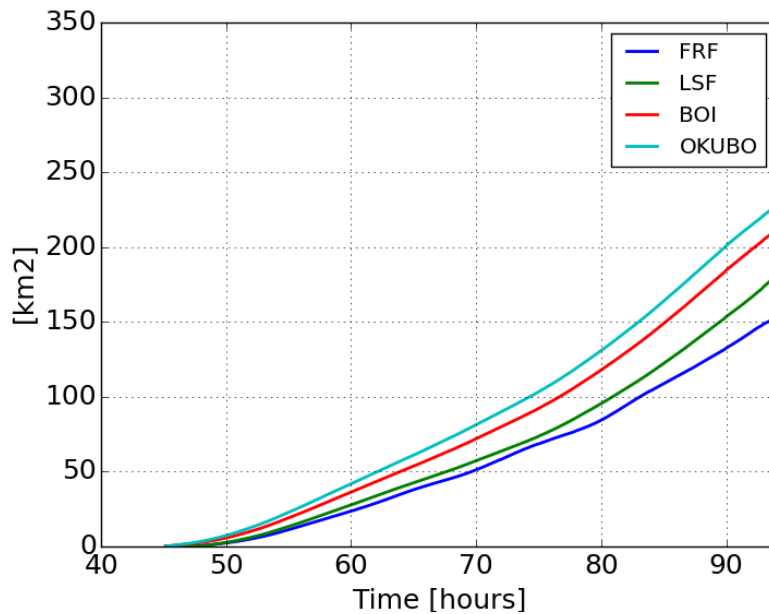


Figure 4.16 – Dispersion is measured looking at the particle displacement variances. This plot shows the evolution in time of $Var_{XX} + Var_{YY}$ for a particular release of particles. The blue line represents the transport in the FRF, the green line in the filtered field without any description of the subgrid dynamics. Red and light blue lines are related with transport simulation in which an Eddy Diffusivity closure has been applied.

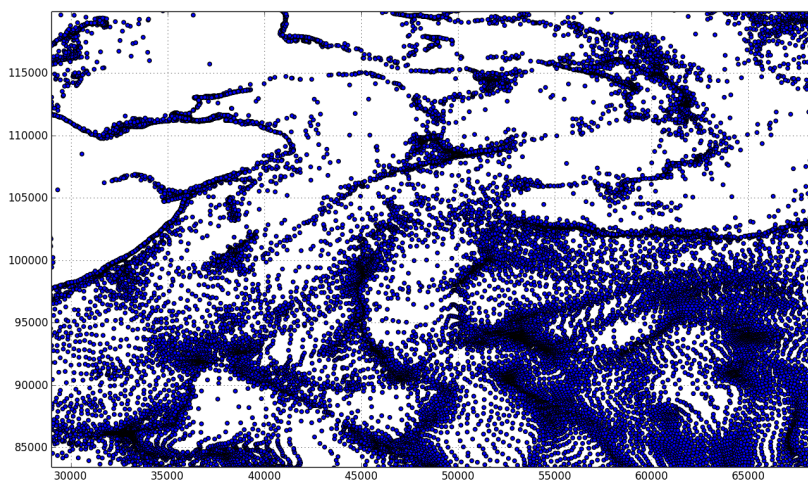


Figure 4.17 – Clustering of particles on small-scale structures in the FRF (lower than the cutoff wave-length $\lambda \sim 30$ km).

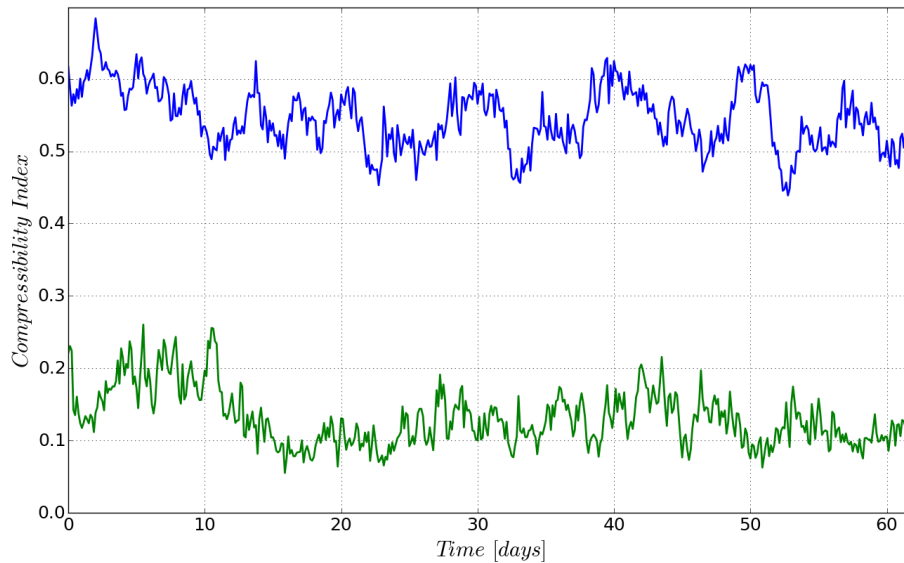


Figure 4.18 – Compressibility index as function of time, it is equal to 0 in incompressible flows (averaging on space) and it is equal to 1 in the pure potential case. The blue line represents the fully resolved field while the green represents the filtered one. It is evident for all times that, in the filtering process, a great contribution to compressibility is removed.

effect cannot be seen and Eddy Diffusivity schemes work well. However, vertical phenomena like in the Greenland Sea are not rare in oceanography and standard Eddy Diffusion models can significantly overestimate the transport. Moreover, this result points out the necessity to develop new closures that are able to describe transport processes also in presence of a compressible component in the subgrid dynamics.

Appendix A

Papers in preparation

Related with the research developed in this thesis I have two papers in preparation:

1. *Atmospheric stability shapes strategies for fungal spores liberation* in collaboration with A. Mazzino (Dicca - Unige), A. Seminara (CNRS - Nice) and A. Pringle (University of Madison WI)
2. *Sea-surface transport of non-bouyant particles* in collaboration with A. Mazzino (Dicca - Unige) and M.G. Magaldi (CNR - La Spezia)

Bibliography

- [1] <https://www.ars.usda.gov> “United States Department of Agriculture”.
- [2] L. Palatella, F. Bignami, F. Falcini, G. Lacorata, A. S. Lanotte, and R. Santoleri, “Lagrangian simulations and interannual variability of anchovy egg and larva dispersal in the in the Sicily Channel”, *J. Geophys. Res. Oceans* 119, 1306–1323 (2014).
- [3] M. Roper, A. Seminara, M. M. Bandi, A. Cobb, H.R. Dillard, A. Pringle, “Dispersal of fungal spores on a cooperatively generated wind”, *PNAS* 107, 17474 (2010).
- [4] J. Fritz, A. Seminara, M. Roper, A. Pringle and M. P. Brenner, “A natural O-ring optimizes dispersal of fungal spores”, *J Roy Soc Interface* 10, 20130187 (2013).
- [5] F. Trail and A. Seminara, “The mechanism of ascus firing - merging biophysical and mycological viewpoints”, *Fungal Biol Rev* 28, 70 (2014).
- [6] D. Andrade, Z. Pan, W. Dannevik, and J. Zidek, “Modeling soybean rust spore escape from infected canopies: model description and preliminary results”, *Journal of Applied Meteorology and Climatology* 48(4), 789-803 (2009).
- [7] H. Wang, X. B. Yang, and Z. Ma, “Long-distance spore transport of wheat stripe rust pathogen from Sichuan, Yunnan, and Guizhou in southwestern China”, *Plant disease* 94(7), 873-880 (2010).
- [8] D. E. Aylor, “Aerial spore dispersal close to a focus of disease”, *Agricultural and forest meteorology* 47(2-4), 109-122 (1989).
- [9] M. G. Magaldi, T. W. N. Haine, “Hydrostatic and non-hydrostatic simulations of dense waters cascading off a shelf: the East Greenland case”, *Deep Sea Res. I* 96 , 89-104 (2015).
- [10] J. Marshall, A. Adcroft, C. Hill, L. Perelman, and C. Heisey, “A finite-volume, incompressible Navier Stokes model for studies of the ocean on parallel computers”, *J. Geophys. Res.* 102(C3), 5753–5766 (1997).

-
- [11] G. Falkovich, K. Gawedzki, M. Vergassola “Particles and fields in fluid turbulence”, *Reviews of modern physics* 73, 913-975 (2001).
- [12] P. K. Kundu, I. M. Cohen, “Fluid Mechanics.” Elsevier Academic Press (2008).
- [13] P. Castiglione, A. Mazzino, P. Muratore and A. Vulpiani, “On strong anomalous diffusion”, *Physica D* 134, 75-93 (1999).
- [14] K.H. Andersen, P. Castiglione, A. Mazzino and A. Vulpiani, “Simple stochastic models showing strong anomalous diffusion”, *Eur. Phys. J. B* 18, 447-452 (2000).
- [15] H. B. Fischer, “Mixing in inland and coastal waters.” Academic Press (1979).
- [16] U. Frisch, “Turbulence: the legacy of AN Kolmogorov.” Cambridge University Press (1995).
- [17] S. Boi, A. Mazzino and G. Lacorata, “Explicit expressions for eddy-diffusivity fields and effective large-scale advection in turbulent transport”, *Journal of Fluid Mechanics* 795, pp. 524–548 (2016).
- [18] I. Hernández-Carrasco, C. López, E. Hernández-García and A. Turiel, “How reliable are finite-size Lyapunov exponents for the assessment of ocean dynamics?”, *Ocean Modelling* 36(3-4), 208-218 (2011).
- [19] C. M. Bender, S. A. Orszag, “Advanced Mathematical Methods for Scientists and Engineers,” MacGraw Hill, New York (1978).
- [20] L. Biferale, A. Crisanti, M. Vergassola, A. Vulpiani, “Eddy diffusivities in scalar transport”, *Physics of Fluids* 7(11), 2725-2734 (1995).
- [21] A. Mazzino, S. Musacchio, A. Vulpiani, “Multiple-scale analysis and renormalization for preasymptotic scalar transport”, *Physical Review E* 71(1), 011113 (2005).
- [22] J. H. LaCasce, “Statistics from Lagrangian observations”, *Progress in Oceanography* 77(1), 1-29 (2008).
- [23] J. Tesmer and M. Schnittler, “Sedimentation velocity of myxomycete spores”, *Mycological Progress* 6(4), 229 (2007).
- [24] C. E. Yarwood, “Water content of fungus spores”, *American Journal of Botany* 636-639 (1950).
- [25] “<https://www.arl.noaa.gov>”, Air Resource Laboratory website.
- [26] J. R. Garratt, “The atmospheric boundary layer”, Cambridge University Press, Cambridge (1992).

-
- [27] R. B. Stull, “An introduction to boundary layer meteorology”, Springer Science and Business Media (2012).
- [28] F. Mesinger, G. DiMego, E. Kalnay, K. Mitchell and Coauthors, “North American Regional Reanalysis”, *Bulletin of the American Meteorological Society* 87, 343–360 (2006).
- [29] “<https://www.ncdc.noaa.gov>”, National Oceanic and Atmospheric Administration website.
- [30] H. Risken, “The Fokker-Planck Equation”, Springer, Berlin, Heidelberg (1996).
- [31] S. Chandrasekhar, “Stochastic problems in physics and astronomy”, *Reviews of modern physics* 15(1), 1 (1943).
- [32] Y. Kaneda, T. Ishihara, K. Gotoh, “Taylor expansions in powers of time of Lagrangian and Eulerian two-point two-time velocity correlations in turbulence”, *Physics of Fluids* 11(8), 2154-2166 (1999).

Acknowledgments

I would like to thank all the people who supported me during these three years and without whom this would not have been possible: my supervisor Andrea Mazzino, who patiently guided me in this experience; Agnese Seminara, who introduced me to the fascinating field of biophysics and whose support was essential; Marcello Magaldi for giving me the opportunity to work with high-resolution datasets.

Thanks also to all the office mates with whom I shared joy and efforts: Davide, Peyman, Duaa, Krystyna, Francesco De Leo, Francesco Enrile, Francesco Ferrari, Stefano, Irene, Masha, Gaetano. I also want to thank all the friends and my family, essential support in times of hard work: mom and dad, Simone and Marco, Fausto and Graziella but above all Chiara and Bianca. Thank you!